η Carinae

Detection and Characterisation of the First Colliding-Wind Binary in Very-High-Energy γ-rays with H.E.S.S.

Doktorarbeit
zur Erlangung des akademischen Grades
Dr. rer. nat.
in Astroteilchenphysik

vorgelegt von

Eva Leser (Master of Science)

Institut für Physik und Astronomie
Universität Potsdam
2018

1. Gutachter : Prof. Dr. Christian Stegmann
2. Gutachter : Prof. Dr. Jörn Wilms
3. Gutachter : Prof. Dr. Marek Kowalski

Datum des Einreichens der Arbeit: 20. 11. 2018

Published online at the
Institutional Repository of the University of Potsdam:
https://doi.org/10.25932/publishup-42814
https://nbn-resolving.org/urn:nbn:de:kobv:517-opus4-428141

Selbstständigkeitserklärung

Ich versichere, dass ich die vorliegende Arbeit selbständig und nur mit den angegeben Quellen und Hilfsmitteln angefertigt habe. Alle Stellen der Arbeit, die ich aus diesen Quellen und Hilfsmitteln dem Wortlaut oder dem Sinne nach entnommen habe, sind kenntlich gemacht und im Literaturverzeichnis aufgeführt. Weiterhin versichere ich, dass ich die vorliegende Arbeit, weder in der vorliegenden, noch in einer mehr oder weniger abgewandelten Form, als Dissertation an einer anderen Hochschule eingereicht habe.

Potsdam, Eva Leser

Kurzfassung

Das außergewöhnliche Doppelsternsystem η Carinae fasziniert WissenschaftlerInnen und BeobachterInnen auf der südlichen Erdhalbkugel seit hunderten Jahren. Nach einem Supernova-ähnlichem Ausbruch war η Carinae zeitweise der hellste Stern am Nachthimmel. Heute sind durch zahlreiche Beobachtungen, von Radiowellen bis zu Röntgenstrahlung, der Aufbau des Sternsystems und die Eigenschaften seiner Strahlung bis zu Energien von $\sim 50\,\mathrm{keV}$ gut erforscht. Das Doppelsternsystem besteht aus zwei massiven Sternen (~ 30 und ~ 100 Sonnenmassen Gewicht) mit starken Sternwinden, über die sie kontinuierlich einen Teil ihrer Masse verlieren. Wenn diese Sternwinde kollidieren, entsteht auf beiden Seiten ein Kompressionsschock der das Plasma in der Kollisionszone aufheizt, was sich in Röntgenstrahlung beobachten lässt. Bei Energien oberhalb von $\sim 50\,\mathrm{keV}$ ist der Ursprung der Strahlung nicht mehr thermisch: um ein Plasma auf die entsprechende Temperatur zu bringen, wird mehr mechanische Energie benötigt, als in den Sternwinden vorhanden. In hoch-energetischer γ-Strahlung ist η Carinae das einzige eindeutig detektierte Sternsystem seiner Art und sein Energiespektrum reicht bis zu $\sim$ hundert GeV. Bodengebundene γ-Strahlungsexperimente haben in diesem Energiebereich den Vorteil von großen Detektorflächen. H.E.S.S. ist das einzige bodengebundene γ-Strahlungsexperiment auf der Südhalbkugel und somit in der Lage, η Carinae in diesen Energien zu beobachten. H.E.S.S. misst γ-Strahlung mit Hilfe der elektromagnetischen Teilchenschauer, die sehr hoch-energetische Photonen in der Atmosphäre auslösen. Die größte Herausforderung der Messung von η Carinae's Strahlung mit H.E.S.S. ist die ultraviolette Strahlung des Carina Nebels, die zu einem Hintergrund führt, der bis zu zehn mal stärker ist als der Durchschnitt in H.E.S.S. In dieser Arbeit wird die erste Detektion eines Doppelsternsystems mit kollidierenden Sternwinden in sehr hoch-energetischer γ-Strahlung präsentiert und die Studien, die diese ermöglicht haben. Das differentielle γ-Strahlungsspektrum bis $700\,\mathrm{GeV}$ wird untersucht. Hadronische und leptonische Szenarios für den Ursprung der γ-Strahlung werden diskutiert und das hadronische Szenario wird aufgrund eines Vergleichs der Kühlzeiten bevorzugt.

Abstract

The exceptional binary star η Carinae has been fascinating scientists and the people in the Southern hemisphere alike for hundreds of years. It survived an enormous outbreak, comparable to a supernova energy-wise, and for a short period became the brightest star of the night sky. From observations from the radio regime to X-rays the system's characteristics and its emission in photon energies up to $\sim 50\,\mathrm{keV}$ are well studied today. The binary is composed of two massive stars of ~ 30 and ~ 100 solar masses. Either star drives a strong stellar wind that continuously carries away a fraction of its mass. The collision of these winds leads to a shock on each side of the encounter. In the wind-wind-collision region plasma gets heated when it is overrun by the shocks. Part of the emission seen in X-rays can be attributed to this plasma. Above $\sim 50\,\mathrm{keV}$ the emission is no longer of thermal origin: the required plasma temperature exceeds the available mechanical energy input of the stellar winds. In contrast to its observational history in thermal energies observational evidence of η Carinae's non-thermal emission has only recently built up. In high-energy γ-rays η Carinae is the only binary of its kind that has been detected unambiguously. Its energy spectrum reaches up to $\sim$ hundred GeV, a regime where satellite-based γ-ray experiments run out of statistics. Ground-based γ-ray experiments have the advantage of large photon collection areas. H.E.S.S. is the only γ-ray experiment located in the Southern hemisphere and thus able to observe η Carinae in this energy range. H.E.S.S. measures γ-rays via electromagnetic showers of particles that very-high-energy γ-rays initiate in the atmosphere. The main challenge in observations of η Carinae with H.E.S.S. is the UV emission of the Carina nebula that leads to a background that is up to 10 times stronger than usual for H.E.S.S. This thesis presents the first detection of a colliding-wind binary in very-high-energy γ-rays and documents the studies that led to it. The differential γ-ray energy spectrum of η Carinae is measured up to 700 GeV. A hadronic and leptonic origin of the γ-ray emission is discussed and based on the comparison of cooling times a hadronic scenario is favoured.

Contents

Chapter 1

Introduction

Die Wissenschaft stellt sowohl diese bildende Bewegung in ihrer Ausführlichkeit und Notwendigkeit als [auch] das, was schon zum Momente und Eigentum des Geistes herabgesunken ist, in seiner Gestaltung dar. Das Ziel ist die Einsicht des Geistes in das, was das Wissen ist. [1]

Science lays before us the morphogenetic process of this cultural development in all its detailed fullness and necessity, and at the same time shows it to be something that has already sunk into the mind as a moment of its being and become a possession of mind. The goal to be reached is the mind's insight into what knowing is. [2]

As a young branch of modern physics, γ-ray astronomy seeks to further our knowledge about the flux of highly energetic photons reaching the Earth in GeV to TeV energies. In general, these photons are produced in interactions of accelerated cosmic rays with ambient radiation fields and matter of the interstellar medium. The search for acceleration sites of cosmic rays is thus linked to the search for γ-ray sources. As neutral particles, γ-rays have the advantage of tracing back to their sources while the charged cosmic rays are deflected by interstellar magnetic fields. The composition of cosmic rays is dominated by protons and α-particles ($\sim 98\,\%$). Heavier nuclei, positrons and electrons also contribute on a smaller scale ($\sim 1.8\,\%$). The last two decades have brought substantial progress in our understanding of sources of very-high energy γ-rays. In this energy regime, ground-based γ-ray telescopes outperform space-based satellite experiments because the decreased flux of γ-rays requires larger collection areas. Imaging Atmospheric Cherenkov Telescopes, like H.E.S.S., have successfully mapped the very-high energy γ-ray sky.

Up to the "knee" of the cosmic-ray energy spectrum at $\sim 4 \times 10^{15}\,\mathrm{eV}$, it can be described by a power law with an index of -2.7. Above the "knee" the slope of the spectrum steepens and this is interpreted as the transition from galactic to extragalactic sources. Most galactic cosmic rays are thought to be accelerated in supernova remnants. This consideration is based on their energy input: supernova remnants are the only galactic sources powerful enough to maintain the observed cosmic-ray density of $\sim 10^{48}\,\mathrm{erg/yr}$, assuming that about 10 % of the average kinetic energy of a supernova goes into cosmic-ray acceleration and 1 supernova explosion takes place every 50 - 100 years [3, 4].

Beside supernova remnants, other objects may contribute to the flux of cosmic rays as well, e.g. γ-ray binaries with compact objects [5, 6] or microquasars [7], which show very-high energy γ-ray emission. Another source class that has been proposed to be capable of accelerating particles are colliding-wind binaries [8]. First only considered as sources for soft γ-rays (MeV-GeV energies), the linkage of massive stars to very-high energy γ-ray emission [9] and the detection of γ-ray emission close to the thresholds of current very-high energy experiments sparked interest also in the very-high energy regime. Particle acceleration is supposed to take place in the shocks that form when the strong stellar winds collide. Some basic criteria that have to be met are fast shock velocities ($\gtrsim 1000\,\mathrm{km\,s^{-1}}$), an available wind power of $\sim 10^{37}\,\mathrm{erg\,s^{-1}}$ and soft photon fields/ high-density gas as a target.

Following Hegel, the insight into *what knowing is*, the foundation of our knowledge, starts at reflecting upon the concept of knowledge you are applying. In the case of the enigmatic colliding-wind binary η Carinae, which will be investigated in very-high energy γ-rays in this work, this includes a rich history of concepts and observations. The most relevant observations will be covered in the subsequent chapter, with the emphasis laid on observations of non-thermal emission. The production mechanisms of γ-rays in general and the origin of emission towards η Carinae in high-energy γ-rays are discussed at the end of the chapter.

Figure 1.1, *left*, gives an impression of the number of bright stars in the Carina Nebula. The amount of stellar UV photons reaching the Cherenkov telescopes are the main obstacle for a detection of η Carinae in very-high energy γ-rays. The challenge that observations of η Carinae with the H.E.S.S. telescopes, and especially the analysis of

H.E.S.S. data on η Carinae, pose, will be elaborated in detail in chapter 3. Additionally, the methods for the reconstruction of the properties of the primary γ-ray from the indirect measurement of Cherenkov light are presented. The analysis of η Carinae observations with H.E.S.S. is given in chapter 4, followed by conclusions and an outlook in chapter 5.

Figure 1.1: Pavel Alekseyevich Cherenkov (*right*), discoverer and eponym of Cherenkov radiation, for which he was awarded the Nobel Prize in Physics in 1958. Broad-band optical image of the Carina Nebula taken at the Cerro Tololo 4-meter Blanco telescope in 1976 with a zoomed inlay of η Carinae in X-rays observed with CHANDRA (orange) and optical emission observed with the Hubble Space Telescope (light blue) (*left*). Credits: broad-band optical: NOAO/AURA/NSF (underlying image), X-ray: NASA/CXC/GSFC/M.Corcoran et al.; Optical: NASA/STScI (inlay) (*left*), [10] (*right*).

Chapter 2

The colliding-wind binary η Carinae

2.1 Observational history

η Carinae's appearance today as depicted in figure 2.1 by the *Hubble Space Telescope* is the result of a history of massive eruptions. The prominent structure of gas and dust around the central star, the *Homunculus Nebulae*, resembles two lobes, which are separated by a collar-like outflow. η Carinae has been in the focus of astronomers for at least four centuries, in more and more observational windows as technology advanced. It is first recorded in writing in Halley's *Catalogus Stellarum Australium*, published in 1679, which maps the stars of the Southern Hemisphere (see figure 2.1 for a picture of the original page in the catalog) [11]. Already in 1595 a Dutch expedition to the East Indies with navigator Pieter Keyser had carried out the first accurate observations of the southern stars [12]. In the following years the globes by Petrus Plancius and Jodocus Hondius were expanded to include these observations, depicting a star of magnitude four at the position of η Carinae [12]. Despite that, in Houtman's star catalog from 1603, η Carinae is missing. It is not clear, whether it was omitted because it did not reach the magnitude threshold or if it was overlooked [13]. In traditional Chinese astronomy the binary system first appeared when the *Southern Asterisms* were added in the 17th century [14]. What captured the attention of our ancestors were drastic changes in luminosity like they occurred in 1827 and 1838. In 1827 William Burchell was the first to observe variability in η Carinae [15]. Sir John Herschel then monitored the system at the Cape of Good Hope from 1834 and did not see any change in luminosity up till 1838, when a sudden increase in brightness occurred [15]. The nebula shaping our image of the binary today dates back to this period of activity in the 1830s when the first documented eruption in η Carinae started [13]. Thomas Maclear and C. P. Smyth who were

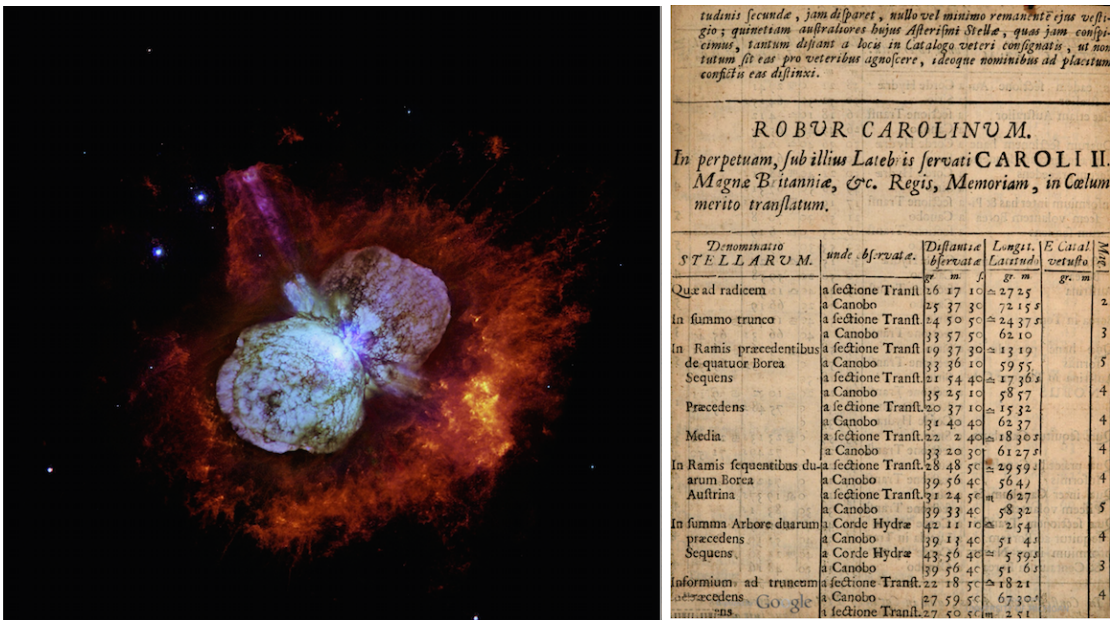

tudinis ſecundæ, jam diſparet, nullo vel minimo remanente ejus veſtigio; quinetiam auſtraliores hujus Aſteriſmi Stellæ, quas jam conſpicimus, tantum diſtant a locis in Catalogo veteri conſignatis, ut non tutum ſit eas pro veteribus agnoſcere, ideoque nominibus ad placitum conficti eas diſtinxi.

ROBUR CAROLINUM.

In perpetuam, ſub illius Lateb is ſervati CAROLI II. Magnæ Britanniæ, &c. Regis, Memoriam, in Cœlum merito tranſlatum.

Denominatio STELLARUM.	unde obſervatæ.	Diſtantiæ obſervatæ	Longit. Latitudo	E Catal. vetuſto	Mag.
		gr. m. ſ.	gr. m.	gr. m.	
Quæ ad radicem	a ſectione Tranſit.	26 17 10	♋ 27 25		
	a Canobo	25 37 30	72 15 5		2
In ſummo trunco	a ſectione Tranſit.	24 50 50	♋ 24 37 5		
	a Canobo	33 57 50	62 10		3
In Ramis præcedentibus de quatuor Borea	a ſectione Tranſit.	19 37 30	♋ 13 19		
	a Canobo	33 36 10	59 55		5
Sequens	a ſectione Tranſit.	21 54 40	♋ 27 36 5		
	a Canobo	35 25 10	58 57		4
Præcedens	a ſectione Tranſit.	20 37 10	♋ 15 32		
	a Canobo	31 40 40	62 37		4
Media.	a ſectione Tranſit.	22 2 40	♋ 18 30 5		
	a Canobo	33 20 30	61 27 5		4
In Ramis ſequentibus duarum Borea	a ſectione Tranſit.	28 48 50	♋ 29 59		
	a Canobo	39 56 40	56 43		4
Auſtrina	a ſectione Tranſit.	31 24 50	♌ 6 27		
	a Canobo	39 33 40	58 32		5
In ſumma Arbore duarum	a Corde Hydræ	42 11 10	♋ 2 54		
præcedens	a Canobo	39 13 40	51 45		4
Sequens.	a Corde Hydræ	43 56 40	♋ 5 59 5		
	a Canobo	39 56 40	51 65		3
Informium ad truncum	a ſectione Tranſit.	22 18 50	♋ 18 21		
præcedens	a Canobo	27 59 50	67 30 5		4
ſequens.	a ſectione Tranſit.	27 50 50	♌ 2 51		

Figure 2.1: η Carinae and its Homunculus Nebula in red and near-ultraviolet light as observed by NASA's Wide Field and Planetary Camera 2 (*left*). Image Credit: Nathan Smith (University of California, Berkeley), and NASA. Original page from 1679's *Catalogus Stellarum Australium* depicting η Carinae as *Sequens* in fifth line from below (*right*) [11].

also observers at the Cape of Good Hope Observatory took interest in this variable star and entered into correspondence with Sir Herschel to find all available data. Herschel was not the only one to observe the eruption: in a paper from 1857 William Stanbridge reported about the astronomical knowledge of the Boorong clan that used to live in northwest Victoria, Australia [16]. From his report, Frew and Hamacher were able to identify η Carinae, known to the Boorong as *Collowgullouric War* in observations from the 1840s [17]. The name η Carinae dates back to late 19th century catalogue *Uranometria Argentina* by Benjamin A. Gould, an American astronomer and student of Carl F. Gauss in Göttingen [18]. Before, the binary system was known as Eta Argus, Eta Navis and Eta Roboris Caroli [13].

Looking at the historical light curve (figure 2.2), the brightening noticed in 1838 was only the beginning of a decades long period of extraordinary eruptions accompanied by high luminosity which coined the term *Great Eruption* [13]. In several energetic outbursts a very large amount of material was expelled from the primary star, totalling up to about 12 times the mass of the sun [19].

Energetics-wise, the Great Eruption was comparable to a supernova, which marks the end of the star's life. In η Carinae's case the massive star survived, thus the term *supernova impostor* was established [20]. The gas and dust that has been released in the eruptions more than 170 years ago is still visible today and forms the Homunculus Nebulae (in figure 2.1 the structure can be identified by its characteristic lobes). A smaller outburst occurred around 1890 (compare figure 2.2) and produced the little Homunculus within the Homunculus Nebulae (compare figure 2.3) [21]. The 12 solar

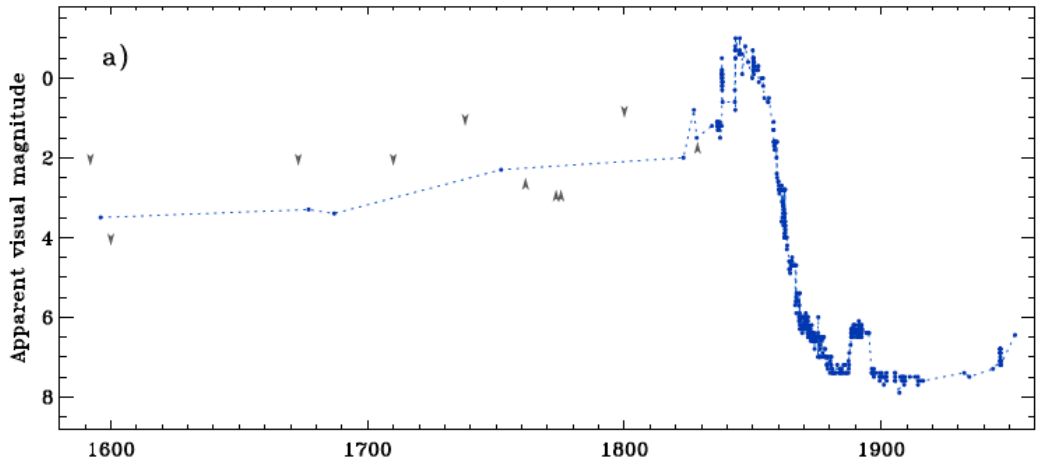

Figure 2.2: Historical light curve of η Carinae showing the rise in magnitude during the years of the Great Eruption (1822-1864) and the lesser Eruption in 1890. Grey arrows depict limits [13].

masses material expelled in the Homunculus Nebulae moves at a speed of $\sim 650\,\mathrm{km\,s^{-1}}$ (while the nested little Homunculus is only half as fast) [19, 21]. This leads to a kinetic energy contained in the Homunculus Nebulae of $10^{49.6} - 10^{50}$ ergs [19]. Also originating in the Great Eruption is a fast blast wave that is threefold to fourfold the size and speed of the Homunculus Nebulae. The blast wave has a geometry similar to the Homunculus itself and is correlated to the X-ray shell. In terms of kinetic energy, the blast wave provides about the same amount as expected in the Homunculus Nebulae [22]. For a long time η Carinae was thought to be a single luminous blue variable (LBV), a short-lived stellar phase with high mass loss rates [23, 24], although there were speculations about a binary scenario to explain some features of the optical light curve [25]. Measurements of periodic radial velocity variations in the emission spectrum supported the binary scenario [26]. Following observations accumulated further evidence

and the binary scenario is now widely accepted for η Carinae [27, 28].

2.2 Colliding-wind binaries: Thermal and non-thermal emission

So far, the observations mentioned are in the regime of thermal energies but in the last years evidence for non-thermal emission from η Carinae has been observed. The distinction between thermal and non-thermal emission is based upon characteristic features like the spectral index of the photon flux density, the brightness temperature T_B and variability in the radio domain [29]. Thermal radiation in infrared and radio domains originates from the plasma of the stellar envelope where electrons scattering off ionized hydrogen produce thermal Bremsstrahlung (*free-free emission*) [30]. The energy of the electrons follows a Maxwell-Boltzmann distribution and the photon flux density S_ν can be described in dependence of the frequency ν and the spectral index α as

$$S_{\gamma,thermal} \propto \nu^{\alpha}. \tag{2.1}$$

Based on the measurement of thermal radio emission it is possible to determine the mass loss rate of a massive star [30]. The observed characteristic spectral index for thermal emission is α equal to 0.6 (implying a homogeneous mass loss rate and constant velocity) [31]. The brightness temperature T_B is the black body temperature needed to produce the observed photon flux density. For thermal emission $T_{B,thermal} \sim 10^4\,\mathrm{K}$, while non-thermal (radio) emission is accompanied by black body temperatures of one or two orders of magnitude higher.

Non-thermal radiation originates from interactions of highly energetic particles in synchrotron radiation, inverse Compton scattering or π^0-decay (see 2.6). The spectral index α is significantly lower than 0.6 in case of non-thermal emission. Variability in the radio emission is also considered to be a hint for non-thermal emission, because the plasma giving rise to thermal emission is not expected to change on short timescales.

Colliding-wind binaries (CWBs) like η Carinae are binary systems consisting of massive (early type, over 8 $M_\odot$ [32]), typically O- or B-type or Wolf-Rayet stars, with colliding stellar winds (see figure 2.3 for an illustrated model of η Carinae). Some CWBs are particle accelerators showing non-thermal emission. Particle acceleration of relativistic electrons and/or protons is supposedly happening in the wind-wind interac-

tion regions, where strong shocks form [33]. Multiplicity (the number ob stars in the system) is a crucial ingredient for particle acceleration in this type of objects to allow for stellar wind collisions [8]. Besides the question of a contribution to cosmic rays, massive stars are interesting as donors of material. They enrich the interstellar medium with material which is a potential target for particles, leading to production of γ-rays subsequently.

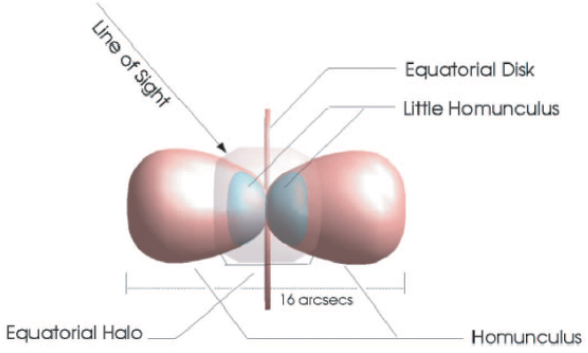

Figure 2.3: Cartoon model of the η Carinae nebula [21].

There are at least 43 objects in our galaxy which can be attributed as particle accelerating CWBs (multiple member systems included) [29]. Compared to the most common sources of γ-rays in our galaxy, supernova remnants and pulsar wind nebulae, CWBs probably only contribute on a smaller scale and only in the GeV regime. This contribution could still be significant: following the argument in [34], a population of 10^5 massive stars with energy injection rates in charged particles between 0.01% to 1% would lead to an integrated power in cosmic rays of $10^{37} - 10^{39}\,\mathrm{erg\,s^{-1}}$. The total power in cosmic-rays is in the order of $10^{40}\,\mathrm{erg\,s^{-1}}$ thus resulting in $0.1 - 10\,\%$ potential contribution of CWB [3]. The contribution of CWBs depends on the fraction of particle accelerators among CWBs which is identified by non-thermal emission processes but tracing these can be difficult. In the radio domain absorption by stellar wind material can hide synchrotron emission [29]. In X-rays, thermal emission dominates over non-thermal emission below 10 keV leaving only the hard X-ray regime for a potential detection [34]. Measurements of gamma-ray emission are also a strong evidence for particle acceleration and theoretically expected for systems with powerful stellar winds [8, 35]. Two stellar wind parameters determine the kinetic power of a stellar wind, the mass loss rate and the terminal wind velocity. Still, most particle accelerating CWBs are non-thermal radio emitters. The only two systems showing non-thermal hard X-ray

emission are η Carinae and WR 140 [36, 37]. η Carinae stands further out as also being the only CWB detected in high energy gamma-rays (although there are hints for high energy gamma ray emission also in WR 11) [38, 39]. Although η Carinae does not produce radio synchrotron radiation, which WR 140 does, both systems share some key features like a high eccentricity (~ 0.9) and long periods (5.52 and 8 years) [23, 40].

2.3 The neighbourhood - the Carina Nebula

η Carinae lies within NGC 3372 - the Carina Nebula - a massive active starforming region situated in the Carina constellation in the southern hemisphere at a distance of 2.3 kpc [41]. It is one of the brightest parts of the Milky Way and can be seen with the naked eye. Its red appearence (compare fig. 2.4) is due to hydrogen that is illuminated by star light. The Carina Nebula hosts 6 open stellar clusters (counting Cr 228 and Cr 232 as a part of Tr 16), which differ in age between 0.1 and 8 Myr, testifying the past star-formation [41]. It is studied in great detail in visual-wavelengths because of little extinction and reddening along the line of sight compared to other star-forming regions. The stellar population of the Carina Nebula currently consists of at least 65 O-type stars, 3 Wolf-Rayet (WR) stars (WR 25/ HD 93162, HD 93131 and HD 92740) and the Luminous Blue Variable η Carinae residing in the stellar cluster Tr 16 [42]. The more massive stars tend to exist in the clusters Tr 16, Tr 14 and Tr 15, while the younger star population spreads over the younger clusters (e.g. *Treasure Chest*) and extends over the Carina Nebula without a cluster association [43]. The energy input in the nebula is dominated by the massive cluster Tr 16 and especially η Carinae. The age of the cluster can be confined by the presence of H-rich WR stars and the absence of He-rich WR stars. Tr 16 is host to the H-rich Wolf-Rayet stars HD 93162, HD 93131 and HD 92740. The evolution of η Carinae off of the main sequence is also a constraining factor to the age of the cluster, which is estimated to be between 2-3 Myr. For the UV luminosity, the *Great Eruption* marked a turning point since after the outburst the dust shell has been cutting off the UV emission from the binary [42]. In terms of mechanical energy, stellar winds in Tr 16 have provided up to 2.6×10^{52} ergs in the 3 Myr of their existence. Only a fraction (3 - 20 %) of this energy is kinetic energy that drives the expansion, while most energy is lost in radiation [42]. However, this fraction depends on mass loss rates and the amount of clumping in the stellar winds [44]. The nebulosity in the Carina Nebula in total reaches a mass of $10^6\,M_\odot$. Most of its mass is made up of atomic gas in photodissociation regions where also the bulk of dust resides (cooler dust with

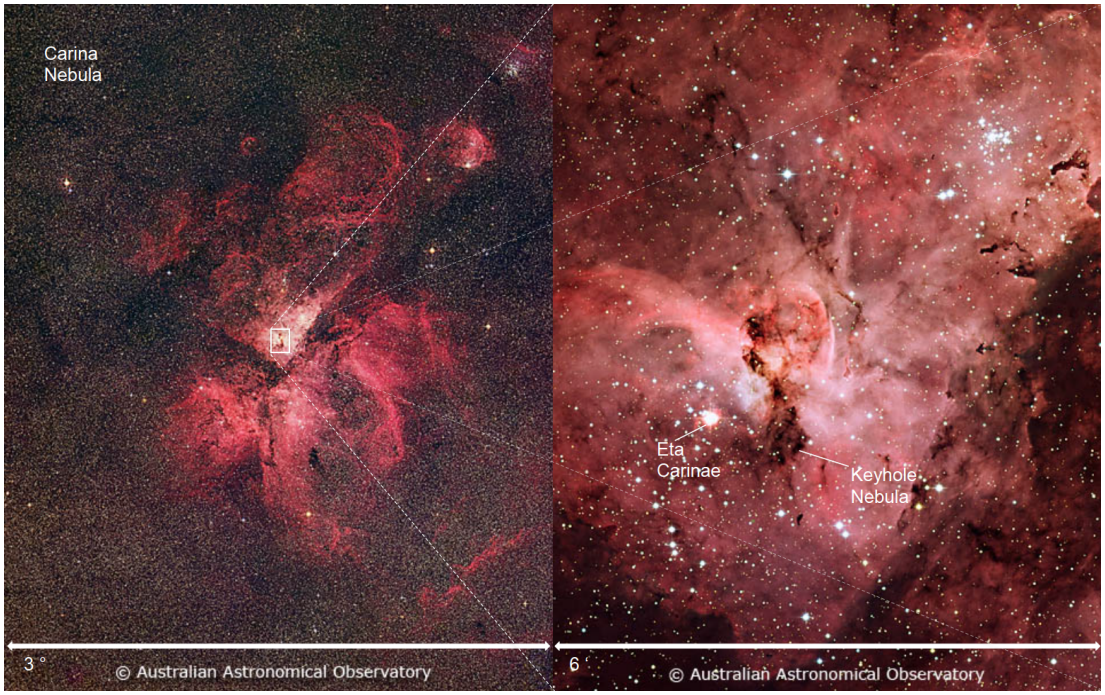

Figure 2.4: The Carina Nebula (NGC 3372) in a large field-of-view photograph on the left panel. On the right hand side is a zoom in of the marked region, including η Carinae and the Keyhole Nebula. Photographs by David Malin.

temperatures between 30 - 40 K and warmer dust at $\sim$ 80 K that is mixed with ionised gas) [45, 41]. About 1/3 of the total gas mass is molecular gas that is concentrated in the Southern Cloud, Northern Cloud and the Southern Pillar. These molecular clouds were found to be part of a giant molecular cloud complex that extends over 150 pc [46]. Molecular clouds build the foundation of starformation. η Carinae's and other massive stars' role in the formation process is the injection of energy and mass. In the Treasure Chest this suspicion is encouraged by the observation of dust pillars pointing back to η Carinae and Tr 16 [47].

2.4 η Carinae across the electromagnetic spectrum

η Carinae has been the object of numerous observations with ground-based telescopes as well as satellites, from radio to X-rays and γ-rays. The focus here will be on the high end of the energy spectrum while acknowledging the importance of observations in all wavelengths as each one of them adds its unique piece to the puzzle of understanding this outstanding object.

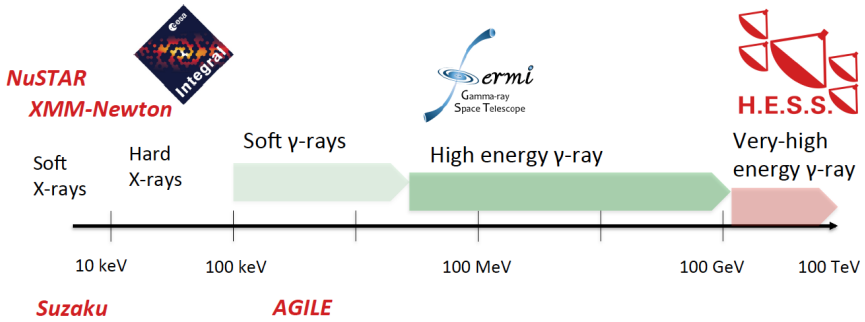

Figure 2.5: The higher end of the electromagnetic spectrum and the experiments engaged in observations of CWBs.

2.4.1 Radio, microwave and mm emission

Subsummized under radio emission is all emission with wavelengths between 100 m and about 1 cm (3 MHz – 30 GHz, "classic" radio), between 1 cm and 1 mm (30 – 300 GHz, microwaves) and between 10 mm and 0.1 mm (30 GHz – 3 THz, mm- and sub-mm) [48], [49]. For the wavelength range between 1 cm and 10 m the term *radio window* was coined to describe the property of the earth's atmosphere to be transparent to photons with these wavelengths. The radio window is used by radio telescopes like the Australia Telescope Compact Array (at Narrabri New South Wales). Besides continuum radiation there is a wealth of molecule lines to be observed in cm, mm and sub-mm. Non-thermal radio emission is an important tracer of particle acceleration in CWBs (as illustrated in section 2.2). WR 140 is one example for an object that emits both radio synchroton radiation and in X-rays [50].

Thermal radio emission in η Carinae is believed to stem from outflowing gas in the stellar wind of the primary star and an equitorial disk that gets ionized by an UV source [49]. The companion star is a possible source of ionizing photons. The emission is modulated by the orbital movement as the supply with ionizing photons from the companion is nearly blocked during periastron leading to a dip in the lightcurve (compare fig. 2.6). During periastron the photons are swallowed by the dense wind [51]. By studying the thermal free-free emission in general (not only in radio wavelengths) it is possible to derive the mass-loss rate, which plays an important role in stellar evolution [52]. However, η Carinae does not show any sign of radio synchrotron emission.

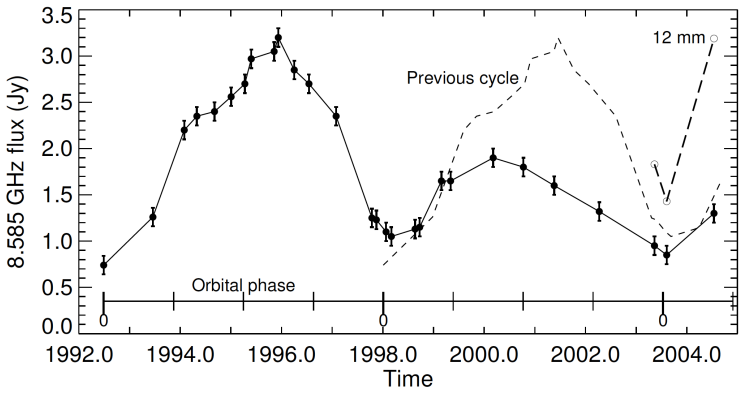

Figure 2.6: Radio lightcurve of η Carinae at 8.6 GHz (and 21 GHz) from observations at Australia Telescope Compact Array showing a minimum emission at periastron (phase 0) (source: [51]).

2.4.2 Infrared, optical and ultraviolet emission

In the infrared (with wavelengths between 100 and 1 μm), spectral and interferometric imaging is well suited to study the inner wind region of the binary system due to its excellent spatial and spectral resolution. The intensity distribution of the wind-wind collision zone (compare fig. 2.7) was found to depend heavily on wavelengths and velocity and displays a structure that was described as "fan-shaped" at velocities between -339 to $-227\,\mathrm{km\,s^{-1}}$ [53]. The atomic and molecular gas content of the Homunculus has also been studied in infrared wavelengths, finding the inner ejecta to be composed of nitrogen rich material, overall strong Fe II/[Fe II] emission lines and neutral hydrogen [54]. Along the axis of the Homunculus lies the *Strontium filament*, which is an extended ($\sim 1''$) region with emission lines of very low-ionization, e.g Strontium [55].

Observations in the optical regime (wavelengths between 1 μm and 300 nm [48]) led to the binarity hypothesis and added increasing evidence to it over the years [e.g., 56, 57, 55, 58, 59]. Damineli, Conti and Lopes reported the disappearance of lines of highest excitation energy ([NeIII], [ArIII], [FeIII] and [NII]) that had been observed before to be following a 5.52 year cycle due to η Carinae being a binary system and supported their claim by measurements of periodic radial velocities in a broad line component that they interpreted as the orbital motion of a star [26]. The emission-line spectrum in optical wavelengths is very rich and mixed with emission from the nebula and reflected starlight. Disentangling the spectral components, it was found that the broad line emission stems from the central star, unlike the narrow line emission which

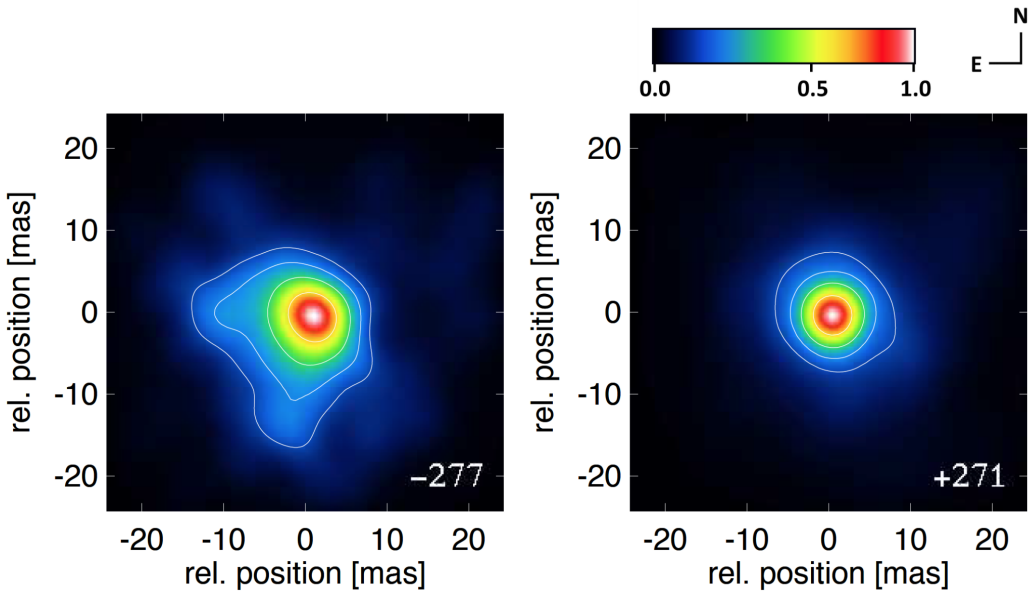

Figure 2.7: η Carinae in the near-infrared. Intensity distributions with the peak intensity normalized to unity, at different velocities (in units of $\mathrm{km\,s^{-1}}$). Contour lines depict 8, 16, 32 and 64% of the peak luminosity (source: [53]).

originates in three bright knots in the surrounding nebula [60]. These knots lie between 0.1" and 0.3" northwest of the star and were discovered by Weigelt and Ebersberger in 1986 which coined the term *Weigelt blobs* [61]. The central $\sim 0.2''$ show strong emission lines from H and Fe II [62]. The disappearing lines mentioned above were identified to be produced in the vincinity of the Weigelt blobs [62, 63]. An explanation put forward for the disappearence of the high-excitation lines is that during periastron the dense wind of the primary star blocks the ionizing photons [59].

Emission in ultraviolet (UV) wavelengths (between 300 and 10 nm [48]) plays an important role in understanding stellar evolution because many resonance lines of common elements are found there (e.g. He II). The UV spectrum of η Carinae is rich in Fe II emission and absorption lines and also shows a dip around periastron [28]. The Homunculus nebula, in contrast, is less bright in UV and shows reddening towards the edges [64]. As the secondary moves along the orbit it carves into the primary's wind and creates a low-density cavity. Groh et al were able to reproduce the characteristic UV absorption features in a 2D radiative transfer model by incorporating this cavity [65]. The cavity's influence on emission lines is correlated to the size of their formation volume [28].

Between 1998 and 2006 η Carinae went through a phase of increasing brightness with a peak in 2006 at a magnitude of V = 4.7 [57]. Since then its brightness slowly increased further to the current value of V = 4.2 [66].

2.4.3 X-rays

η Carinae's X-ray spectrum has been monitored for the last 2 to 3 decades, covering 4 orbital cycles. X-rays from binaries of massive stars were theoretically predicted in the mid 70s [67, 68], η Carinae was first detected in 1978 [69, 70]. Variability, which characterises the binary's emission in all wavelengths covered so far, is also present in X-rays. It was first detected in 1995 by Corcoran et al. in data collected with the *ROSAT* X-ray satellite [71]. The binary hypothesis was put forward in 1997 based on periodic radial velocities in a broad-line component [26, 25]. A colliding-wind binary should also manifest itself in periodic X-ray variations due to orbital changes in the wind collision region. Indeed, the recurrence of a X-ray minimum was observed after 5.5 yr. Also observed variations in X-ray flux and column density N_H supported the colliding-wind binary model [72]. There are several emission components to the X-ray emission: soft, extended X-ray emission (with $E < 1$ keV) is seen to originate from the Homunculus nebula while a harder ($E > 3$ keV), point-like component emerges from the optical position of the primary star [73].

In fig. 2.8 the X-ray lightcurve below 10 keV is depicted. It shows a slow, steady rise to a maximum over a period of $\sim$ 1 yr, then a sharp drop to the minimum flux, followed by a quick recovery to a second peak at maybe one third of the peak flux level. From this second peak onward, the flux slightly decreases, before it begins to rise again. The X-ray minimum occurs along with the fading of the high-excitation line emission and the IR brightness. The origin of thermal X-rays (< 10 keV) at the position of η Carinae lies in the wind-wind collision (WWC) region, where hot ($T \sim 10^7$ K), shocked gas resides [e.g. 74].

The rapid transition between X-ray minimum and maximum has been associated with the periastron passage. As the secondary moves along the orbit it carves into the primary's wind and creates a low-density "tunnel" which allows thermal X-rays from the WWC region to escape [76]. The sudden transition to minimal emission can be interpreted as the destruction of the low-density cavity by the primary wind. There are,

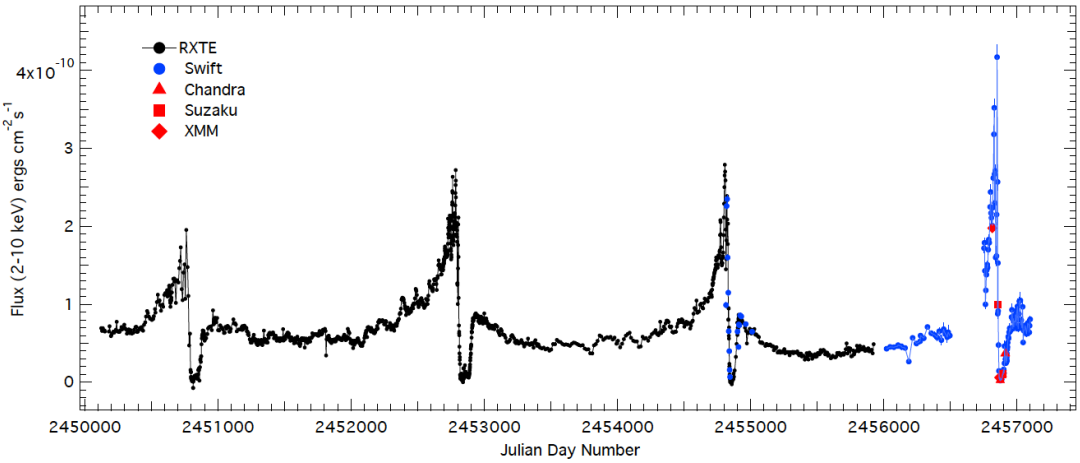

Figure 2.8: η Carinae's X-ray flux (2 - 10 keV) 1996 - 2014 (source: [75]).

however, some open issues which complicate the picture, like non-phase-locked variations in the X-ray flux, flares and the identity of the secondary star. Variations of the X-ray flux can be used to deduce important characteristics of the system like the mass-loss rate of the primary star, the companion star and the wind-speed of the companion star.

In the early 2000s, Italian-Dutch X-ray astronomy satellite *BeppoSAX* was the first experiment to claim a "super-hard" [36] emission component of non-thermal origin that extends clearly over 10 keV at the orbital phases of 0.46, 0.83, 0.37 [77, 78, 79]. Satellites *INTEGRAL* and *Suzaku* confirmed the existence of a non-thermal X-ray component up to 100 keV/ 50 keV in 2008 (compare fig. 2.9) and 2009 [80, 36]. The orbital phases of the observations detecting the non-thermal component were ∼0, 0.17, 0.36 for *INTEGRAL* and 0.39 and 0.47 for *Suzaku*.

Data by X-ray space observatory *XMM-Newton* [81] and space-based X-ray telescope *NuSTAR* [82] shift the thermal range up to 50 keV with observations at periastron 2014 [83]. A non-thermal hard X-ray tail could not be detected during periastron [84, 83]. Beside orbital variability, another reason for the non-detection could e.g. be an increase of absorption. After the recovery of the soft X-ray flux, at phases $\gtrsim$ 0.17, *NuSTAR* detected a non-thermal component [85]. The best-fit spectral model for the non-thermal component is a power-law with $\Gamma = 1.65$ and a cut-off at 1.6 GeV. It smoothly connects to the soft component of the *Fermi*−LAT γ-ray spectrum and can be interpreted as the low-energy tail of the soft GeV emission originating from the inverse Compton

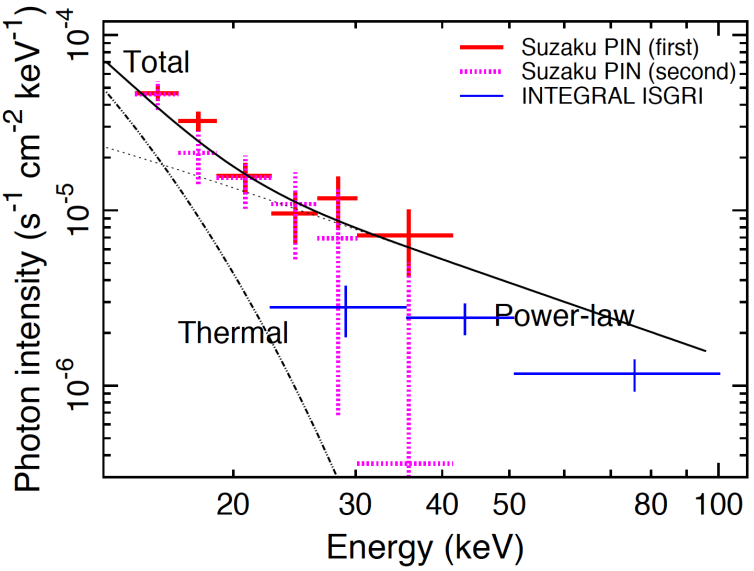

Figure 2.9: η Carinae's X-ray spectrum as observed with *Suzaku* and *INTEGRAL*. The non-thermal component is fitted with a power-law function with index $\Gamma = 1.38^{+0.14}_{-0.13}$ (source: [36]).

process. Emission mechanisms of non-thermal hard X-ray emission are deferred to in section 2.6.

2.5 Gamma-ray observations

The first detection of γ-rays from the direction of η Carinae was reported by Tavani et al in 2009 [86]. Italy's Space Agency's X- and γ-ray satellite mission ***A**stro-Rivelatore **G**amma a **I**mmagini **L**eggero - AGILE* observed the region $\sim$130 days from July 2007 - January 2009. *AGILE* operated in the energy ranges from 18 - 60 keV and between 30 MeV and 30 GeV [87]. A γ-ray source was detected at the position of η Carinae with a significance of 7.8 σ and an integrated γ-ray flux above 100 MeV of $\phi = (37 \pm 5) \times 10^{-8}\,\mathrm{ph\,cm^{-2}\,s^{-1}}$ [86]. In October 2008 a flare occurred (shortly before periastron passage in December 2008/ January 2009) that increased the flux level to $\phi = (270 \pm 65) \times 10^{-8}\,\mathrm{ph\,cm^{-2}\,s^{-1}}$ for two days (10/11 - 13).

In the same year *AGILE* reported η Carinae's detection, the binary appeared on *Fermi*−LAT 's bright γ-ray source list that collected sources with a significance of $\sim 10\,\sigma$ in the data of the first 3 months [88]. The *Large Area Telescope* (LAT) on board the γ-ray satellite is a pair-production telescope sensitive in the energy range

from below 20 MeV to more than 300 GeV (details can be found in [89]). η Carinae was detected in the soft ($0.1 - 10$ GeV) and hard ($10 - 100$ GeV) energy band [38]. The average flux observed was consistent with the *AGILE* result but a flare in 2008 could not be confirmed by *Fermi*−LAT . The full spectrum from $0.1 - 100$ GeV was fit by a combination of a cutoff power-law function for energies below 10 GeV with a power-law function for higher energies.

Orbital modulation was found in the full energy range (extended up to 300 GeV in 2012), but with different amplitudes below and above 10 GeV and, in general, less pronounced than in X-rays [90]. An increased flux level can be observed close to periastron, a decrease with growing separation between the primary and secondary star (compare figure 2.10 which shows the light curve for the first full orbit observations by *Fermi*−LAT). Different models have been proposed to account for the two distinct components in energy and will be revisited in section 2.6.3. The form of orbital modulation plays an important role as a diagnostic tool to evaluate models. Particle acceleration in the expanding blast wave of the Great Eruption in 1843, as suggested by Ohm et al. [91], is likely not the origin of the bulk of emission. The detection of orbital variability suggests acceleration near the binary system [90].

The first full orbit data set by *Fermi*−LAT confirmed the decrease of γ-ray flux for the high-energy component towards apastron (compare figure 2.10) [92]. For E $\gtrsim$ 10 GeV the γ-ray flux during periastron passage is significantly different from apastron. The last periastron passage in 2014 provided a good opportunity to test predictions made so far. With seven years of *Fermi*−LAT data, orbital modulation in the low energy flux was observed. The variability is of factor 2, compared to 3 - 4 for the high energy band. At periastron, when the high energy flux is at its maximum, the low energy flux experiences variability similar to the thermal X-ray band [93].

With a flux reaching up to 300 GeV, η Carinae is potentially in reach for a ground-based imaging γ-ray telescope like *H.E.S.S.* (see section 3.2 for a description of H.E.S.S.). Motivated by the detections of η Carinae in γ-rays by *AGILE* and *Fermi*−LAT , the binary system was observed by H.E.S.S. for ~ 60 h between 2004 and 2010 [94]. With an energy threshold of ~ 400 GeV, no emission was observed. With the installation of a new telescope in 2012 the energy threshold dropped significantly. A detection of very-high-energy (VHE) γ-rays from η Carinae would be the first of a CWB in this energy range. H.E.S.S. is better suited to observe variability on monthly timescales

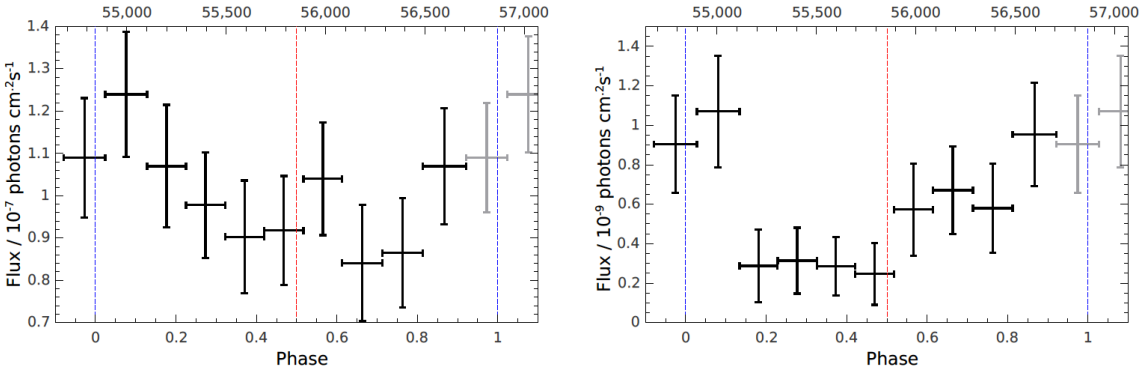

Figure 2.10: Light curve of η Carinae by *Fermi*−LAT from 0.2 to 10 GeV (*left*) and 10 to 300 GeV (*right*) [92]. The dashed vertical lines depict the time of periastron (blue) and apastron (red).

than *Fermi*−LAT due to the large collection area [95] and can probe the maximum energy to which particles are accelerated and study the acceleration emission.

2.6 Origin of γ-ray emission

γ-ray emission from the direction of the colliding-wind binary η Carinae has been observed up to 300 GeV [93]. For the production of high-energy γ-rays several ingredients are required: a relativistic particle population (hadronic or leptonic), an efficient acceleration mechanism, and target material or magnetic fields for interactions with the relativistic particles. Proposed mechanisms for the acceleration are discussed in the subsequent section, followed by the processes involved in the production of X-rays, high and very-high-energy γ-rays. The section concludes with an elaboration of the models for γ-ray emission from η Carinae.

2.6.1 Particle acceleration in colliding-wind binaries

The idea of particle acceleration in the interstellar medium was put forward by Enrico Fermi. He suggested that relativistic particles could gain energy by scattering off randomly-oriented magnetic field structures in interstellar clouds [96]. The main problem of this process is the efficiency of energy gain: it depends quadratically on the velocity of the magnetic cloud (as a fraction of c) that is hit and this fraction is usually very small [48]. This process is thus termed *2nd order Fermi acceleration*. A more efficient acceleration mechanism needs a more beneficial velocity dependence, e.g. first order. Such an efficient mechanism is proposed to take place in the environment of

astrophysical shock fronts and is termed *Diffusive Shock Acceleration* (DSA) [97, 98].It naturally gives rise to a power-law spectrum of the accelerated particles. *Shock* here refers to a transition layer that propagates through a plasma and compresses it, decreasing the mean plasma velocity. Cosmic rays perform a random walk on either side of the shock. Entering the shock environment upstream of the shock, they excite fluctuations in the magnetic field and can get reflected across the shock. Downstream of the shock they can scatter on magnetic field turbulences and cross the shock again. With every crossing, an energy of $\sim \frac{\Delta E}{E} \approx \frac{u}{c}$ is gained (with the velocity of the upstream plasma u) [99, 100]. A strong shock exhibits a *compression ratio* (ratio between the density of upstream and downstream gas), of $\chi = \frac{\rho_{\mathrm{down}}}{\rho_{\mathrm{up}}} = 4$ [31].

The collision of supersonic stellar winds in a binary system creates such strong shocks and should be able to efficiently accelerate particles to high energies [8]. In the collision, the high-speed winds produce hot gas separated by a contact discontinuity. Shocks form on either side of the contact discontinuity (the scenario is outlined in figure 2.11). The location where the shocks form is defined by the balance between the ram pressure of both winds $\rho_{\mathrm{Comp}}\, v^2_{\infty,\mathrm{Comp}} = \rho_{\mathrm{Primary}}\, v^2_{\infty,\mathrm{Primary}}$ (with gas densities ρ_i and terminal velocities v_∞) [35]. A long orbital period (large separation) like in η Carinae's case is necessary to enable the stellar winds to reach their terminal velocity. Most of the shock power is released downstream on both sides of the wind-collision region [35]. The magnetic field plays an important role in the acceleration process as well as in the particle interactions but is poorly constrained. A reasonable estimate of the magnetic field strength at the surface of the primary star is $\sim$100 G [101]. The choice of the magnetic field strength constrains the maximum energy of the accelerated particles, when modelling the emission.

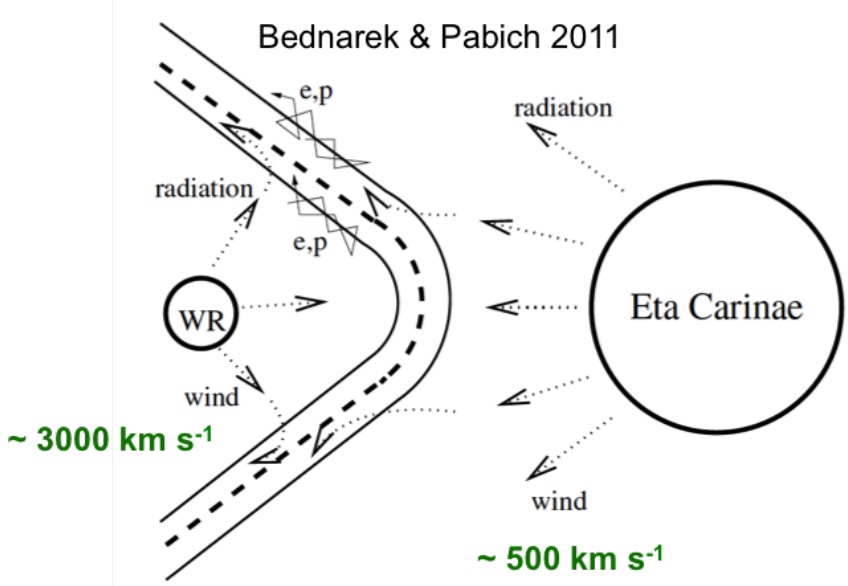

Figure 2.11: Schematic drawing of η Carinae: where the stellar winds collide, a contact discontinuity forms and shocks on each side build up. Particles from either star can get accelerated in the shock fronts. A shock cap around the companion star emerges because the wind pressure of the primary star dominates (source: [102]).

2.6.2 Non-thermal emission processes

When relativistic particles travel through space, non-thermal emission is produced

- in electromagnetic interactions with photon fields in inverse-Compton scattering,
- as Bremsstrahlung from relativistic electrons
- as Synchrotron radiation when a magnetic field forces a spiral motion upon the cosmic-ray particle,
- in hadronic interactions involving neutral pions.

In an **Inverse Compton** (IC) process a highly energetic electron scatters a low-energy photon and transfers a fraction of its energy. In case of CWBs there is a strong supply of UV and visible photons from the stars' photospheres which makes Inverse Compton scattering an important process. Relativistic electrons can 'boost' these soft photons to the X-ray and γ-ray regime. The energy loss of the relativistic electron is determined by

$$\left(\frac{dE_e}{dt}\right)_{IC} = \frac{4}{3}\gamma^2 \sigma_T c U_{rad} \tag{2.2}$$

with the Lorentz factor of the electrons γ and the energy density of the target radiation field U_{rad}. This is valid for $\sqrt{\mathrm{E}_{IC}\mathrm{E}_{soft}} \ll \mathrm{m_e c^2}$ (in the reference frame of the electron). In the regime where this relation holds (*Thomson regime*), Inverse Compton scattering is not only an efficient emission process of high-energy photons but also a loss channel for relativistic electrons [35]. Electrons with a Lorentz factor of $\gamma = 1000$ produce X-rays when scattering off far-infrared photons.

Considering VHE γ-rays with $\sqrt{\mathrm{E}_{IC}\mathrm{E}_{soft}} \gg \mathrm{m_e c^2}$, e.g. produced by electrons with energies of 10 TeV scattering off IR photons or 30 GeV scattering off visible light, energy loss is less severe due to the reduced quantum relativistic cross section (*Klein-Nishina-Regime*) [48]. The energy loss of the relativistic electron is reduced by the factor

$$f_{\mathrm{KN}} \approx (1+b)^{-1.5} \approx (1 + 40 E_{\mathrm{e,TeV}} k T_{\mathrm{eV}})^{-1.5}. \tag{2.3}$$

Synchrotron radiation is emitted by charged particles when interacting with a magnetic field. The Lorentz force (orthogonal to the magnetic field direction) pushes the particle on a helical path. The energy of the radiated photons depends on the energy density of the magnetic field U_B, the energy of the charged particle and the angle between the magnetic field direction and the particle path. The emitted power is ($\beta = \frac{v}{c}$

$$\left(\frac{dE_e}{dt}\right)_{sync} = 2\sigma_T c U_B \gamma^2 \beta^2 \sin^2\theta. \tag{2.4}$$

Synchrotron emission is important as a production mechanism for non-thermal X-rays. Since $\sigma_T \propto m^{-2}$, synchrotron radiation from protons is negligible.

In the picture of particle accelerating binaries, synchrotron emission also plays a role in the radio regime where some CWBs show non-thermal emission via synchrotron radiation (e.g. in the case of WR 140, compare section 2.4.1). η Carinae is not showing non-thermal radio synchrotron emission. This has been interpreted as a consequence of the *Razin-Tsytovitch* effect. In cold plasma the refraction index becomes < 1, which increases the beaming angle and reduces the emitted power [details in, e.g., 103, 104, 31]. The effect leads to suppression of radio synchrotron radiation.

Neutral pion decay from pp interactions. For hadrons, electromagnetic interactions have much lower cross-sections. Via strong interactions γ-rays are produced in the neutral pion channel $p + p \rightarrow \pi^0 + X$, $\pi^0 \rightarrow \gamma + \gamma$. γ-rays produced via neutral

pion decay show a characteristic 'pion bump' in their spectrum, which is centered at $E \sim 70\,\mathrm{MeV}$ in the rest frame of the neutral pion.

The observable flux of γ-rays at Earth will, however, also depend on energy losses of cosmic-rays via bremsstrahlung and the loss of γ-rays via pair production.
Bremsstrahlung, similar to synchrotron radiation, is emitted when a charged particle is accelerated in the Coulomb field of a nucleus or other charged particle [31]. In the γ-ray regime (non-thermal) bremsstrahlung only gives a minor contribution to the emission because the plasma densities are not sufficiently high [105]. Pair production through γ-γ absorption is the conversion of a photon into an electron-positron pair: $\gamma\,\gamma \rightarrow\ e^-\,e^+$. To ensure the conservation of momentum the photon has to be in the vicinity of a nucleus. The threshold energy for the process is the centre of mass energy of the pair. Processes of γ-ray emission also decrease the amount of particles that can get accelerated and are thereby counterbalancing the acceleration mechanisms ('cooling'). It is therefore important to evaluate the time scales on which energy loss takes place (compare section 4.3.8).

2.6.3 Modelling the γ-ray emission in η Carinae

Which emission and absorption processes are most important depends on the primary particle population, the particle energies, involved magnetic field strengths and target material densities. This leaves room for the modelling of observational results. As mentioned in section 2.5, orbital variability can act as a diagnostic tool to differentiate between models. Recent scenarios that take into account the two spectral components seen in *Fermi*-LAT data, are:

1. Two distinct spectral components as a result of leptonic and hadronic emission processes [33, 93]. The low-energy component has been attributed to photons of the photosphere which get up-scattered (IC) by relativistic electrons. The high-energy ($> 10\,\mathrm{GeV}$) tail is interpreted as relativistic protons interacting with the dense stellar wind in the shock. Only one shock is assumed and the model does not include the temporal evolution of the system. As the conditions in the photosphere and in the shock region differ along the orbit, phase locked variability would be expected in observations. The details of variability are determined by the changes in the density of relativistic protons and in photon-field energy density.

2. Production of γ-ray emission in η Carinae by a single electron population through IC scattering. The change in the spectrum at $10\,\mathrm{GeV}$ is interpreted as γ-γ ab-

sorption and re-emission. As absorbers are suggested X-ray gas surrounding the CWB or hot shocked gas inside the wind collision region [90].

3. Instead of treating the wind-collison region as one, two shocks, one on the primary and one on the companion side, are considered with their respective properties like proposed by Bednarek and Pabich [102]. Time-dependancy is taken into account for particle acceleration and interactions of relativistic electrons and protons. Emission in low and high energy band are explained as originating in hadronic interactions [106]. Emission above 10 GeV is dominated by protons accelerated in the shock on the companion side that leave the system along the contact discontinuity, interacting in the post-shocked region. The low energy emission is due to calorimetric radiation on the primary side.

Chapter 3

Measuring VHE γ-rays from η Carinae with H.E.S.S.

The GeV energy range is where space-based γ-ray instruments like $Fermi-$LAT reach their limits due to the small photon collection areas. By lowering its energy threshold H.E.S.S. aimed to close the gap between space- and ground-based γ-ray instruments. The addition of a 28 m diameter telescope in 2012 brought a significant improvement in sensitivity to low energies: H.E.S.S. is sensitive to γ-ray emission in photon energies from ~ 30 GeV to tens of TeV. For the case of η Carinae, as well as other CWBs, this is particularly important because it is expected that the energy spectrum only extends to a few hundred GeV [e.g. 35, 102, 106]. For H.E.S.S., this is still in the low energy domain of the instrument. The energy threshold depends, among other quantities, on the level of background, which will be discussed further in the course of this chapter.

The UV emission of the Carina nebula poses an extraordinary background to the measurement of VHE γ-ray emission. The average Galactic night sky background (NSB) in the H.E.S.S. field-of-view is ~ 100 MHz, around η Carinae the background is up to 10 times as strong and varies greatly across the FoV [107]. This poses challenges on observations and every level of data processing, from calibration to data analysis. The working hypothesis of this work was to eliminate as much NSB as early as possible in the analysis chain and minimize its impact on the high-level analysis results.

In the beginning of this chapter the H.E.S.S. experiment will be portrayed. The calibration procedure of H.E.S.S. is introduced next. After data calibration, reconstruction methods are needed to retrieve information about the original particle that induced

the Cherenkov shower, from the shower image in the camera. With the reconstructed properties of the primary particle, background and signal can be discriminated. In this work, the Hillas and Model Analysis reconstruction methods are applied and will be explained. Finally, the extraction of the signal and generation of the spectral energy distribution will be presented. The influence of the NSB will be evaluated throughout the data processing and steps taken to tackle it will be described.

3.1 Principle of γ-ray detection with IACTs

Imaging Atmospheric Cherenkov Telescopes (IACTs) like H.E.S.S. measure Cherenkov radiation emitted by charged secondary particles travelling with a velocity greater than the phase velocity of light in the atmosphere [108]. By reconstructing the properties of the original γ-rays it is possible to trace them back to their source. The source can then be studied by, e.g. analysing the spectral energy distribution and the spatial distribution of the γ-ray emission. The secondary particles are created when a γ-ray enters the Earth's atmosphere and interacts with the Coulomb field of an atmospheric nucleus, leading to the production of an electron-positron pair. Both, the electron and the positron produce photons via Bremsstrahlung, which will again undergo pair production. The process continues, producing an (electromagnetic) shower of particles, until the critical energy is reached and ionisation starts to dominate the process.

Showers induced by hadronic particles constitute an important background, outnumbering γ-ray induced showers by a factor of $\sim 10^5$ [109]. Due to additional weak- and strong-force interactions, hadronic showers entail π and K mesons, μ (from decay of charged π and K), neutrinos (from decay of charged π, K and μ) and tend to illuminate broader areas on ground compared to electromagnetic (EM) showers with a primary particle of the same energy. Roughly two thirds of the produced particles are charged particles, one third are neutral particles (π^0, which will further decay to two γ). Details about hadronic interactions can be found in e.g. [110].

Cherenkov radiation forms a cone-like shock front with an opening angle $\theta_C = \arccos\left(\frac{c}{vn}\right)$ with respect to the direction of movement of the emitting particle (with the refractive index n, the velocity v and the speed of light c). The typical opening angle of the light cone is $\sim 1\,^\circ$ for γ-ray induced showers. The charged particle induces dipoles in the air which emit spherical waves when relaxing. These interfere constructively and form the Cherenkov cone. The number of emitted Cherenkov photons is proportional to

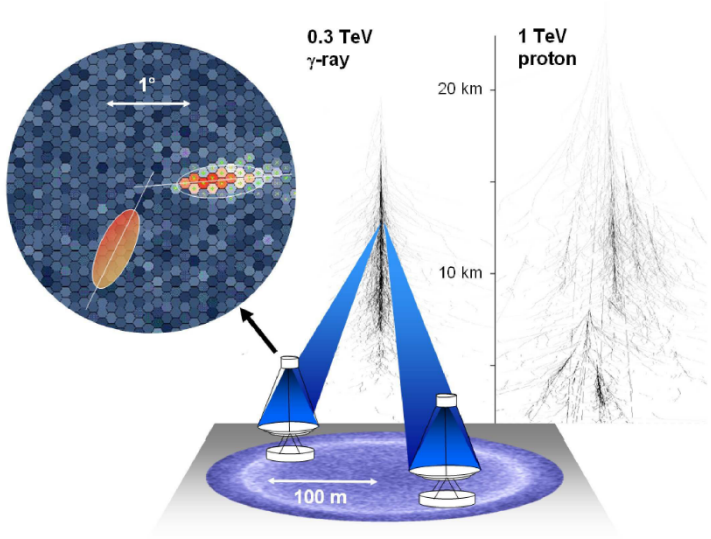

Figure 3.1: A γ-ray primary of 0.3 TeV induces an EM shower at ∼ 10 km height. The light pool created by its Cherenkov light illuminates a circle of ∼ 100 m radius. In the field-of-view of the camera of the telescope, the Cherenkov photons leave an elliptical imprint. The arrival direction can be reconstructed by intersecting the shower ellipses in the telescopes if several telescopes are observing. This topic is covered in section 3.4. Image taken from [100].

the energy of the primary particle. Measuring the number of Cherenkov photons thus gives an indirect measurement of the primary particle's energy. The emission lasts only a few nanoseconds.

In a shower, the Cherenkov light cones of the secondary particles add up and form a pool of light on the ground. For a γ-ray primary of 0.3 TeV, the light pool reaches its maximum photon density at a radius of ∼ 100 m (compare figure 3.1). The mirror dishes of the telescopes placed within the light pool collect the light and focus it into the camera to take an image of the shower.

3.2 The High Energy Stereoscopic System

The analysis presented in this work was carried out with data obtained with the H.E.S.S. telescopes. The **H**igh **E**nergy **S**tereoscopic **S**ystem, named after the pioneer of cosmic-ray physics Viktor Hess [111], has been in operation since 2004 (phase H.E.S.S.-I, [112, 113]), and in its current shape, with five telescopes, since 2012 (phase H.E.S.S.-II, [114]).

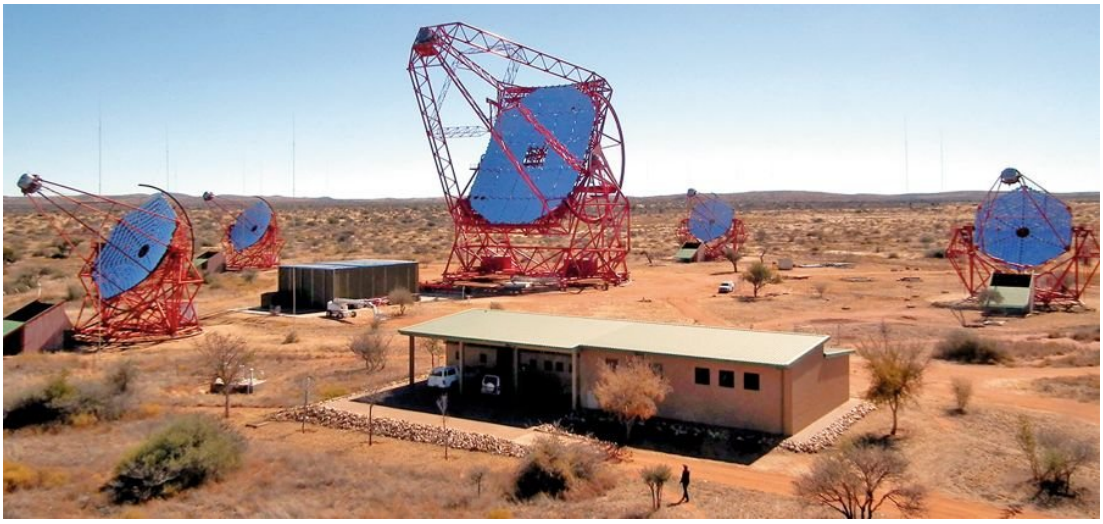

Figure 3.2: H.E.S.S. telescope array with CT5 in the centre. Picture by Mathieu de Naurois.

H.E.S.S. consists of five IACTs using Earth's atmosphere as a calorimeter for the detection of high-energy γ-rays on ground. The telescopes are located in Khomas Highland, Namibia, which makes H.E.S.S. the only IACT able to observe a large fraction of the Southern hemisphere. There are four identical telescopes (CT1-4) equipped with a dish of spherical mirrors of 12 m diameter, resulting in a total mirror area of 107 m^2. They are placed in a square of 120 m side length, because the Cherenkov light imprint on ground is about 250 m in diameter for a typical γ-ray shower. The focal length of CT1-4 is f_{CT1-4} =15 m. The biggest telescope, CT5, is located in the centre of the array. It has a mirror dish of 28 m diameter and a total mirror surface of $\sim$ 614 m^2. The focal length of CT5 is f_{CT5}=36 m. All telescopes are alt-azimuth mount Davies-Cotton reflectors [115]. Figure 3.2 shows the array with unparked telescopes during daytime. H.E.S.S. is currently the only IACT integrating telescopes of different sizes into its system.

The four cameras of the first generation telescopes comprise 960 photo-multipliers each with a field of view (FoV) of 0.16 °, in the following called pixels. The fifth telescope is equipped with 2048 pixels with a FoV of 0.067 °, respectively. The FoV of the four H.E.S.S.-I telescopes is 5 ° in total, the fifth telescope has a FoV of $\sim$3.2 ° [116, 114]. On every pixel a Winston cone is installed to focus the light [117]. To get a precise image of the shower fast electronics (for background rejection) and a fine grid of pixels are necessary. In every pixel the signal is split into a trigger channel and two sampling channels, with low or high amplification factors (*high gain* and *low gain* channels). From high-

and low-gain the signal is sent to an analogue memory. The trigger in a single camera acts when a threshold intensity S_1 (first level trigger) is exceeded by at least S_2 pixels in the same sector (second level trigger).

Observations with H.E.S.S. are carried out in bunches of 28 min called *run* during astronomical darkness. Only the moonless hours of the night are suited for observations with H.E.S.S. to avoid the night sky background from the moon. With these constraints roughly 1000 h of observation time are available per year. The H.E.S.S. telescopes typically operate in **stereoscopic** mode (CT5 and at least one of CT1-4) or in **monoscopic** mode (only CT5). During the observation they are pointed slightly offset the source position and track the position in the sky (further explanations about the pointing in section 3.5). The pointing accuracy varies between $\sim 6''$ for dedicated observations with CT1-4 [118] and $\sim 36''$ for standard monoscopic observations and analysis with only CT5 [119]. The angular resolution (or *point spread function*, PSF) of H.E.S.S. depends on observation conditions (e.g. night sky background, zenith angle) and reconstruction and analysis methods. For a standard analysis with CT1-4, the angular resolution $\vartheta^2_{CT1-4} = 0.01\,\mathrm{deg}^2$ [107], while the standard monoscopic analysis yields a slightly worse angular resolution of $\vartheta^2_{CT5} = 0.03\,\mathrm{deg}^2$ [120].

To minimize a potential risk for the cameras when pointing at the bright Carina nebula the pixel thresholds were scanned and custom pixel trigger criteria were defined for observations on η Carinae. The pixel trigger criteria also play a mayor role in suppressing NSB photons right at the instrument level. By increasing the threshold intensity value for CT5 to $S_1 = 4.5$ photo-electrons (p.e.) compared to 4.0 in normal observation mode, the accidental camera trigger rate due to NSB photons can be reduced to a standard level of ~ 3.5 kHz. When the second level trigger decides in favour of an event, the signal is digitized and integrated over 16 ns for the high- and low-gain channel respectively and sent to the central trigger. In stereoscopic observation mode, there is another trigger level at the central trigger to connect multiple telescopes. This trigger is passed if at least two telescopes were triggered within 80 ns. The signal is further processed and saved to disk. A data acquisition system (DAQ) ensures smooth operation of the telescopes by controlling and coordinating the telescopes' subsystems (e.g. cameras) and monitoring the instrument's behaviour. It is described in more detail in [121].

After observations, the raw data that is still in Analogue-Digital-Converter counts,

Figure 3.3: The fifth telescope, which was added in 2012, in twilight (September 2017). On the left hand side, the mirror facets, which form the dish. Situated at the end of the leverage on the right is the camera.

needs to be converted into a physical meaningful unit. This process and the role and treatment of night sky background at this stage are described in section 3.3. The reconstruction of the primary γ-ray from the measurement of the Cherenkov shower photons is discussed in section 3.4. Two possible methods and how they react to night sky background are introduced, the Hillas method (section 3.4.1) and the Model Analysis (section 3.4.2).

3.3 Calibration of raw data

Before the recorded electronic signals can be interpreted, they need to be converted from Analogue-Digital-Converter (ADC) counts to a more physically meaningful unit, which is the number of Cherenkov photons per pixel. This quantity can later be used to infer the particle energy. The calibration procedure includes the gain calibration of the photo-multipliers, the relative calibration between low- and high-gain electronics, the pedestal determination and the conversion of electronic signal into detected photo-electrons, which are further converted into Cherenkov photons. It is described in detail in [116, 114, 122]. The H.E.S.S. collaboration uses two independent calibration chains to be able to cross-check results. In the following a short description of the *French* calibration procedure is given.

The intensity in the high-gain channel I_{HG} and the intensity in the low-gain channel I_{LG} in photo-electrons is described by

$$I_{HG} = \frac{ADC^{HG} - p_{HG}}{\gamma_e} \times FF \qquad I_{LG} = \frac{ADC^{LG} - p_{LG}}{\gamma_e} \times \frac{HG}{LG} \times FF \tag{3.1}$$

with $ij = HG, LG$ and

- the amplitude ADC^{ij} in ADC counts, measured for every event
- the gain of the high-gain channel for a single photo-electron γ_e in ADC counts/p.e.
- the position of the pedestal p_{ij} in ADC counts
- the amplification ratio of high-gain to low-gain $\frac{HG}{LG}$
- the flat-field coefficient FF.

To obtain the parameters for the conversion dedicated calibration runs are performed. The gain γ_e and the ratio $\frac{HG}{LG}$ are obtained via *SinglePe* runs. *SinglePe* runs are performed with CT1-4 parked inside the shelter to avoid night sky background contamination and only for the high-gain channel. The high-gain channel is capable of measuring single photo-electrons. An LED flash light is used that can generate single photon events inside the camera pixels. The camera of CT5 has to be unloaded and brought to its shelter for this procedure. This distribution describes the response of the photo-multipliers to the LED flash light. It is a combination of the pedestal, described by a Gaussian function of width σ_p and mean p_{HG}, the photo-electron number n, following a Poisson distribution and the distribution of a signal of n p.e., described by a Gaussian function of width $\sqrt{n}\sigma_\gamma$ and mean $p_{HG} + n\gamma_e$:

$$G(x) = N\frac{e^{-\mu}}{\sqrt{2\pi}\sigma_p}\exp\Big(-\frac{(x-p_{HG})^2}{2{\sigma_p}^2}\Big) + N \times N_s \sum_{n=1}^{m\gg 1} \frac{e^{-\mu}}{\sqrt{2\pi n}\sigma_p}\frac{\mu^n}{n!}\exp\Big(-\frac{(x-(p_{HG}+n\gamma_e))^2}{2n{\sigma_\gamma}^2}\Big). \tag{3.2}$$

In eqn. 3.2, N is the number of triggers, N_s a normalisation factor and μ is the average number of photo-electrons per trigger. This function is fitted to the ADC count distribution of each pixel averaged over one observation period (the period between full moon occurrences) and the fitted value of γ_e is used in equation 3.1. In the high-gain channel there are $\gamma_e \approx 80$ ADC counts difference between the electronic pedestal and the signal from a single photo-electron. The electronic pedestal width is typically 20% of a photo-electron $\sigma_{p0} \approx 16$ ADC counts per photo-electron. It is monitored with dedicated calibration runs, the *ElectronicPedestal* runs. The amplification ratio $\frac{HG}{LG}$ is inferred from the intensity ratio in the linear range of the high-gain and low-gain channel. Figure 3.4 depicts an exemplary distribution of ADC counts obtained during *SinglePe* runs

averaged over one observation period.

The flat-field coefficient FF compensates for different quantum efficiencies and light collection efficiencies and also for differing signal gains in each pixel. It represents the deviation of the pixel response regarding the average pixel response in the camera. It is determined via *FlatFielding* runs. During *FlatFielding* runs, the cameras are illuminated with a homogeneous light source providing every pixel with the same amount of light. The obtained distributions are averaged over one observation period for every pixel. The pixel-wise mean width divided by the mean of the whole camera delivers the flat-field coefficient for the respective pixel.

The pedestal position p_{ij} is determined in each channel as the mean value of ADC counts measured in absence of Cherenkov light. To obtain it, the pedestal in all pixels without Cherenkov signal is recorded during standard observation runs. The pedestal width σ_p is constituted by the electronic pedestal width σ_{p0}, the resolution of the PMTs (width of single p.e. peak) σ_γ and NSB. In figure 3.5 the evolution of the pedestal width for different levels of NSB is shown. The pedestal width increases with an increase in NSB. The rate of NSB photons in photo-electrons per second can be determined as follows (for an acquisition window $\Delta t = 16\,\text{ns}$ and a high-gain $\gamma_e = 80\,\text{ADC}\,\gamma_e^{-1}$):

$$r_{NSB} = \frac{(\sigma_p^2 - \sigma_{p0}^2 - \sigma_\gamma^2)}{\gamma_e^2 \times \Delta t} \tag{3.3}$$

The pedestal evolution is also monitored because the exact determination is crucial for the identification of photo-electrons (compare 3.1). It is recalculated if the average position of at least four pixels in the camera has moved by more than 10 ADC counts. Also the gradient of the pedestal is calculated. NSB measurement with PMTs is further described in detail in [116].

The high rate of photons induced by NSB leads to two effects:

- NSB photons can accidentally simultaneously arrive at neighbouring pixels of a pixel triggered by a background photon (first level trigger) and thus help it pass the second level trigger.
- When first and second level triggers are passed, the integration time window of 16 ns will unavoidably include NSB photons that arrived at the pixel within this time frame. This holds also for triggers of background events. The consequence is

that the intensity in every pixel includes a fraction of NSB photon intensity which boosts γ- and background events to higher intensities.

As a first measure, this is addressed by the raised trigger pixel threshold. Still, there is a remaining contribution of NSB photons on top of each γ-ray signal, which will be studied carefully. To further convert photo-electrons into a number of Cherenkov

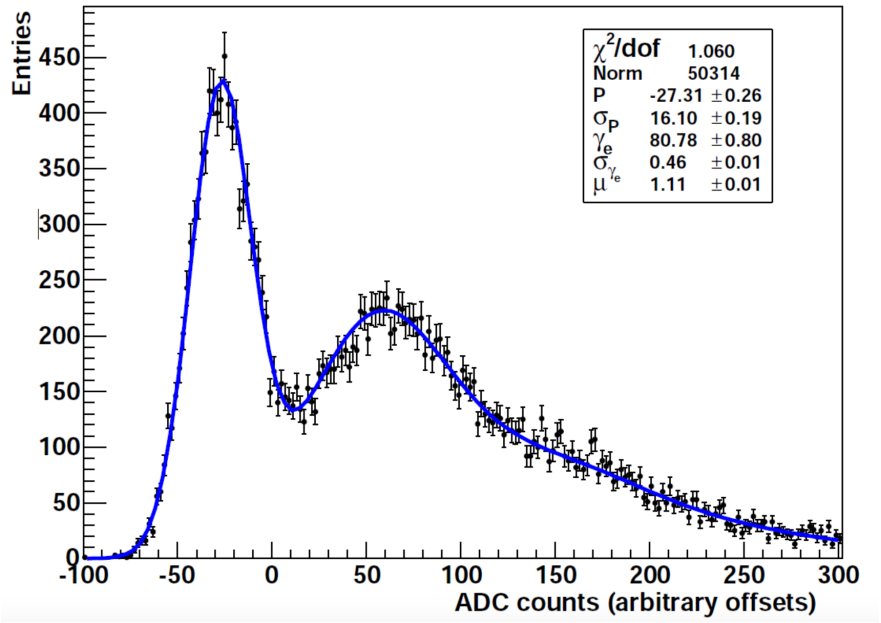

Figure 3.4: Example of a SinglePeRun used for the translation of ADC counts to photo-electrons together with the fitted PMT response function. The narrow peak to the left is due to the electronic pedestal. The broader peak to the right is the single photon-electron peak. *SinglePe* runs are performed every observation period. Image taken from [123].

photons, the overall optical transmission efficiency (including Winston cones, mirrors, atmosphere) is needed. This conversion factor can be obtained based on measuring the properties of muon induced shower images. Muons produce Cherenkov showers that resemble γ-ray induced showers and their Cherenkov radiation can be calculated analytically. By comparing the calculated muon induced Cherenkov radiation with the measured muon induced Cherenkov radiation the loss of Cherenkov photons at the telescopes can be inferred. Details about this method can be found in [123].

After the successful translation of ADC counts to Cherenkov photons the next step is to reconstruct the properties of the γ-rays inducing the Cherenkov showers.

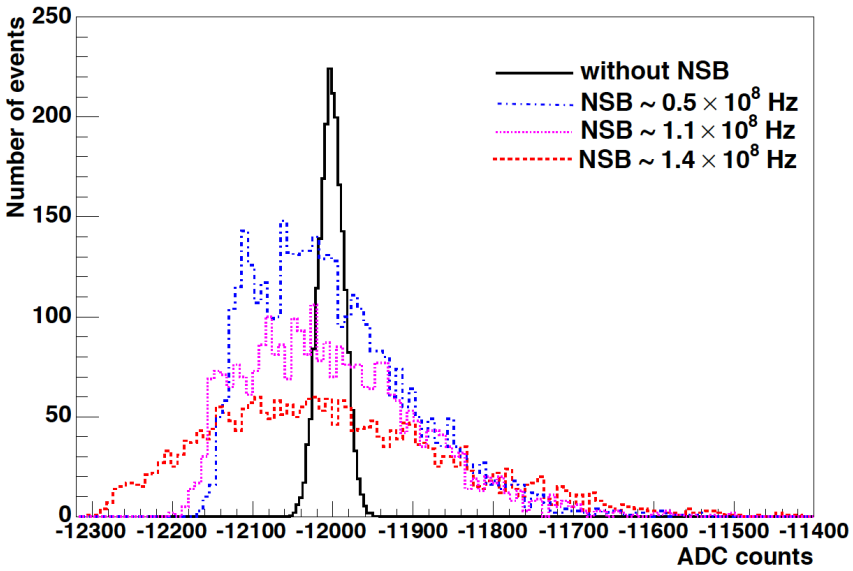

Figure 3.5: Pedestal distributions for different NSB levels. The pedestal's peak position shifts towards negative values and the distribution broadens because there are several photoelectrons within the integration window. Image taken from [116].

3.4 Air shower reconstruction and treatment of NSB

To gain information about the primary γ-ray (energy, direction) from the Cherenkov shower on the ground, reconstruction procedures are used. The pioneering procedure, the Hillas method, applies a parametrization based on the ellipse-like shape of the shower image [124]. This method has successfully been used for decades now [e.g. 125]. With the advancement of IACTs, also the methods for reconstruction have developed and improved the instruments' sensitivities. The Model Analysis applies a semi-analytical model to describe the Cherenkov light distribution of charged particles in electromagnetic showers [126, 107]. Another way to improve performance is to compare measured shower images with a bank of shower templates realising different sets of shower parameters. For the generation of the shower templates Monte Carlo simulations can be used. This is the case for the second analysis chain in H.E.S.S. [127, 128], which uses the CORSIKA/*sim_telarray* chain [129, 130].

In this work, the Hillas and Model Analysis reconstructions are applied and will be explained in the following.

3.4.1 Reconstruction with Hillas parametrization

Hillas-based reconstructions act on cleaned camera images. Ideally, only information in pixels contained inside a shower ellipse is taken into account. A standard way of cleaning an image is based on two thresholds: a pixel is kept, if its intensity is above threshold s_1 and it has a neighbour with intensity bigger than threshold s_2. Standard cleaning levels are (s_1,s_2) = (3,6),(4,7),(5,10) (in the unit of photo-electrons). For the application on η Carinae, the standard cleaning levels were extended by a stricter set of (6,12) p.e.

The image of a Cherenkov shower in the telescope's field-of-view can be approximately described by an ellipse (compare fig. 3.1). The ellipse is characterised by its moments (Hillas parameters) and additional parameters:

- Width w (semi-minor axis) and length L (semi-major axis) of the ellipse
- Size s: sum over image amplitudes $s = \sum_{i=1}^{n} a_i$, with pixel intensity a_i, n number of pixels
- *Centre of gravity (CoG)*: barycentre of the pixels in the shower concerning measured intensity, with the mean of the pixel coordinates (x_i,y_i)

$$\langle x \rangle = \frac{\sum_{i=1}^{n} x_i a_i}{\sum_{j=1}^{n} a_j} \quad \langle y \rangle = \frac{\sum_{i=1}^{n} y_i a_i}{\sum_{j=1}^{n} a_j}, \quad CoG = \begin{pmatrix} \langle x \rangle \\ \langle y \rangle \end{pmatrix}. \tag{3.4}$$

- Nominal distance R, which is the angular distance between the camera centre and the CoG of the image
- The angle ϕ, the azimuth angle of the main axis of the ellipse
- The angle φ, which describes the orientation of the Hillas ellipse with respect to the camera centre in the camera plane

The reconstruction of the direction of the primary γ-ray that induced a shower (the source position) is calculated in the *Nominal System*. The *Nominal System* is a 2D Cartesian system describing positions in the focal plane of a telescope. The orientation of x- and y-axis are as followed: for an azimuth angle $\phi = 0\,^\circ$ and altitude of $90\,^\circ$, the x-axis is facing north and the y-axis is facing west. A detailed description of the coordinate systems used within the H.E.S.S. software is given in [131]. The arrival direction of the primary photon can be reconstructed by intersecting the main axes of the shower ellipses in different telescopes (if CT5 and at least one of CT1-4 participated in the observation). The main axis of a shower is defined by the CoG of the shower and the angle φ (orientation with respect to the camera centre).

In the single-telescope case, the arrival direction can be determined from the asymmetry in the intensity distribution of the Hillas ellipse. This is possible because the intensity distribution in a shower is usually peaked towards the source direction, as depicted in figure 3.6. γ-rays are simulated for a variety of energies E, impact distances R and first interaction depths T (and for each shower they induce, the size s, length L and width W is calculated. Additionally, the asymmetry of the intensity distributions δ is determined in the monoscopic case. The calculated parameters (s, L, W) can then be filled into a table together with the corresponding true (simulated) properties (E, R, δ) and serve as a *look-up table*. The direction of the γ-ray can be calculated with the asymmetry parameter δ. A detailed description of the calculation of δ and the reconstruction of the arrival direction with it in the monoscopic analysis is given in [120].

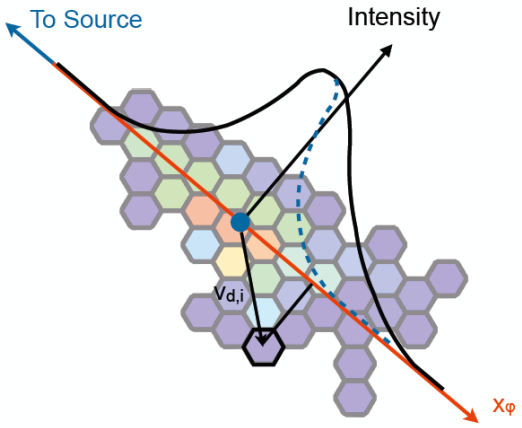

Figure 3.6: Sketch of a shower image inside a camera. The colour scale depicts intensity in p.e. with the maximum intensity in red. Overlaid in black is the intensity distribution with a peak towards the source direction. The dashed blue line shows how a symmetric intensity distribution would look like. Image taken from [120].

Discrimination between γ-ray showers and showers induced by cosmic rays can be accomplished by applying cuts on length and width of the shower ellipse, making use of the differing shapes of hadronic and electromagnetic showers (see section 3.1). The scaled width SW and scaled length SL

$$SW = \frac{w(s,R) - \langle w(s,R)\rangle}{\sigma_w(s,R)} \quad SL = \frac{L(s,R) - \langle L(s,R)\rangle}{\sigma_L(s,R)} \tag{3.5}$$

are considered here, in which the actual length and width are compared to the expectation value and variance from simulations of γ-rays. For stereoscopic reconstruction, the sum of all scaled widths (lengths) for all telescopes is calculated and divided by $\sqrt{N_{Tel}}$.

γ-ray showers exhibit a peak at 0 in the mean scaled width and length distributions with a root mean square (RMS) of 1.

More advanced reconstruction techniques have been developed in the last decade. In H.E.S.S. two widely-used techniques are based either on a semi-analytical model of the shower development [122] or multi-variate analyses [132, 127]. In the following subsection, the first technique, the Model Analysis, will be presented.

3.4.2 Reconstruction with Model templates

The Model Analysis is based on a semi-analytical model for the electromagnetic shower development in the atmosphere to infer the properties of the primary particle [107]. Monte Carlo simulations of the Cherenkov emission of every particle inside the shower are performed using the software package KASCADE [133]. The longitudinal, lateral and angular distributions of charged particles in the shower are derived from Monte Carlo simulations and parametrized in order to achieve an analytical description of the Cherenkov light density distribution in the camera [a detailed description of the parametrization can be found in 122, 107].

Model template generation

The analytical expression of the Cherenkov light density distribution is an eight-dimensional integral [107]:

$$
\begin{aligned}
I(x,y) = & \int \mathrm{d}z \int \mathrm{d}E' \times \frac{\mathrm{d}\mathcal{N}_e}{\mathrm{d}E'}(t,E') \times \frac{\mathrm{d}t}{\mathrm{d}z}(y) \\
& \int \mathrm{d}u \times F_u(u(E',s)) \int \frac{\mathrm{d}\phi}{2\pi} \\
& \int \mathrm{d}X_r \int \mathrm{d}Y_r F_{XY}(X_r,Y_r,E',s,u) \\
& \int \mathrm{d}\phi_{ph} \int \frac{\mathrm{d}\lambda}{\lambda^2} \frac{\mathrm{d}^2 n_\gamma}{\cos\theta \mathrm{d}z \mathrm{d}\lambda} \times \exp(-\tau(z,\lambda)) \times Q_{\mathrm{eff}}(\lambda) \\
& \times Col(z,X_r,Y_r,u,\phi,\phi_{ph})
\end{aligned}
\tag{3.6}
$$

This includes the integral over

- The longitudinal shower development: altitude z, energy E' of the electron/positron in the shower, atmospheric depth t and longitudinal distribution of charged shower particles $\mathrm{d}\mathcal{N}_e/\mathrm{d}E'$

- The angular shower development: (rescaled) electron/positron direction angle u with respect to shower axis, second direction angle ϕ (angle between x-axis of camera system and main axis of the shower ellipse), normalised angular distribution of particles $F_u(u(E',s))$ with s being the shower age, defined to be 0 at $t = 0$ and 1 at the maximum shower energy

- the lateral shower development: (rescaled) lateral coordinates X_r,Y_r, normalised lateral particle distribution $F_{XY}(X_r, Y_r, E', s, u)$ with respect to its direction

- $1/\lambda^2 \, \mathrm{d}^2 \, n_\gamma / \cos\theta \, \mathrm{d}z \, \mathrm{d}\lambda$ rate of Cherenkov photon production for electron/positron with angle θ to shower axis

- The atmospheric absorption described by $\exp(-\tau(z, \lambda))$ with the optical depth τ

- The detector quantum efficiency $Q_{\mathrm{eff}}(\lambda)$, including the mirror reflectivity

- The average geometrical detection efficiency $Col(z, X_r, Y_r, u, \phi, \phi_{ph})$ for Cherenkov photons emitted at position (X_r, Y_r,z) in direction (u, ϕ) and with angle ϕ_{ph}, azimuth angle of Cherenkov photon to shower direction

Beside the shower development, instrumental effects, like the electronic response of the camera or the point spread function, and other effects like atmospheric absorption of light, quantum efficiencies of the PMTs and the mirror size and shape are simulated.

The outcome of the shower model is a set of two-dimensional histograms, the model templates. They are produced for a variety of zenith angles θ_i between 0 and 56 deg, with a finer spacing for larger zenith angles, following $\theta_i = \arccos\left(\frac{1}{1+i/20}\right)$ with i = 0,1,...,16. For each θ_i, 40 impact distances, between 0 m and $(400/\cos\theta_i)$ m, 65 energies from (5 $/\cos\theta_i$) GeV to (80 $/\cos\theta_i$) TeV and 12 first interaction depths from 0 to 5 (in units of radiation lengths) are produced.

The next step in reconstructing the characteristics of the primary γ-ray is the comparison between data and the prediction of the model templates for a given set of energy, impact distance and first interaction depth. A log-likelihood minimisation is used to find optimised parameters for energy, depth of first interaction and impact distance.

Log-likelihood fit

The probability density to observe a signal intensity of s in a pixel for an expectation value μ (from the model templates) is described by [107]

$$P(s|\mu,\sigma_p,\sigma_\gamma,\sigma_c) = \sum_n \frac{\mu^n e^{-\mu}}{n!\sqrt{2\pi(\sigma_p^2 + n\sigma_\gamma^2 + n^2\sigma_c^2)}} \exp\left(- \frac{(s-n)^2}{2(\sigma_p^2 + n\sigma_\gamma^2 + n^2\sigma_c^2)} \right) \quad (3.7)$$

with pedestal width σ_p, single photo-electron peak width σ_γ and calibration uncertainty σ_c. The first term, the Poisson distribution, represents the distribution of the number of Cherenkov photons n. The second term expresses the photo-multiplier resolution.

In eq. 3.7 the width of the photo-electron peak σ_γ and the pedestal width σ_p correspond to the measured values for the individual pixel. In case of a signal that was induced by NSB photons, the probability density function is a Gaussian of width σ_p. Figure 3.7 shows the probability density function for $\sigma_p = 0.3\,\mathrm{p.e.}$, $\sigma_{ph} = 0.4$, $\sigma_c = 0$.

The intensity s_i in each pixel is collated with the prediction from the model templates for the current pixel. For values lying between templates, the templates are interpolated. The log-likelihood

$$\ln L = \sum_{\text{pixel}\,i} \ln L_i = \sum_{\text{pixel}\,i} -2 \times \ln P(s_i|\mu_i,\sigma_p,\sigma_\gamma,\sigma_c). \quad (3.8)$$

is minimised to find the best fit parameters.
To avoid local minima, it is necessary to find good starting parameters. These are delivered by the earlier described Hillas method (compare sec. 3.4.1). The observed signal is compared with showers for different realisations of $\mu, \sigma_p, \sigma_\gamma$ and σ_c for the starting parameters (size s, width w, length L). Besides the starting parameters provided by Hillas analyses with different cleaning levels, additional starting parameters with rotated direction angles are supplied in the single-telescope case. For each set of starting parameters the log-likelihood minimisation is carried out twice, first with a fixed first interaction depth, because the Hillas method does not provide it, then it is left as a free parameter. The log-likelihood of all fits is compared and the one with the lowest $\ln L$ is kept. This $\ln L$ is now based on a cleaned image, because the starting parameters are derived from a Hillas reconstruction. To regain the information lost in the cleaning, the fitting process (first with fixed first interaction depth, then left free) is repeated on all functional camera pixels. Depending on the involved telescopes, the log-likelihood

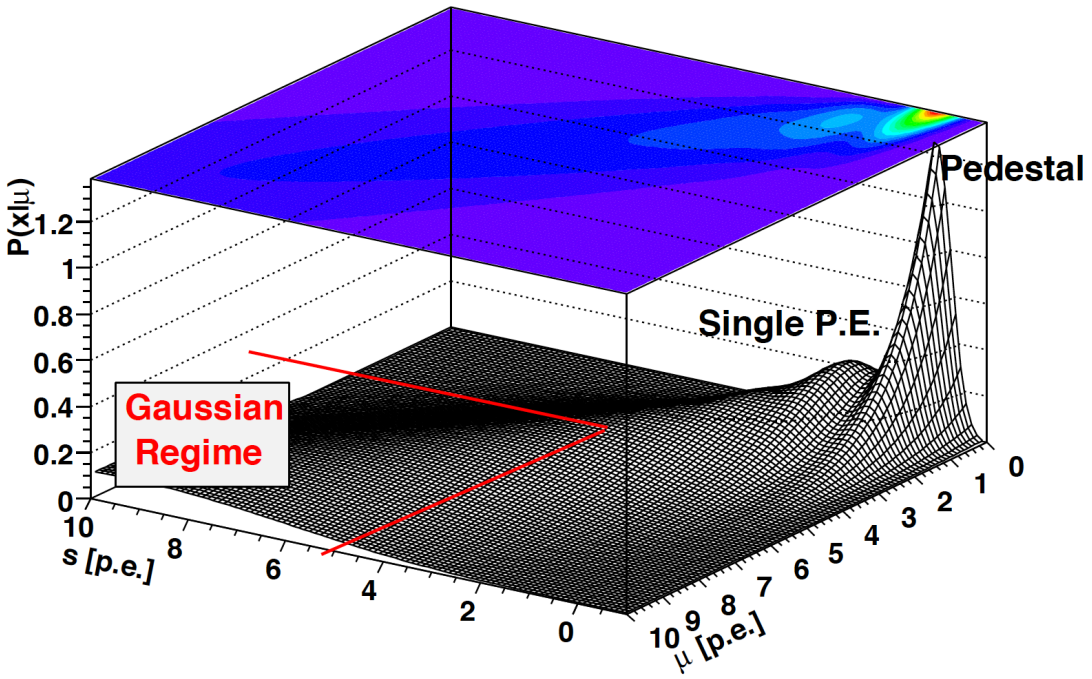

Figure 3.7: Visualisation of the probability density $P(s|\mu, \sigma_p, \sigma_\gamma, \sigma_c)$ for $\sigma_p = 0.3\,\text{p.e.}$, $\sigma_{ph} = 0.4$, $\sigma_c = 0$. Image taken from [107].

incorporates one to five telescopes. A detailed description of the minimisation process can be found in [122, 107].

The result of the minimisation are best-fit estimates for the shower parameters of the primary γ-ray

- impact distance d
- direction in (x,y) and angle φ
- energy E
- depth of first interaction T,

the final log-likelihood value and the correlation matrix of the fit parameters.

After reconstructing the properties of the primary particle under the assumption that it is indeed a γ-ray, it remains to be checked whether this holds true. Apart from NSB, which is incorporated in the fit, hadronic showers are the main source of background and have not been treated so far. Based on their abundance, it is safe to assume that many showers making it into the fit are induced by hadrons and not γ-rays (compare sec. 3.1).

Discrimination between γ-ray showers and background

The dominant background for IACTs are showers generated by charged cosmic rays, mostly protons, in the Earth's atmosphere. Since these are much more numerous than γ-ray showers, the performance of an IACT analysis method depends on its ability to differentiate between γ-ray showers and background. The Model Analysis provides further background suppression through cuts on goodness-of-fit variables [107]. As the name suggests, the goodness-of-fit G is a measure for the agreement between model prediction and shower images in the data (still under the assumption of a γ-ray as primary particle). It is defined as the normalized sum over the difference between the pixel log-likelihood and the average pixel log-likelihood

$$G = \frac{\sum\limits_{\text{pixel } i} \left[\ln L(s_i|\mu_i) - \langle \ln L \rangle|_{\mu_i} \right]}{\sqrt{2 \times \text{NdF}}}, \tag{3.9}$$

normalized with the number of degrees of freedom NdF. In equation (3.9), the average pixel log-likelihood reads

$$\langle \ln L \rangle|_{\mu} = \int \mathrm{d}s \ln L(s|\mu) \cdot P(s|\mu), \tag{3.10}$$

with the probability density function $P(s|\mu)$ defined in equation (3.7). For $\mu \gg 0$, G behaves asymptotically like a χ^2 distribution. If the pixel log-likelihoods behave like independent random variables, the goodness G is expected to behave like a normal variable with $\langle G \rangle = 0$ and $\sigma^2(G) = 1$. As this is not always the case, G is rescaled with the mean and root mean square (RMS). Depending on the choice of the pixels, different goodness variables are defined. An important variable for background rejection is the mean scaled shower goodness $\langle SG \rangle$, which takes only pixels inside the shower ellipse plus three rows of neighbouring pixels into account:

$$\langle SG \rangle = \frac{SG - \langle SG_{exp}(s,d) \rangle}{\sigma_{SG_{exp}}(s,d)}. \tag{3.11}$$

The mean expected shower goodness $\langle SG_{exp}(s,d) \rangle$ and RMS $\sigma_{SG_{exp}}(s,d)$ are taken from look-up tables based on MC. For stereoscopic observations the mean of each participating telescope and consecutively the mean scaled shower goodness $\langle SG \rangle$ of all telescopes is derived. Analogously, the background goodness variable $\langle BG \rangle$ is constructed with the group of pixels outside the shower ellipse. γ-ray showers and hadronic showers show different behaviour in $\langle SG \rangle$ and $\langle BG \rangle$, which is why it's possible to discriminate them

with these variables. To address NSB, the NSB goodness variable is constructed as

$$G_{NSB} = \frac{\sum\limits_{\text{pixels } i} \left[\ln L(s_i|0) - \langle \ln L \rangle|_0 \right]}{\sqrt{2 \times \text{NdF}}}. \tag{3.12}$$

If a shower is due to noise, $G_{NSB} \to 0$, for γ-ray showers $G_{NSB} \gg 0$. This property allows for a separation of γ-ray induced showers and background. For sources with usual values of NSB or stereoscopic analyses, γ-hadron separation with shower goodness $\langle SG \rangle$ and background goodness $\langle BG \rangle$/ NSB goodness G_{NSB} works well [for the performance of monoscopic reconstruction under standard conditions, see 120], [for the performance of the stereoscopic reconstruction: 122, 107].

With the discriminating parameters $\langle SG \rangle$ and $\langle BG \rangle$ events can be classified as γ-ray-like or background events (or un-categorized events, that will not be used further).

- γ-candidates
- background events
- un-categorized.

The high level of NSB in η Carinae challenges the discrimination with the NSB goodness, because, by definition, the measured level of NSB enters into it. The consequence is a uniform acceptance of γ-ray-like events, at the price of an inhomogeneous acceptance of γ-ray-like background. This will become important for the generation of sky images later on, because it leads to negative excess in regions with high NSB. For this reason, a modified version of the NSB goodness was used for the monoscopic analysis, the uniform NSB goodness G_{UNSB}. It is uniform in its assumption of a pedestal width of 1 p.e., which corresponds to a rate of $\sim$100 MHz NSB. Its distribution follows a Gaussian function with expected signal $\mu = 0$. The NSB rejection cut is applied in the positive tail of the distribution, at $G_{UNSB} = 50$ and only values bigger than this are included (compare fig. 3.8 *left*). With this assumption, a more homogeneous acceptance of γ-ray-like background events is reached, but the γ-ray acceptance remains inhomogenous. In figures 3.10a and 3.10b γ/γ-ray-like background acceptances are depicted for the case of the uniform NSB goodness parameter applied. Below, in figures 3.10c and 3.10d acceptances for the alternative parameter NSB goodness are shown. In principle, a homogeneous distribution in both is desirable, but it's not possible to reach with this approach. A definition of acceptance and methods of acceptance calculation will be presented in section 3.5. It must be noted that the use of G_{UNSB} is not without risk as

it was shown to be able to produce positive excess at high NSB regions [134]. However, it turned out to be the best variable at-hand for a detection measurement at low energies because it reaches a lower energy threshold than comparable variables.[1] A possible correlation with high NSB regions will be investigated thoroughly in chapter 4.

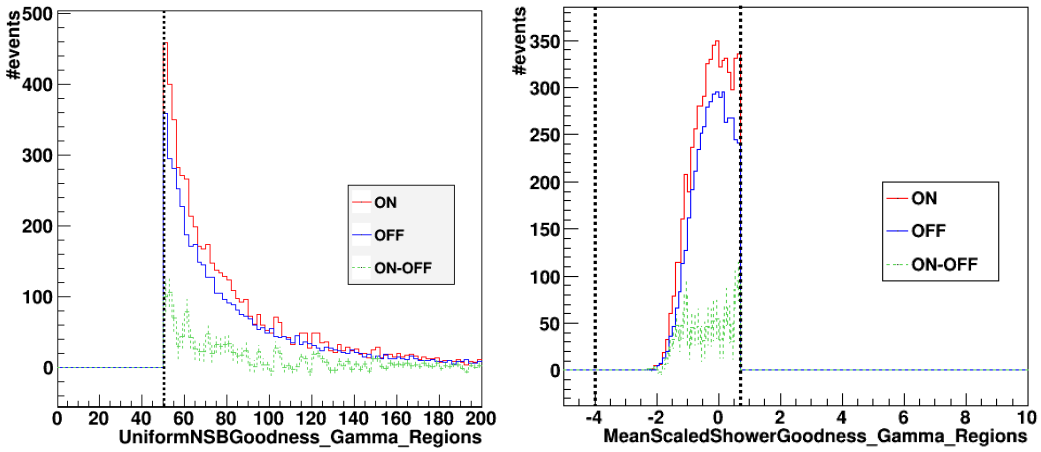

Figure 3.8: Discriminating parameters *uniform NSB goodness* G_{UNSB} and *mean scaled shower goodness* $\langle SG \rangle$ used for the monoscopic analysis of η Carinae with Paris Analysis. Dashed black lines in both plots depict the cut values. ON and OFF correspond to events in ON and OFF regions (see section 3.5). *Left:* NSB cut parameter of the monoscopic analysis G_{UNSB} (eqn. no 3.12, but with the modification of a fixed pedestal σ_p). Events induced by a NSB rate of $\sim 100\,\mathrm{MHz}$ accumulate around zero. Values of $G_{UNSB} > 50$ are used. *Right:* Main background cut parameter in the Model Analysis (mono and stereo) $\langle SG \rangle$ (definition in equation 3.11). Values of $-4 < SG < 0.7$ are used.

γ-hadron discrimination in stereoscopic analyses requires less effort in general, because the additional information helps to reduce the amount of background right at trigger level. The two main parameters for γ-hadron separation in stereo analyses with the Model Analysis are the aforementioned mean scaled shower goodness $\langle SG \rangle$ and the depth of the first interaction T. The mean scaled background goodness $\langle BG \rangle$ is also applied, but as a safety cut with little rejection power. Additional variables for the discrimination between γ-ray showers and hadronic showers are the depth of the first interaction T, a minimal size s and a minimum number of pixels above a given threshold.

After successful background reduction, only shower images classified as γ-like (events) are left. This sample includes γ-rays from the source, diffuse γ-rays from unresolved sources and cosmic-ray interactions in the interstellar medium, as well as hadronic and

[1] Development and performance evaluation of G_{NSB}, G_{UNSB} and the alternative NSB parameters NSB likelihood and uniform NSB likelihood performed by M. de Naurois, M. Holler and D. Zaborov

electromagnetic induced showers that survive γ/hadron separation [information about the diffuse galactic γ-ray emission observed with H.E.S.S. in 135].

3.5 Source detection and sky image generation

The sample of events surviving γ/hadron separation (γ-like events or γ-candidate events) still contains background events that appear γ-ray-like. For the detection of γ-ray sources, it is therefore necessary to quantify the amount of background in the sample and extract the γ-ray signal from the source. A simple method is based on the definition of an ON region around the source and OFF regions as control regions for background estimation. The number of events from the source N_{src} can be calculated by comparing event numbers from the ON and OFF regions: $N_{src} = N_{ON} - \alpha N_{OFF}$.

The factor α corrects for differences between the source region and control regions. αN_{OFF} is the corrected number of background events N_B. These differences are the observed solid angles, the zenith angles of the observations and the exposure times (time a region is inside the field of view). Another origin of differences is the different acceptance to γ-ray-like cosmic ray background events. The determination of acceptance is described later in this chapter. α has to be calculated for every region in every run. A general definition of α can be found in, e.g., [136]. For a number of runs n,

$$\alpha = \sum_i^n \frac{\alpha_i N_{OFF,i}}{N_{OFF,i}} \qquad N_{ON} = \sum_i^n N_{ON,i} \qquad N_{OFF} = \sum_i^n N_{OFF,i}. \tag{3.13}$$

The significance of a source can be calculated by [137]:

$$\sigma = \sqrt{-2 \ln \gamma} \tag{3.14}$$

with

$$\gamma = \left[\frac{\alpha}{1+\alpha} \left(\frac{N_{ON} + N_{OFF}}{N_{OFF}} \right) \right]^{N_{ON}} \cdot \left[\frac{1}{1+\alpha} \left(\frac{N_{ON} + N_{OFF}}{N_{OFF}} \right) \right]^{N_{OFF}}. \tag{3.15}$$

To obtain N_{OFF} and α, several background models exist. One challenge is to find appropriate OFF regions, if, like in the FoV of η Carinae, observing conditions vary greatly. In this work, the *Ring Background* technique was applied for sky map generation and the *Reflected Background* technique for background estimation in the spectral

estimation [136]. During observations, the H.E.S.S. telescopes are pointed slightly offset from the source position (often 0.7 °). With these *wobble-mode* observations it is possible to define OFF regions with the same radial offset to the camera centre as the source. Furthermore, no observation time is lost to background-only observations as it was standard at the beginning of γ-ray astronomy.

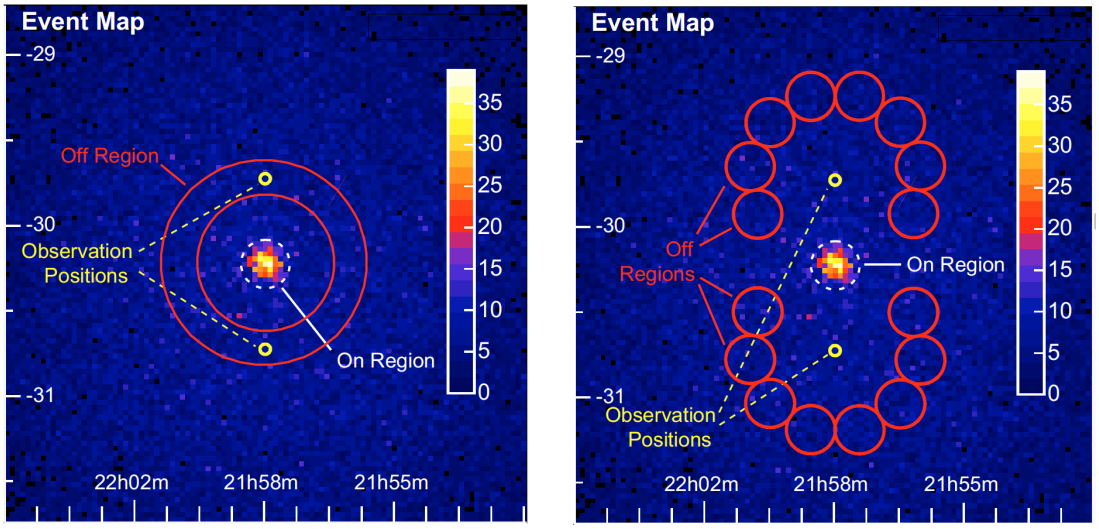

Figure 3.9: Count map of γ-ray like events illustrating the *Ring Background* method (*left*) and the *Reflected Background* method (*right*) for background estimation. Image taken from [136].

In the *Reflected Background* technique, a ring of n_{OFF} OFF regions is constructed for every observation position with the same offset to the camera centre, same size and shape as the source region (depicted in fig. 3.9, *right*). The same offset from the camera centre is important for the detector acceptance, because it depends on the radial distance to the camera centre. This leads to a simple way to determine α for an observation position in the *Reflected Background* method: $\alpha = 1/\mathrm{n_{OFF}}$. In contrast, the *Ring Background* technique utilises a ring around the observation position for background estimation (depicted in fig. 3.9, *left*). The ring-like OFF region includes positions with varying offsets from the observation position and therefore needs to address changes in the acceptance. This requires a detailed understanding of the detector acceptance for the calculation of α. For sky maps, α is approximated as the ratio of the solid angle of the ring Ω_{Ring} (typically 0.5 °) and the solid angles of the ON region and the OFF regions: $\alpha = \Omega_{Ring}/(\Omega_{ON}/\Omega_{OFF})$ (often $\alpha \sim 1/7$). However, the energy-dependence of the detector acceptance is not known in sufficient detail with the current methods which is the reason for limiting the use of the method to the generation of sky maps.

Both methods for background estimation are depicted in fig. 3.9.

In the following, the determination and definitions of the different acceptances will be outlined. In general, the acceptance depends on:

- The distance to the camera centre
- Zenith and azimuth angles of the observation
- The reconstructed primary energy
- The time of observation regarding the state of the system (e.g. mirrors aging)
- The night-sky-background.

The **acceptance for γ-rays** predicts the number of γ-rays in the FoV of the observations and is determined in energy bands with Monte Carlo simulations. Two methods for the determination of the γ-ray-like background acceptance used in H.E.S.S. are based on the summation of 2D maps or radial symmetry. The **γ-ray-like background acceptance** predicts the number γ-ray-like background events in the FoV of observations. Assuming radial symmetry, the acceptance can be provided by filling a 1D histogram with the squared angular distance between the reconstructed γ-ray direction and the pointing direction and rotating it (**radial accceptance** method). As can be seen in figure 3.10, this assumption does not hold fully for the observing conditions in η Carinae (strong and inhomogeneous NSB). The coordinate system used in figure 3.10 is the *Nominal System*. The coordinates express the distance to the camera centre, divided by the focal length of the telescope [a detailed description can be found in 131]. To derive the acceptance without the assumption of radial symmetry, a binned 2D map of γ-ray-like events and an exposure map is filled for every run and in the end summed over all runs (**2D acceptance** method). For the exposure map, the trajectories of the excluded regions are monitored and removed. This is done by first computing the distribution of background events in the Nominal System with excluded regions (regions of significant γ-ray emission), then without excluded regions. The ratio of these maps is the exposure map for this run. This assumes an approximately homogeneous background. Holes from exclusion regions in a single map are covered up in the summation, because every new observation position has its unique exclusion regions (in the *Nominal System*). The final acceptance map is obtained as the ratio between the γ-ray-like events map and the exposure map. This acceptance map is a measure for the expected amount of γ-ray -like backgrounds events. In Paris Analysis, there are two ways implemented to display

acceptances maps. The **FoV acceptance** maps show the acceptance in the Nominal System, which is centred on the actual camera centre (e.g. figure 3.10). The **Sky Acceptance** display is just the translation of the acceptance in the Nominal System to sky coordinates.

The choice of the NSB rejection parameter influences the shape of γ/background acceptance. As mentioned in section 3.4.2, one has to compromise between a flat acceptance in γ-rays or background, "flat" or "uniform" meaning "more radially symmetric" and less susceptible to inhomogeneities due to NSB. In the case of η Carinae, with both NSB cut parameters this is only partially reached and only for the background acceptance.

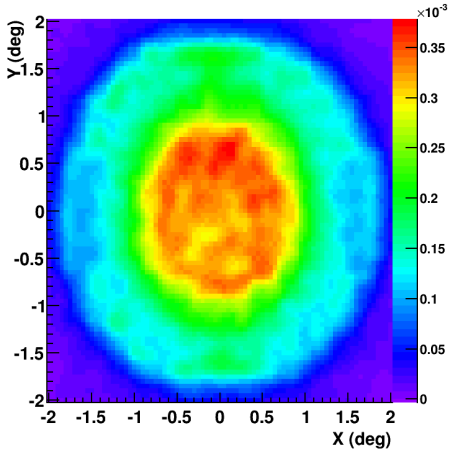

(a) γ acceptance with uniform NSB goodness

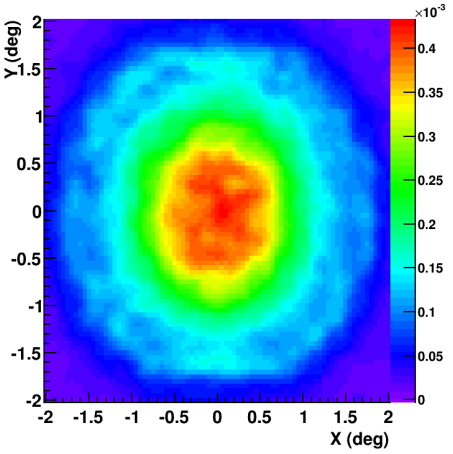

(b) Background acceptance with uniform NSB goodness

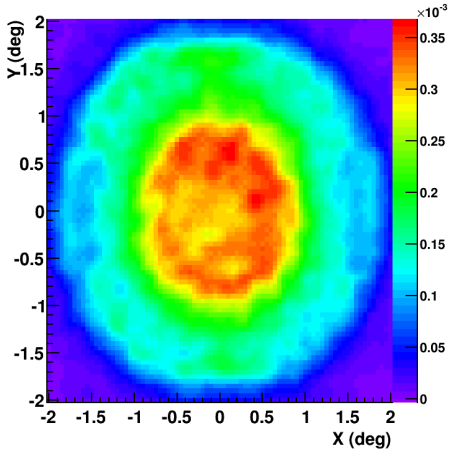

(c) γ acceptance with NSB goodness

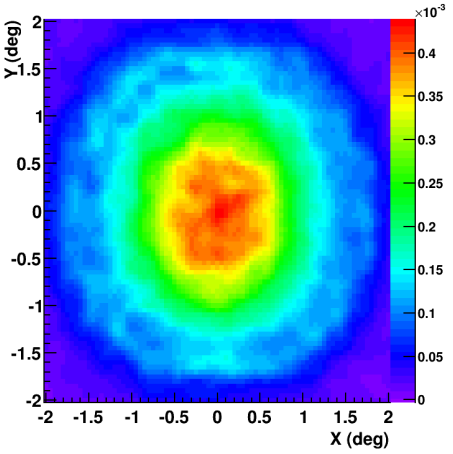

(d) Background acceptance with NSB goodness

Figure 3.10: 2D acceptance maps for γ-/background acceptance with uniform NSB goodness G_{UNSB} (*Top*) and standard NSB goodness G_{NSB} (*Bottom*). The coordinate system used here is the *Nominal System* [131]. The camera centre is at position (0,0) and the source position changes from run to run in this coordinate system.

3.6 Spectrum determination

Besides the detection of a γ-ray source, the energy spectrum of the source is of main interest. The spectral energy distribution allows to study the properties of the acceleration mechanism at work in the source, e.g. the highest energy reached by a γ-ray or

the shape of the spectrum. In the following, the technique for the production of energy spectra of γ-ray sources will be presented.

The reconstruction method of the energy spectrum applied in this work was originally developed for the CAT experiment and later adapted for the use in H.E.S.S. [138]. It is based on the bin-wise comparison of γ-ray event numbers with the predicted number of γ-ray events (bins in reconstructed energy).
The flux of a source is defined as the amount of emitted photons N per energy interval E, surface unit on the ground S, time interval t and the assumed shape of the spectrum represented by the spectral parameters α_i

$$\Phi(E) = \frac{\mathrm{d}^3 N}{\mathrm{d}E\,\mathrm{d}S\,\mathrm{d}t}(E, \alpha_i). \tag{3.16}$$

Since the flux of the source $\Phi(E)$ is a function of the true energy and only the reconstructed energy $\tilde{E}$ is known, the effective photon detection area $\mathcal{A}_{\mathrm{eff}}$ and energy resolution $\mathcal{R}$ need to be taken into account, also to calculate the expected number of γ-rays n_γ

$$n_\gamma = \int_{\tilde{E}_1}^{\tilde{E}_2} \mathrm{d}\tilde{E} \int_0^\infty \mathrm{d}E \;\mathcal{R}(\tilde{E}, E, \theta, \phi) \;\times\; \mathcal{A}_{eff}(E,\theta,\phi) \;\times\; \Phi(E). \tag{3.17}$$

How they are determined will be discussed in the next section.

The **effective** (detection) **area** is a measure for the efficiency of a detector and depends on the true energy E, the zenith angle θ and the off-axis angle ϕ. It is generally defined as the integral of the detection probability over the surface area on ground and is calculated with simulations. Photons are simulated for a range of zenith and azimuth angles [for a detailed description of the simulation of effective areas, see 120]. The calculation of $\mathcal{A}_{eff}$ is implemented via the multiplication of a response matrix $\mathbf{R}_{ji}$ with the simulated detection area with radius r_{sim}

$$\mathcal{A}_{\mathrm{eff},j} = \sum_i \mathbf{R}_{ji,k} \;\times\; r_{\mathrm{sim}}^2 \pi. \tag{3.18}$$

The response matrix $\mathbf{R}_{ji,k}$ is composed of the energy migration matrix $\mathbf{M}_{ji,k}$ and the

detection efficiency and differs for photons, protons and electrons ($k = \gamma, p, e$):

$$\mathbf{R}_{ji,k} = \frac{\mathbf{M}_{ji,k}}{N_{\mathrm{sim},j}}. \tag{3.19}$$

Figure 3.11a shows an extract of $\mathbf{R}_{ji,\gamma}$ for a zenith angle $\theta = 18\,^\circ$ and the *Loose* cut configuration inside the monoscopic Model Analysis in H.E.S.S. [more details about the calculation of the effective areas in 120]. The energy migration matrix $\mathbf{M}_{ji}$ translates a reconstructed energy $\tilde{E}$ into the true energy E. $N_{\mathrm{sim},j}$ is the j-th element of the vector of simulated true energies $\vec{N}^{\mathrm{T}}_{\mathrm{sim}}$. Figure 3.11b shows the effective area of the monoscopic Paris Analysis in comparison to the effective area of the stereoscopic Paris Analysis with only CT1-4.

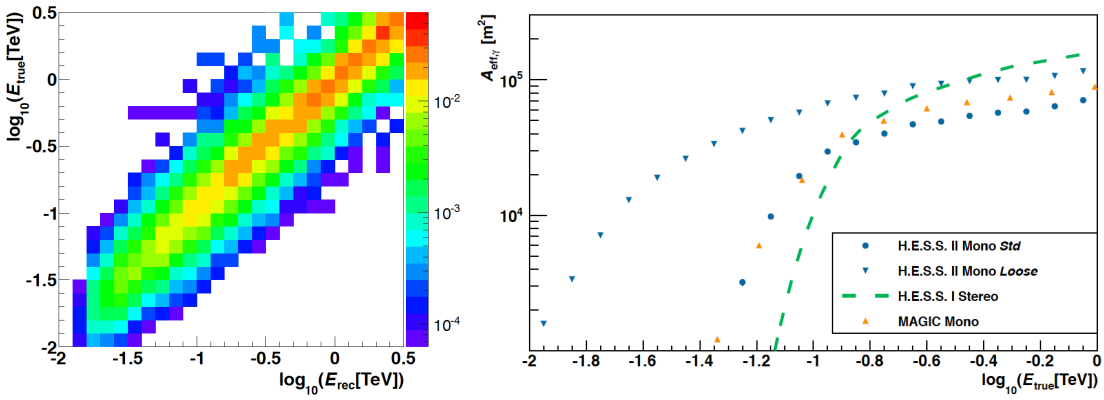

(a) (b)

Figure 3.11: Extract of $\mathbf{R}_{ji,\gamma}$ for a zenith angle $\theta = 18\,^\circ$ and the *Loose* cut configuration inside the monoscopic Model Analysis (a). Effective photon detection area for monoscopic Paris Analysis Std and Loose cut configurations, CT1-4 stereo analysis and monoscopic MAGIC analysis for small zenith angles (b). Images taken from [120]. MAGIC Mono results taken from [139], H.E.S.S. I Stereo results taken from [107].

The **energy resolution** $\mathcal{R}(\tilde{E}|E,\theta,\phi)$ is the probability of measuring a certain reconstructed energy $\tilde{E}$ for a given true energy E. For the estimation again simulations of γ-rays are used and reconstructed with the Model Analysis framework. After γ/hadron separation, the distribution of the ratio of reconstructed and true energy $\ln(\tilde{E}/E)$ is filled in histograms and fitted with a Gaussian function $f(\ln(\tilde{E}/E)) = A \cdot \exp\left(\frac{(\ln(\tilde{E}/E)-b)^2}{2{\sigma_E}^2}\right)$. This step is repeated for a range of true energies, zenith angles and analysis configurations (monoscopic or stereoscopic, standard cuts or loose cuts etc.). The parameter b gives an estimation of the energy reconstruction bias as a function of the true energy. The energy range where H.E.S.S. analyses are performed

is inside the range where b is below 10 %. σ_E gives the 68 % energy resolution for a certain zenith angle and analysis configuration as a function of the true energy.

Effective area and energy resolution are tabulated as functions of the true energy, zenith angle, off-axis angle and also optical efficiencies (also called *instrument response functions*, IRFs). With the effective area and energy resolution tabulated, the next step on the way towards a spectral energy distribution is the calculation of the expected number of γ-ray events n_γ (eqn. 3.17).

The expected number of γ-ray events n_γ depends on the spectral shape. In this work, a simple power-law function is assumed:

$$\frac{\mathrm{d}N}{\mathrm{d}E} = \Phi_0 \left(\frac{E}{E_0} \right)^{-\Gamma}. \tag{3.20}$$

Parameters α_i of the power-law function are the spectral index Γ, the reference energy E_0, where the differential flux is calculated, and the normalisation Φ_0. The probability of observing N_{ON} and N_{OFF} events when n_γ is the number of expected γ-ray events and n_{Bck} the expected number of background events is given by

$$P(N_{ON},N_{OFF}|n_\gamma,n_{Bck}) = \frac{n_\gamma + \beta n_{Bck}^{N_{ON}}}{N_{ON}!} \mathrm{e}^{-(n_\gamma+\beta n_{Bck})} \times \frac{n_{Bck}^{N_{OFF}}}{N_{OFF}!} \mathrm{e}^{-n_{Bck}}. \tag{3.21}$$

The expected number of background events n_{Bck} is found as the best fit parameter when maximizing the log-likelihood $\ln L = \ln P(N_{ON},N_{OFF}|n_\gamma,n_{Bck})$. In 3.21, the parameter β is the ratio between the amounts of observation time that went into measuring N_{ON} and N_{OFF}: $\beta = T_{ON}/T_{OFF}$. With the solution for n_{Bck}, $\ln L$ is maximized to fit the spectral parameters Γ, Φ_0 and E_0. For the estimation of N_{ON} and N_{OFF}, the *Reflected Background* technique for background estimation was applied. The translation of the spectral energy distribution from reconstructed to true energy is performed in every reconstructed energy bin $[\tilde{E}_1,\tilde{E}_2]$ by first calculating the average true energy $\langle E \rangle$:

$$\langle E \rangle = \frac{\int_{\tilde{E}_1}^{\tilde{E}_2} E \, \mathrm{d}\tilde{E} \int_0^\infty \mathrm{d}E \;\; \mathcal{R}(\tilde{E},E,\theta,\phi) \times \mathcal{A}_{eff}(E,\theta,\phi) \times \Phi(E)}{\int_{\tilde{E}_1}^{\tilde{E}_2} \mathrm{d}\tilde{E} \int_0^\infty \mathrm{d}E \;\; \mathcal{R}(\tilde{E},E,\theta,\phi) \times \mathcal{A}_{eff}(E,\theta,\phi) \times \Phi(E)}. \tag{3.22}$$

The average true energy per reconstructed energy bin i states the position of the spectrcal point $(E_i, \tilde{\Phi}(E_i))$ with uncertainty $\sigma_{Energy} = \sqrt{\langle E^2 \rangle - \langle E \rangle^2}$. Also the flux $\Phi(\langle E \rangle)$ needs to be transformed to true energy. This is simply done by scaling $\Phi(\langle E \rangle)$ with the

ratio of observed γ-ray events N and expected γ-ray events:

$$\tilde{\Phi}(\langle E \rangle) = \frac{N}{n_\gamma} \times \Phi(\langle E \rangle). \tag{3.23}$$

This approach to the determination of a spectral energy distribution is also described in [138, 122].

In the following chapter, the methods introduced in this chapter will be applied to the H.E.S.S. data set of η Carinae.

Chapter 4

H.E.S.S. observations of η Carinae

The detection of η Carinae in 2009 by the γ-ray satellite *AGILE* was the first time that γ-ray emission was seen from a CWB [86]. $Fermi-$LAT data confirmed the detection and the source showed high-energy γ-ray emission up to GeV energies [88, 33]. Although the following H.E.S.S. observations yielded upper limits, the interest in the object continued. The threshold energy in the analysis published in 2012 was $E_{Th} = 470\,\mathrm{GeV}$. The non-detection implied a cut-off below $\sim 1\,\mathrm{TeV}$ under the assumption of an extrapolation of the hard HE γ-ray component measured by $Fermi-$LAT . Given the limited statistics, the spectral shape of the HE γ-ray component was described as a pure power-law with a spectral index of 1.85 ± 0.25 [94]. The addition of the bigger telescope to the H.E.S.S. array the same year nourished expectations for the upcoming periastron passage in 2014, because the energy threshold was expected to be reduced significantly and the maximum of emission was expected to occur around this orbital phase. With its interesting nature as CWB and supernova-impostor, η Carinae is an extraordinary source for H.E.S.S. Unfortunately, this is also true in terms of background. Since the impact of NSB from the Carina nebula on the more complex Model Analysis is expected to be more complex, the analysis of η Carinae data commenced with a Hillas analysis and NSB studies.

In the following, H.E.S.S. observations of η Carinae and the properties of the data set will be covered. Subsequently, the steps towards the analysis in Hillas, the analysis and its results will be described. After the completion of all studies within the Hillas reconstruction, the focus will lie on results and tests accomplished with the Model Analysis. Finally, an interpretation of the achieved results concerning the processes of particle acceleration and γ-ray production in η Carinae will be given.

Table 4.1: Properties of the data sets used in this work. The time range of the H.E.S.S. observations, the total live time corresponding to the individual data sets along with the covered orbital phase are summarised.

Data Set	MJD	Phase	live time mono/stereo [!htbp]
I	56439-56444	0.78	0.90/0.65
	56666-56667	0.89	0.79/0.79
	56741-56751	0.93	9.38/7.99
	56775-56778	0.95	0.88/0.80
	56797-56799	0.96	1.81/1.65
II	56803-56807	0.96	3.34 /-
	57066-57074	1.09	8.62/-
	57077-57079	1.10	3.95/-
all	56439-57079	0.78 - 1.10	29.67/ 11.88

4.1 Properties of the data set

The main challenge in the analysis of γ-ray data from the direction of η Carinae is the large number of UV photons, which are the origin of the high NSB. The UV photons originate from the massive star-forming region Carina nebula (compare sec. 2.3). To distinguish real Cherenkov showers from NSB-induced events, at least three neighbouring pixels with > 4.0 p.e. are required to trigger the CT5 camera in standard operation mode. Thereby, the number of NSB induced triggers is reduced to a level of 1.5 kHz. In the case of η Carinae this threshold was adopted for data set I, whereas for data set II, the pixel trigger threshold had to be increased to 4.5 p.e. The data used in the following analysis was taken in the first 6 months of 2014 and 2015 (with the exception of two runs which were taken in summer 2013). In table 4.1 H.E.S.S. observation times, data sets DS-I and DS-II, covered phases, exposure of the data sets, and observation modes (mono vs. stereo) are summarized. Observations were carried out in mono mode only (exclusively CT5) for DS-II. Therefore, the emphasis of this work is put on the mono analysis, while also presenting the results of the stereo analysis. In total, about 30 h of observations pointing towards η Carinae are available in single-telescope mode and only about 12 h with the full telescope array or a combination of CT5 plus at least one of CT1-4. Cameras were pointed offset from the source coordinates at $\pm 0.5/0.7$ in RA, or Dec. Zenith angles below 45 ° were asked for to reach low in energy and increase the overlap with $Fermi-$LAT . The mean zenith angle is $\langle\phi\rangle = 38.3\,°$.

The data quality of DS-I and DS-II has been checked with standard tools. To adjust to the high NSB level and the extra pixels turned off to protect the Cherenkov

Table 4.2: Data quality cuts.

Cut	Value
Mean trigger rate	1200 - 3000 Hz
Trigger rate dispersion	$< 10\,\%$
CT5 dead time	$< 5\,\%$
Run duration	5 min
Autofocus position	60 - 80 mm
Broken pixel	$< 10\,\%$

camera, the requirement on the maximum number of turned-off pixels per observation run in CT5 has been relaxed from 5% to 10%. All data quality requirements are summarized in table 4.2. The data was calibrated using the French calibration chain [122]. All analysis results presented in this thesis were cross-checked successfully with an independent analysis chain in H.E.S.S. [details about this analysis chain can be found in 132, 140, 141].

4.2 Hillas analysis of η Carinae

In this section, the Hillas analysis results and the tests that prepared the analysis of the data with the Model Analysis are presented.

4.2.1 Analysis configurations

The main challenge is to control the background rate while at the same time not lose sensitivity. To reduce the amount of noise, the cleaning levels, as mentioned in 3.4.1, are adapted to new pixel thresholds of (6, 12) p.e. This level is chosen to keep approximately the same cut efficiency in η Carinae analysis as in a standard Crab Nebula analysis. The Crab nebula is a well understood, standard source for H.E.S.S.and a comparable cut efficiency is desirable. One run of DS-I and DS-II, respectively, and two Crab Nebula runs - taken in the same time range as the η Carinae runs to ensure comparable camera conditions - were probed to find a suitable cleaning level. A CoG is computed for every shower. A homogeneous CoG distribution ensures that showers of a certain direction do not contribute unproportionally. In figure 4.1 CoG maps for the different cleaning levels and size cuts are compared for one of the Crab runs. The colour scale shows how often a CoG falls into a certain pixel. Spots of red colour represent regions inside the camera where many showers were recorded. The chosen set of cuts corresponds to the

most homogeneous map, figure 4.1(e), which also has an overall reduced event number. A (6, 12) p.e. level leaves 70 % of all events with respect to the lowest cleaning level (4, 7) p.e. The standard cuts (table 4.3) include a minimum requirement on the size, which is $s = 60$ p.e.

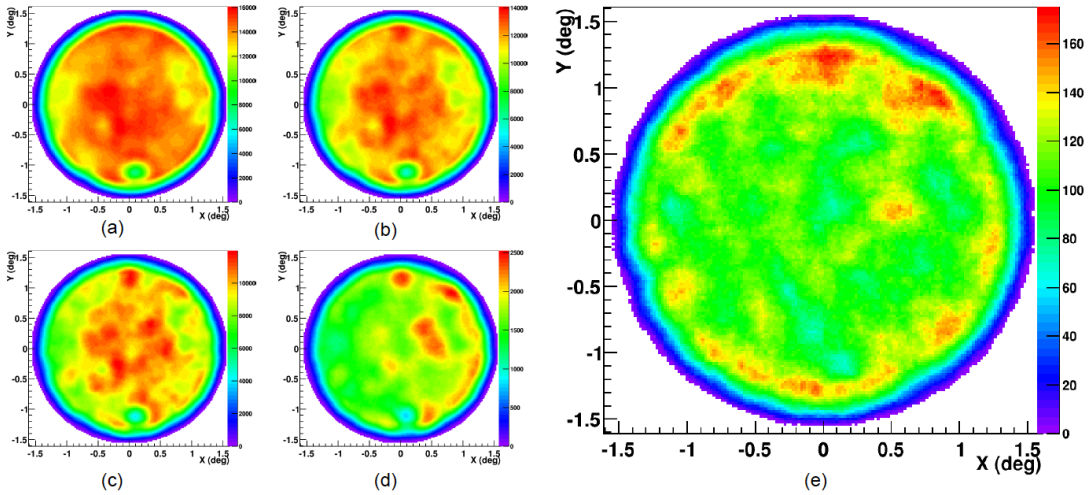

Figure 4.1: Centre of gravity distributions for different cleaning levels and size cuts on a representative Crab run. The colour scale indicates the frequentness of CoGs at a certain position in arbitrary units (because of smoothing). The maps are smoothed by integrating the pixel radius of 0.16 deg. Images *(a), (b), (c)* depict an increase in cleaning levels from (4,7), (5,10) to (6,12). Images *(c), (d)* and *(e)* have a (6,12) p.e. cleaning and an increased size cut from 40 p.e. to 120 p.e. and 400 p.e. Configurations (cleaning level, size cut): *(a)* (4,7) p.e., 40 p.e. *(b)* (5,10) p.e., 40 p.e. *(c)* (6,12) p.e., 40 p.e. *(d)* (6,12) p.e., 120 p.e. *(e)* (6,12) p.e., 400 p.e.

To suppress the NSB, a change in event counts of less than 1.5 % when applying an additional cut on 3 times the pedestal width was aimed for when raising the pixel thresholds of the cleaning levels. This was reached by a reduction of events by 20 %. For a Crab Nebula run, this is the case with a (4, 7) p.e. cleaning and a size cut of $s = 40$ p.e. The probed η Carinae run showed the same decline in event numbers with a (6,12) p.e. cleaning and a cut on $s = 400$ p.e.

A circle with the radius of 0.44 ° around η Carinae is excluded for the definition of the OFF regions. This is necessary to detain leakage of signal into the background regions and to avoid negative significances stemming from turned-off pixels that could fake a signal. Background estimation is performed with the *ring background* technique. With a cut on the ϑ^2 variable (ϑ is the angular distance between reconstructed and

	MSW	MSL	Min Charge CT5 [p.e.]	Nominal Distance [deg]	ϑ^2[deg^2]
Std Hillas Mono	[−4,0.9]	[−2,2]	60	[0,2]	[0,0.015]
This analysis	[−4,0.9]	[−2,2]	400	[0,1.4]	[0,0.04]

Table 4.3: Standard cuts in the Hillas mono analysis and cuts used in this analysis.

true source direction), the size of the ON region is estimated. The standard cut value for a source that is compatible with being point-like for H.E.S.S. is $0.015\,\mathrm{deg}^2$. The compatibility with being point-like depends on the point spread function of H.E.S.S. (defined in chapter 3.2). In this analysis, a wider range for $\vartheta^2 = 0.04\,\mathrm{deg}^2$ is chosen, because the NSB is potentially able to produce a smear in the signal from η Carinae. The broadening is further investigated with tailored simulations later on.

4.2.2 Low-level checks

After the definition of suitable cuts for the analysis, it remains to be checked whether the analysis delivers reasonable results on a low analysis level, on which the main results (spectrum, light curve or ϑ^2 plots, e.g.) will be build. For all runs in DS-I and DS-II intensity and CoG maps were checked for features. The reconstruction of shower properties is based on measured intensities. Therefore intensity maps are a valuable diagnostic tool to spot irregularities early on (before reconstruction). In all η Carinae intensity maps groups of turned-off pixels are visible. Pixels are shut down for security reasons if the current drawn by the PMTs exceeds $150\,\mu$A in CT5 [114]. This is easily reached by the NSB of the Carina nebula. In figure 4.2 intensity maps (average intensity, RMS intensity) and the RMS distribution of p.e. per pixel are shown for two representative runs of the Crab nebula (*top* panel) and η Carinae (*bottom* panel). The strong NSB level in η Carinae is reflected in the large number of turned-off pixels, which is about twice as high in run 95305 compared to the Crab run no 82782. The mean RMS intensity in p.e. per pixel is $\langle\sigma_{I,Eta}\rangle = (3.0 \pm 0.4)$ p.e. for the η Carinae run in comparison to $\langle\sigma_{I,Crab}\rangle = (2.3 \pm 0.3)$ p.e. for the Crab run (compare figures 4.2b and 4.2d). This higher mean RMS intensity reflects the influence of NSB photons. The shape of the region with enhanced sensitivities in fig. 4.2c resembles the shape of the highest NSB region in the Carina nebula measured with H.E.S.S. (covered in section 4.2.3).

After Hillas reconstruction the distribution of CoGs, γ- and background candidate events are checked for every run. Figure 4.3 depicts exemplary the distributions of γ-ray candidates and background events. The runs of the analysed data sets I and II show no

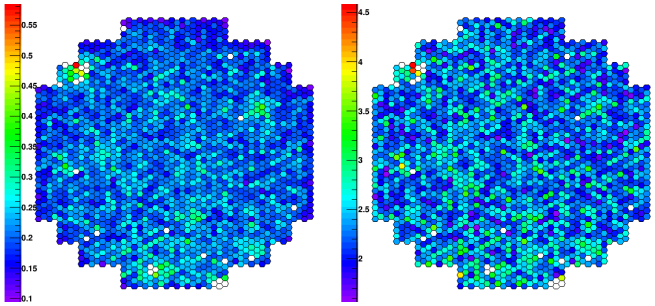

(a) Crab Nebula run no 82782 (2013-04-02)

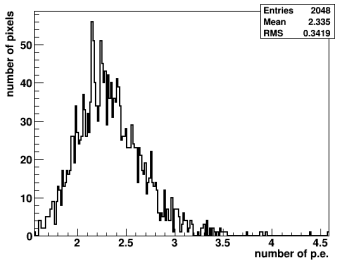

(b) RMS distribution of p.e. per pixel.

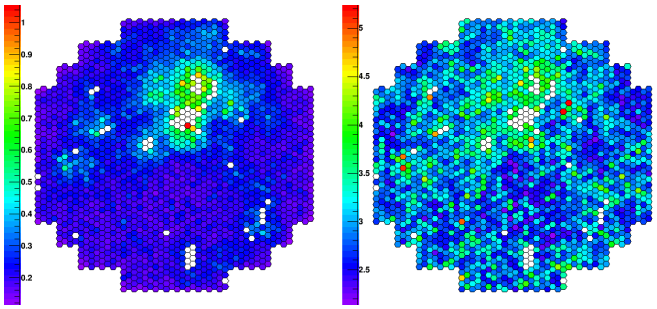

(c) η Carinae run no 95305 (2014-05-30)

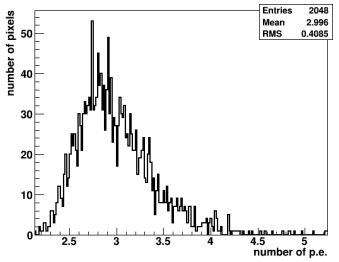

(d) RMS distribution of p.e. per pixel.

Figure 4.2: Pixel-wise average intensity (*left*) and RMS intensity (*middle*) maps for two representative Crab (*top*) and η Carinae (*bottom*) runs in the high-gain channel in the CT5 camera. Every hexagon depicts a pixel. The RMS values (*middle*) are projected in the last plot (*right*). The colour scale is in p.e.

suspicious features. In figure 4.3 the projected and normalized acceptance along the x- and y-axis of the camera plane is shown for all runs of DS-I. A deviation of $\pm 10\,\%$ in the number of events is considered stable in the standard Paris Analysis case. To meet this requirement, the allowed distance between the reconstructed direction of a γ-ray event and the pointing position of the telescope was restricted to $1.5\,^{\circ}$.

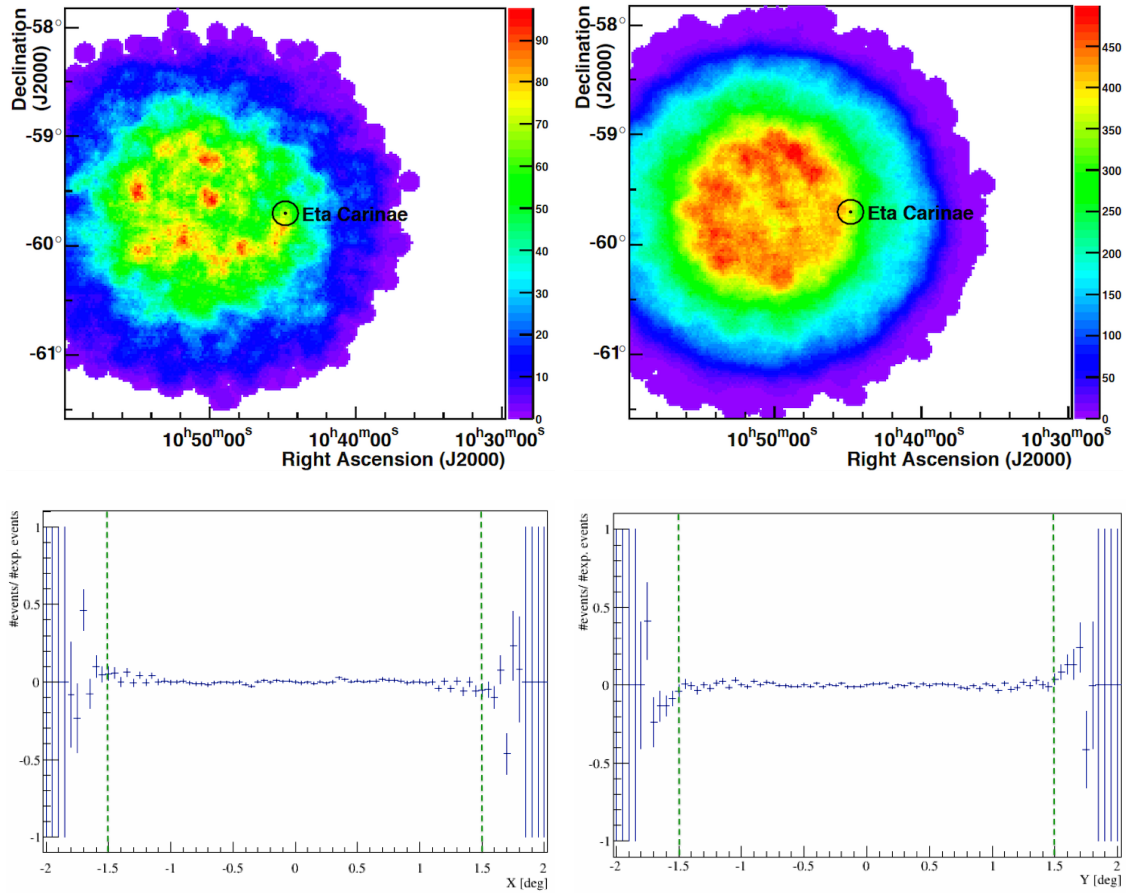

Figure 4.3: *Top*: Representative γ-ray candidate map for run number 104000 (*left*). Representative background map for run number 104000 (*right*). *Bottom*: Number of γ-ray events (acceptance normalized) as a function of distance from the camera centre in X (*left*) and Y-direction (*right*) in the camera in the *Nominal System*.

4.2.3 Results

Data sets DS-I and DS-II were analysed with a modified standard configuration in monoscopic mode *Hillas Mono Std*. Hillas reconstruction is not expected to be sensitive enough to perform a stereoscopic analysis that yields a reasonably low threshold. Table 4.3 summarises the cuts and differences to the standard analysis configuration. The target region was centered on the optical position of η Carinae at RA $10^{\mathrm{h}}\,45^{\mathrm{m}}\,03.6^{\mathrm{s}}$ and Dec $-59^{\circ}\,41'\,04.3''$ (J2000).

Analysing DS-I and DS-II together and applying the *Ring Background* method for signal extraction, an excess with a significance of $S = 8.2\,\sigma$ is obtained with a Hillas

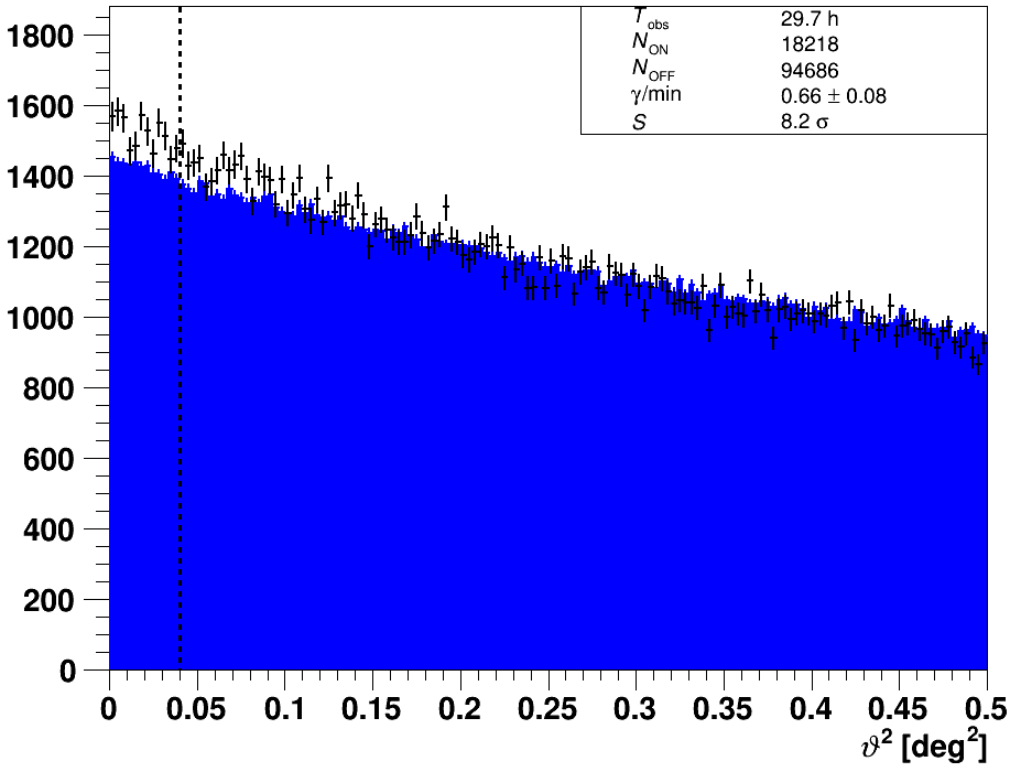

Figure 4.4: Distribution of the number of ON events (black) and $\alpha \cdot N_{OFF}$ (blue) as a function of ϑ^2 for the combined analysis of DS-I and DS-II with Hillas Std Mono. The dashed black line indicates the cut value of $\vartheta^2_{\max}$.

Mono Std analysis (shown in figure 4.4, $5.3\,\sigma$ DS-I only, $3\,\sigma$ DS-II only). After correcting the observation time of 29.7 h by the camera acceptance, the effective livetime amounts to 21.5 h. Figure 4.4 depicts the distribution of ON and OFF events as a function of squared angular distance from the source position ϑ^2. The source position is at $\vartheta^2 = 0$. Examining the PSF with the radius that contains 68% of excess events yields $R_{68} = 0.42\,^\circ$. Run-wise Monte Carlo simulations were provided for DS-I to check the broadening of the PSF [142]. Run-wise simulations take into account the observing conditions in a more detailed way than the classical simulations used in H.E.S.S.. Instead of simulating a fixed number of zenith angles and observation offsets and then interpolating to match a given observation, the exact zenith angle, observation offset, pointing accuracy and optical efficiency is used to produce a tailored simulation for each run. The NSB level (that is fixed to 100 MHz in classical simulations) is extracted

from the pedestal measurement (compare section 3.3) and included into the run-wise simulation. Also the deactivation of pixels in case of too high currents due to NSB is correctly implemented.

300 000 γ-rays from a point source with a power-law spectrum with index $\Gamma = 3.0$ were simulated (energy range: 50 GeV - 10 TeV, maximum impact distance 400 m). To check the influence of NSB and turned-off pixels on the PSF, different versions were produced with either the actual NSB level or the default value of 100 MHz and either the real number and pattern of turned-off pixels or a default value. The resulting ϑ^2 histogram for DS-I is shown in figure 4.5 (*left*) and a zoom into the range below $\vartheta^2_{max} = 0.05$ (*right*). Four representative runs of DS-I were simulated and the live

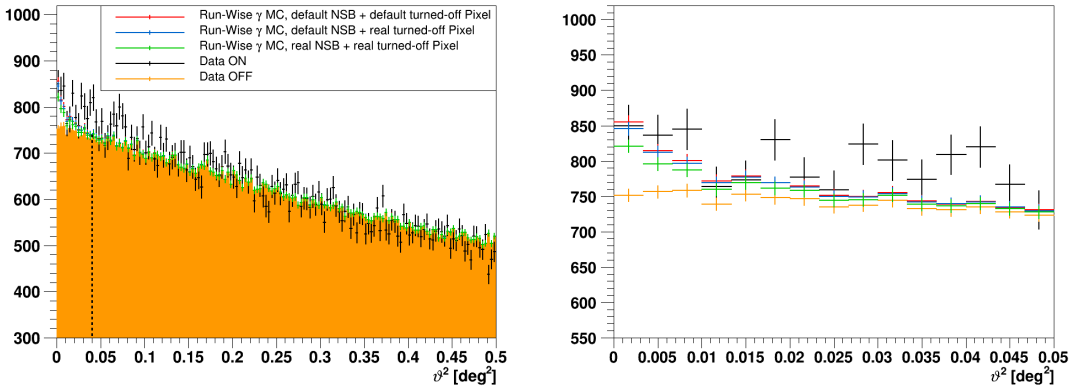

Figure 4.5: *Left*: Distribution of the number of ON events (black) and $\alpha \cdot N_{OFF}$ (orange) as a function of ϑ^2 for the analysis of DS-I with Hillas Std Mono in comparison to run-wise simulations with a power-law index of $\Gamma = 3.0$ (zero suppressed). The dashed black line indicates the cut value of $\vartheta^2_{\mathrm{max}}$. *Right*: Zoom into the ϑ^2 range $[0, 0.05]\,\mathrm{deg}^2$ of the left figure.

time was then scaled to match the total observation time. The PSFs from all simulations are compatible with the standard PSF in Paris Analysis monoscopic analyses of $R_{68} \sim 0.15\,^\circ$ for 68 % containment of events [119] and hereby fail to describe the broadening of the PSF observed. Differences between the simulations taking into account the measured NSB level or the right pattern and number of turned-off pixel have an effect on R_{68} of $\sim 0.01\,^\circ$ at most. The difference between simulations reflecting the real NSB and pixel conditions (green) and simulations with the standard values (red) is biggest at the source position but even then below 10 % in absolute event numbers. The influence of the broken pixels alone over the whole range of ϑ^2 is $\sim$8 %. The main influence of the NSB visible in the ϑ^2 histogram is a decline in γ-ray events which can be attributed

to the cleaning procedure in the beginning of data processing (compare section 3.4.1). The cleaning includes a cut on three times the pedestal width in a given pixel, thereby rejecting pixels containing a potential signal due to a higher NSB contribution. Discrepancies between simulations and data are strongest for $\vartheta^2 < 0.15\,\mathrm{deg}^2$ where 30 % of the ON events are incompatible within statistical errors with the simulated expectations. This enhancement is also visible in figure 4.7 as an extension of the source and will be further discussed with the results of the Model analysis. Over the whole range of ϑ^2 the simulation of the correct NSB level and turned-off pixels lowers the excess about 37 %.

One important difference between data and simulations here is the missing hadronic background in simulations. In combination with the high NSB one effect is that background events can pass the trigger criteria easier if NSB events add on top (compare section 3.3). As this analysis is performed in monoscopic mode no coincidence criterium is applied that could prevent this effect. One set of simulations with limited proton statistics was tested. Roughly one million protons were simulated together with 300 000 γ-rays in the same energy range (50 GeV - 10 TeV) and the same maximum impact distance (400 m). Comparing the integral of the ON event dristribution for $\vartheta^2 > 0.15\,\mathrm{deg}^2$ with the integral of $\vartheta^2_{sim,p} > 0.15\,\mathrm{deg}^2$ in the simulations including protons yields a difference of a factor ~ 20. Subsequently, the background from OFF events was not simulated sufficiently and the simulation is not shown in figure 4.5. In figure 4.5, the observed OFF events were added to the simulated ON events for visualization purposes. Unfortunately, increasing the proton statistic is not feasible because their simulation is computationally expensive. A further difference is the assumed power law spectral index that enters the simulation. This will be discussed in detail in the chapter covering the Model analysis results.

Regarding the sky map in figure 4.7, several issues are apparent. The γ-ray emission appears to be shifted from the source position and extended. In a radius of $\sim 0.06\,^\circ$ around the source position, emission is enhanced and this structure extends north and south of η Carinae where also the NSB level is enhanced (black contours in figure 4.7). The minimum NSB in η Carinae's direct neighbourhood is at least 300 MHz - 3 times the standard galactic NSB.

West of the binary system a negative excess reaching $\sim -5\,\sigma$ is situated. Figure 4.6 shows a sky map of the measured NSB with H.E.S.S. significance contours from 3.5, 4.75 to 6 σ. η Carinae is positioned right next to an elongated structure of high NSB

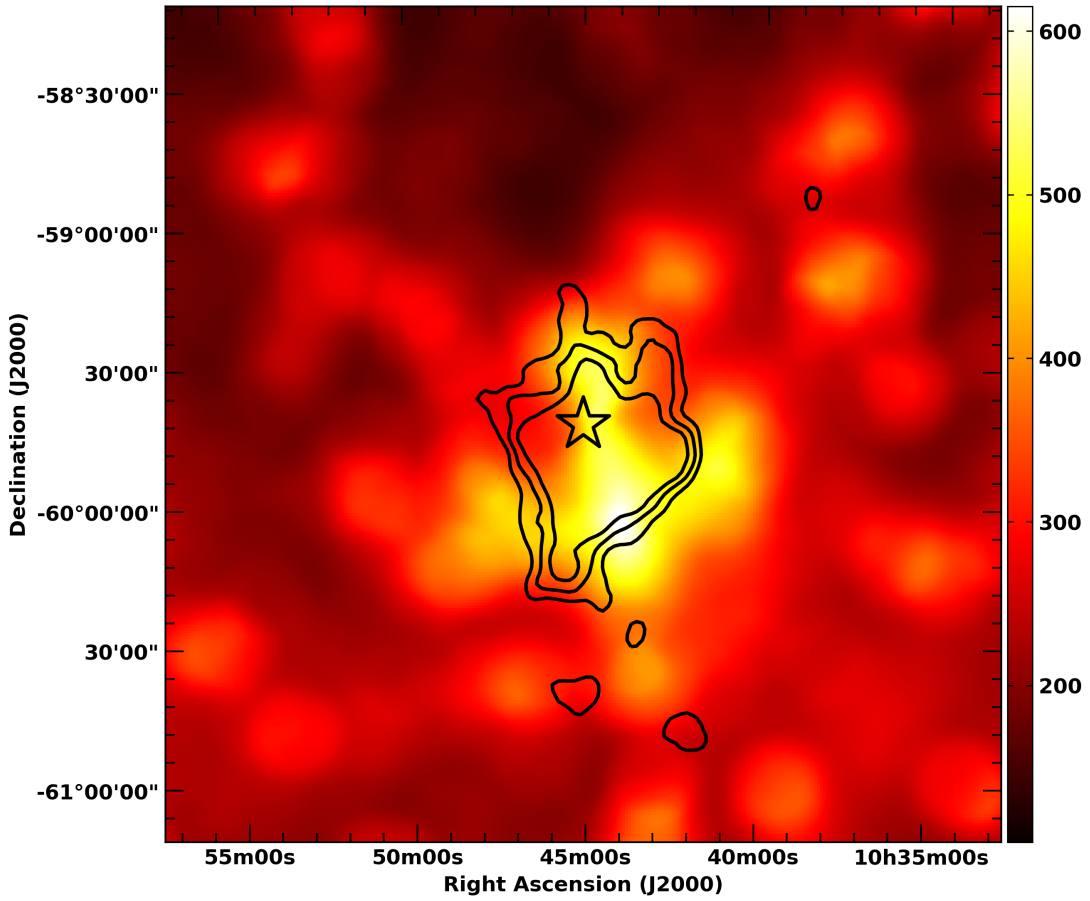

Figure 4.6: Sky map showing the NSB in MHz with overlaid H.E.S.S. significance contours for 3.5, 4.75 and 6 σ. The black star denotes the position of η Carinae.

originating in the UV emission of the Carina nebula. The significance contours partially cover this high NSB region, but do not include the point of maximum NSB.

Figure 4.8 shows the distributions of the cut parameters mean scaled width MSW and mean scaled length MSL and for energy E for data of DS-I and run-wise simulations including the real NSB and broken pixels. All distributions appear broadened compared to simulation and MSW and MSL also appear shifted towards positive values.

In terms of sensitivity a pure Hillas analysis is not able to compete with its descen-

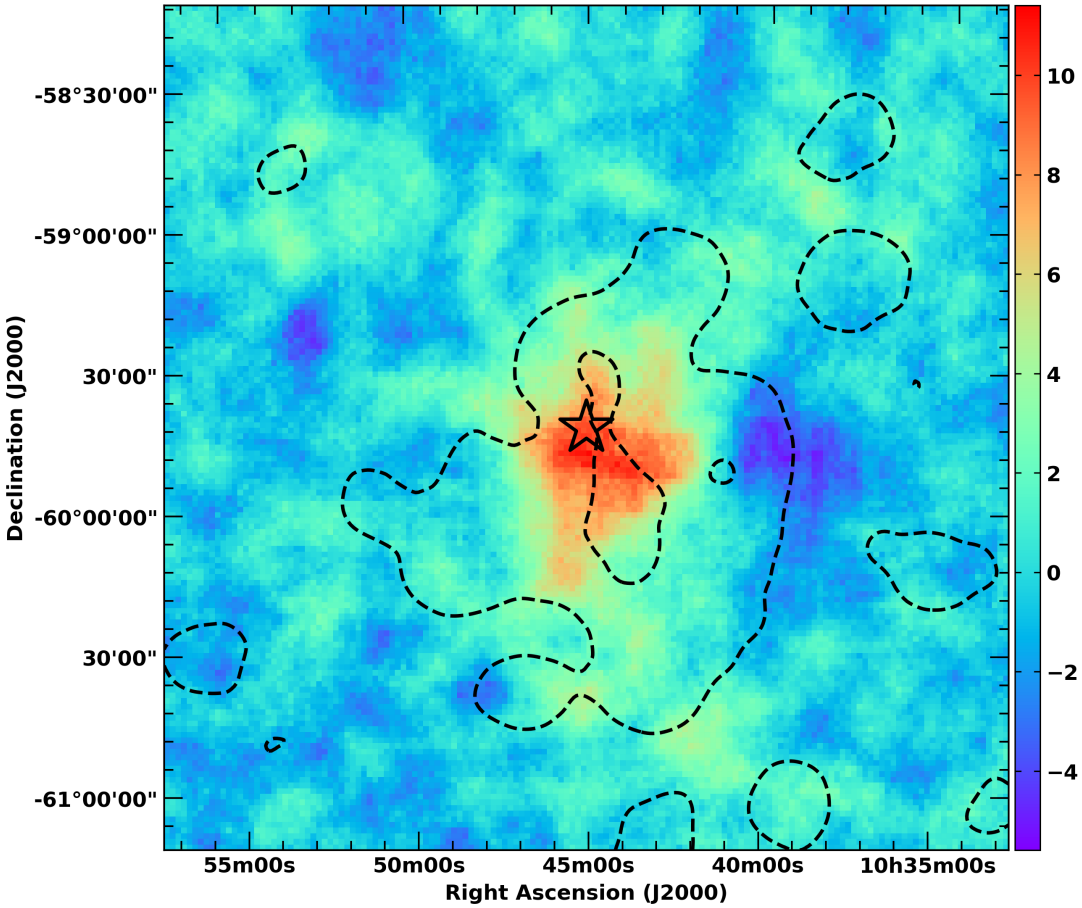

Figure 4.7: Sky map showing the H.E.S.S. significance of the Hillas Std Mono results for both data sets. The black star denotes the position of η Carinae. Contours in black depict NSB levels of 300 and 500 MHz.

dants - the more sophisticated analysis chains using a likelihood fitting approach, like the Model Analysis, which has been covered in chapter or machine learning techniques, like the analysis used for the cross-check from the *H.E.S.S. analysis package* - short *HAP* [140, 132, 141]. The impact of the NSB is visible throughout the analysis at various levels in inhomogeneous intensity and *CoG* distributions, shifted and broadened cut parameter distributions and an extended source size, despite the effort that was made to exclude NSB as early as possible. Still, for a following Model analysis the found configuration can be of advantage as the seeding of the Model fit is set with Hillas

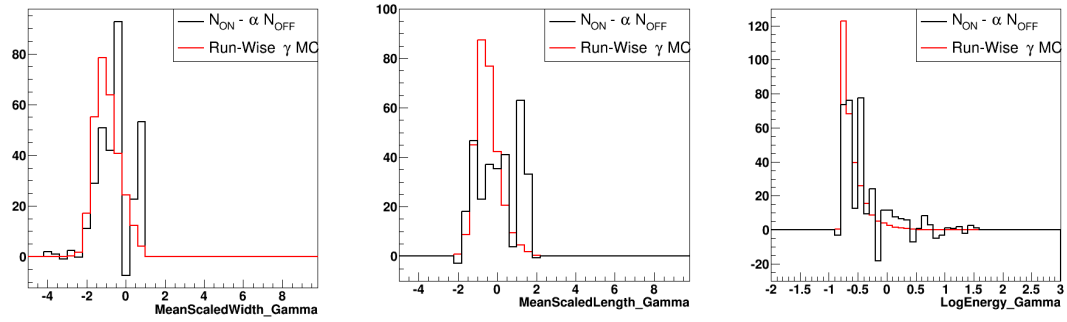

Figure 4.8: Cut parameter mean scaled width (*left*) and mean scaled length (*middle*) of γ-events for data (black) and run-wise simulations (red). Reconstructed energy of γ-events (*right*).

analysis results. With the help of run-wise simulations, the influence of large patterns of turned-off pixels (due to NSB) could be estimated to be negligible compared to the influence of the NSB itself. Despite the problems apparent in the results of the Hillas analysis the fact that there is a significant detection in both DS-I and DS-II is sufficient motivation to extend the analysis to more advanced analysis techniques.

4.3 Semi-analytical shower model analysis of η Carinae

The Model analysis technique, as outlined in section 3.4.2, is based on a likelihood fit that estimates the shower parameters from a comparison between modelled templates and data. DS-I has been analysed in monoscopic and stereoscopic mode, while DS-II only provides single telescope data and thus was analysed in monoscopic fashion only. The applied parameter cuts are summarised in table 4.4 and 4.5 for the single and multiple telescope analyses, respectively. Mono analyses provide lower energy thresholds while stereo analyses provide more stability against NSB at the extent of less performance below $\sim$ 300 GeV [figure 4.14 in 120, 140, 95]. Since only half of the total data set is available in stereoscopic mode, focus will lie on the monoscopic analysis; stereo results will be given when available.

At the beginning of this subchapter the configurations of the applied analyses are introduced. Before discussing the results, more low-level tests are performed. Results are presented in several subsections, starting with the detection and more studies of the NSB and culminating in the discussion and interpretation.

Cut	Std Mono	this
Direction Error [°]	[0,0.3]	[0,0.3]
Primary Depth	[−1.1,1.3]	[−1.1,1.3]
Mean Scaled Shower Goodness	[−4,0.7]	[−4,0.7]
Uniform NSB Goodness	-	$\geq$ 50
NSB Goodness	$\geq$ 19	-
Minimum Charge [p.e.]	60	60
Minimum Containment Fraction [%]	50	50
Minimum Number of Pixels above 5 PE	5	5
Nominal Distance [°]	[0,1.4]	[0,1.4]

Table 4.4: Standard cuts in the Model mono analysis and cuts used in this analysis.

4.3.1 Analysis configurations

In total four analyses are performed: monoscopic analyses of DS-I and DS-II, first separately and then combined, and a stereoscopic analysis of DS-I. The cut parameters in the monoscopic analyses follow the Paris Analysis *Standard Mono* configuration with the exception of the background rejection parameter (compare table 4.4). As discussed in 3.4.2, the uniform NSB goodness G_{UNSB} replaces the standard background rejection parameter NSB goodness. For the stereoscopic analysis of DS-I, a (predefined) configuration with loose cuts is applied to reach a low energy threshold (compare table 4.5). As in the Hillas analysis, a circle of $0.44\,^\circ$ around the position of η Carinae is excluded for the definition of OFF regions. The ON regions is restricted with a $\vartheta^2 = 0.04\,\mathrm{deg}^2$ cut. The background is estimated with the ring background method for sky maps and with the reflected background method (definitions in section 3.5) for the spectral energy distribution presented in section 4.3.7. In section 4.2.1, a higher cleaning was introduced to help limit the admittance of NSB photons into γ-ray showers. The Model fit exploits information of all pixels but it benefits from the new pixel threshold cleaning indirectly. The starting parameters for the log-likelihood fit in the reconstruction with Paris Analysis are found in the results of the Hillas analysis as described in 3.4.2. For every fitted event the seed was stored to evaluate which cleaning level was chosen. In $\sim 90\%$ of reconstructed showers the cleaning level that gave the best fit result was the newly introduced $(6, 12)$ p.e. cleaning, confirming the choice of this increased cleaning level in the first place.

Cut	Std Stereo	this
Direction Error [°]	[0,0.2]	[0,0.2]
Primary Depth	[−1.1,3.4]	[−1.1,3.4]
Mean Scaled Shower Goodness	[−4,0.9]	[−4,0.9]
Mean Scaled Background Goodness	≤ 2	≤ 2
Minimum Charge CT1-4, CT5 [p.e.]	60, 60	20, 40
Minimum Containment Fraction [%]	50	50
Minimum Number of Pixels above 5 p.e.	5	0
Nominal Distance [°]	[0,2]	[0,2]

Table 4.5: Standard cuts in the Model stereo analysis and cuts used in this analysis.

4.3.2 Low-level checks

Intensity maps for all runs have been checked before performing the Hillas analysis (in section 4.2.2)). As a new tool to monitor the impact of the NSB between the steps of calibration that acts on the intensity maps and the spatial distribution of *CoG*s in the focal plane of a telescope, the *pixel participation fraction* was introduced. It states the percentage a pixel took part in a triggered event. Hotspots due to NSB photons are easy to identify in maps of the pixel participation fraction before they enter the reconstruction. Figure 4.9 shows the pixel participation fraction for the mono and stereo analyses of DS-I. Both maps show a sufficient homogeneous distribution without hotspots or holes.

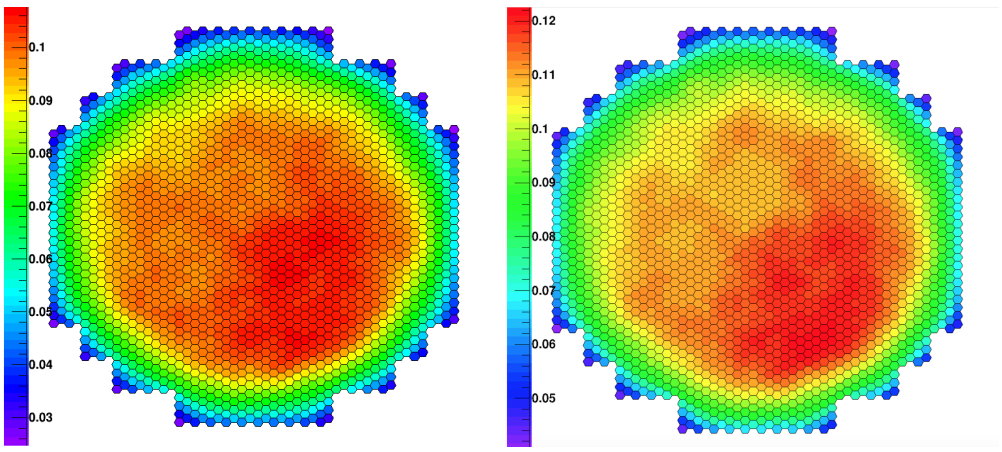

Figure 4.9: Pixel participation fraction in CT5 for the mono (*left*) and stereo (*right*) analysis of DS-I. The colour scale depicts how often a single pixel took part in a shower (every hexagon is a pixel).

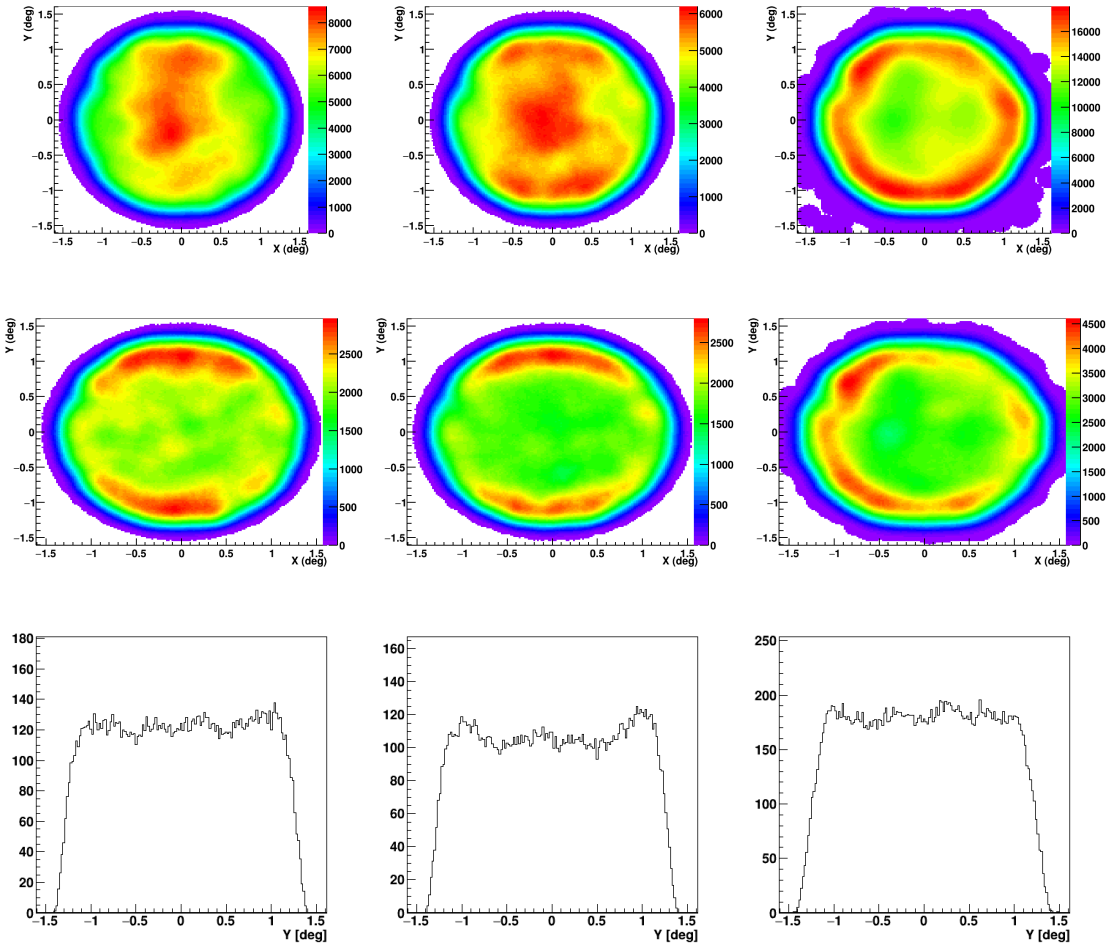

Figure 4.10: *CoG* distributions of all events (*top row*) and γ-like events (*second row*)of DS-I (*left*), DS-II (*middle*) mono analyses and DS-I stereo analysis (*right*). The colour scale indicates the frequentness of CoGs at a certain position in arbitrary units (because of smoothing). The maps are smoothed by integrating circles of 0.07/ 0.16 deg radius (the pixel radius of CT5/ CT1-4). The used coordinate system is the nominal system [131]. Projections along the y-axis of the *CoG* maps for γ-like events (*last row*).

With *CoG* maps the distribution of reconstructed shower *CoG* are depicted in the focal plane of the telescope(s). In figure 4.10 maps for γ-like events and all events of the mono and stereo analyses of DS-I and the mono analysis of DS-II are shown. The γ-like event maps show a ring-like structure with a radius of roughly 1 ° where most *CoG* fall, which is more pronounced in the stereo analysis of DS-I (fig. 4.10, *right*). In the stereo analysis the ring is also visible in the map for all events, while in the mono analyses it is only visible in the γ-like event maps. This excludes the NSB cut parameter in the

mono analysis as the origin. However, projections along the y-axis of the (un-smoothed) γ-like CoG maps (figure 4.10, *last row*) reveal that the effect is rather weak and the distribution can thus be considered sufficiently homogeneous.

Figure 4.11 depicts the acceptance of the mono and stereo analyses of DS-I and the mono analysis of DS-II to γ-like and background events. The right column shows the acceptance to background events. For the mono analyses the impact of the G_{UNSB} cut is visible in the more homogeneous acceptance to background events. In contrast, the γ-candidate acceptance (left column of fig. 4.11) shows some structure. The acceptance to γ-like and background events of the stereo analysis (last row of fig. 4.11) is more homogeneous. The bigger FoV of the CT1-4 telescopes is reflected in the bigger radii of acceptance in figure 4.11.

With homogeneous distributions in the pixel participation fraction and CoG maps the influence of the inhomogeneous NSB is ensured to be restricted. The acceptance to γ-like events in the mono analyses shows some small scale structure which is caused by the background rejection parameter G_{UNSB}. This cannot be changed in the current set-up of Paris Analysis and any following implications will be closely monitored.

(a) γ acceptance (b) Background acceptance

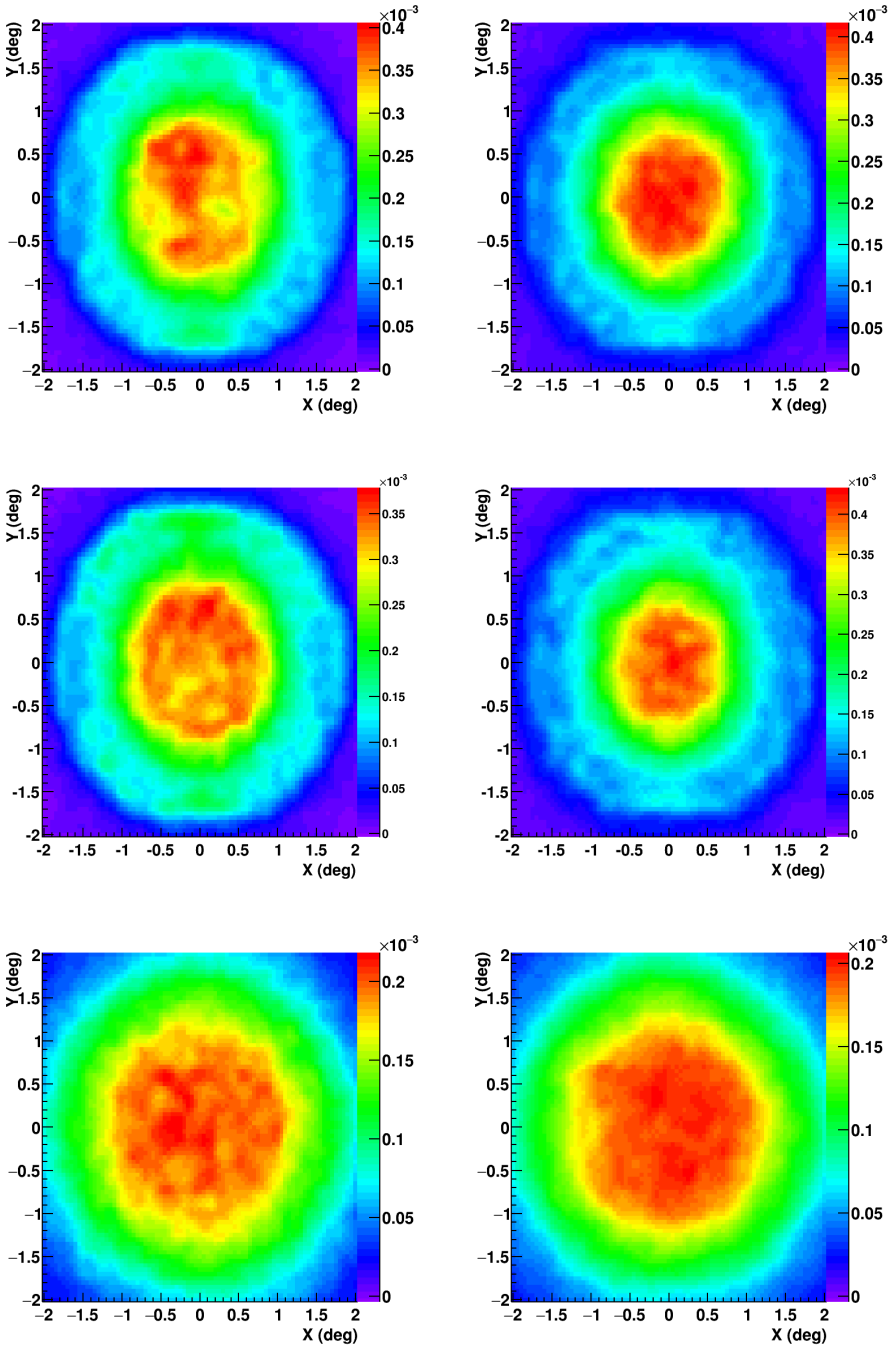

Figure 4.11: 2D acceptance maps of the mono analysis of DS-I (*first row*), the mono analysis of DS-II (*second row*) and stereo analysis of DS-I (*third row*) in the *Nominal System* [131]. The camera centre is at position (0,0). The source position changes from run to run in this coordinate system.

4.3.3 Detection of η Carinae

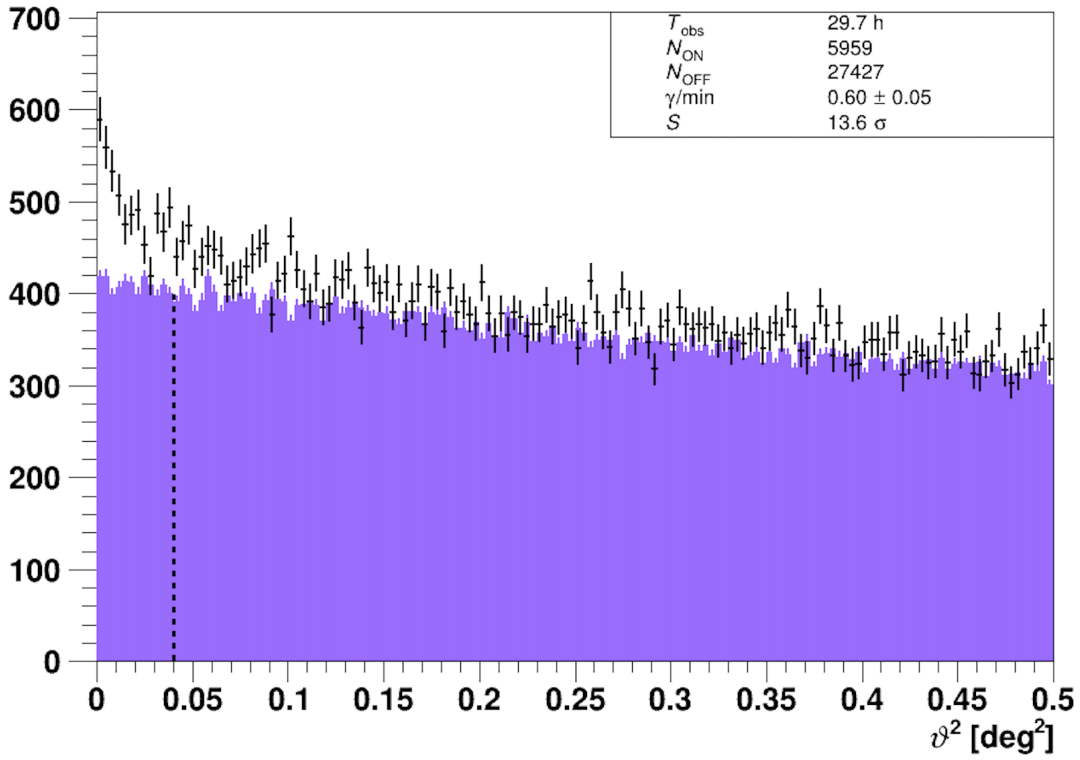

Figure 4.12: Distribution of ON and OFF events as a function of squared angular distance from the source ϑ^2 for the mono analysis of DS-I and DS-II together. ON events in black, OFF events in violet. The dashed black line depicts the ϑ^2 cut that was applied to define the ON region.

	Mono	DS-I	DS-II	DS-I + DS-II	Stereo DS-I
Number of excess events		526	541	1070	464
Significance		8.9	10.3	13.6	7.2

Table 4.6: Significances of excess events above background calculated following equations 3.14 and 3.15 for all analysis configurations.

Excess γ-ray emission towards η Carinae is detected in all data sets and analysis configurations with significances above $7\,\sigma$. Table 4.6 lists the significances obtained with equations 3.14 and 3.15 for each data set and analysis configuration. The distribution of ON and OFF events as a function of squared angular distance from the

source ϑ^2 is shown in figure 4.12 for the mono analysis of DS-I and DS-II (analogous to figure 4.4 of the Hillas analysis). If not stated otherwise, in all results presented the background was estimated with the ring background technique. The 68% containment radius R_{68} is 0.26 °, which is broadened compared to the standard mono PSF of H.E.S.S. ($R_{68,std} = 0.15\,^\circ$ [119]). Also visible in figure 4.12 is the amount of background depicted in purple.

Figure 4.13 shows significance maps of the mono analysis of DS-II and the stereo analysis of DS-I. In both maps the emission seems to be extended. This will be studied in the next section.

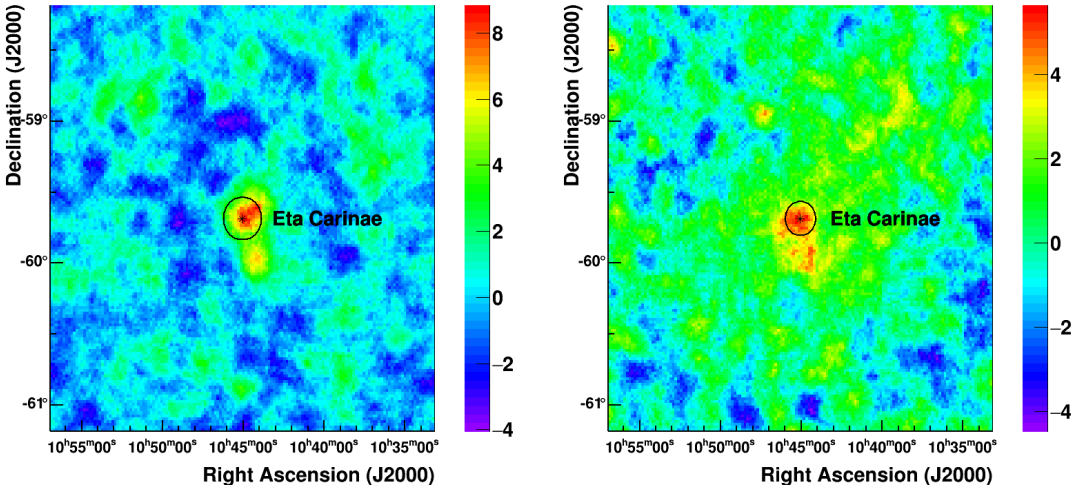

Figure 4.13: Significance maps of the mono analysis of DS-II (*left*) and the stereo analysis of DS-I (*right*). The black circles denote the standard PSF. The colour scale states significances.

4.3.4 Studies of the PSF broadening under high NSB

For the investigation of the widening of the PSF run-wise simulations were used. In section 4.2.3, the influence of the turned-off pixels was estimated with the use of run-wise simulations and found not to have a big impact on the broadening of the PSF observed in the Hillas analysis. This should also pertain for the Paris Analysis results since non-operating pixels are identified and sorted out in the calibration process. The contribution of those pixels to the smearing of the PSF is accounted for by only simulating the operating pixels in the following.

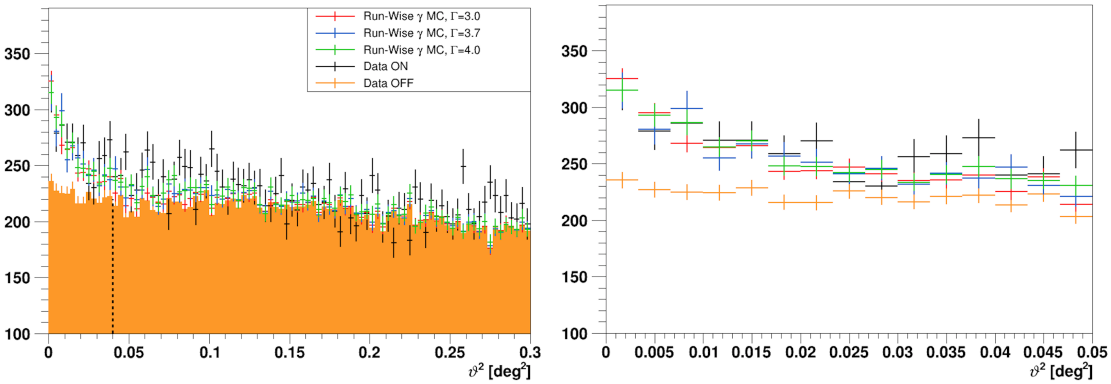

Figure 4.14: *Left*: Distribution of the number of ON events (black) and $\alpha \cdot N_{OFF}$ (orange) as a function of ϑ^2 for the analysis of DS-I with Model Std Mono in comparison to run-wise simulations with a varying power-law index Γ. The dashed black line indicates the cut value of $\vartheta^2_{\mathrm{max}}$. *Right*: Zoom into the ϑ^2 range $[0,\, 0.05]\,\mathrm{deg}^2$ of the left figure.

One uncertainty in the simulation is the spectral index of the power-law function (equation 3.20) that is used to describe the flux from the source. The spectral energy distribution will be reconstructed later on, but the true distribution is unknown. Run-wise simulations with three different power-law indices were analysed for the mono analyses of DS-I and DS-II. The ϑ^2 distributions are shown in figures 4.14 and 4.15. Typical reconstructed indices of galactic γ-ray sources observed with H.E.S.S. lie below $\Gamma = 3$. For η Carinae a "softer" index is expected to be compatible with the reported upper limits on the γ-ray flux [94]. The smallest index simulated is $\Gamma = 3.0$ (red). Its distribution falls steeply off and is matching the distribution of ON events the least. The distributions for $\Gamma = 3.7$ and $\Gamma = 4.0$ reproduce the ON event distribution quite well. "Softer" indices lead to broader peaks due to more low-energy events.

Additionally to extracting the PSF to quantify the broadening of R_{68} in data and run-wise simulations, in the next step 2-D distributions of the γ-candidates will be fit and compared to the results of the 2-D fits of γ-candidate events in the data sets. Figure 4.13 shows the 2-D significance maps for DS-II mono (*left*) and DS-I stereo analysis (*right*). The black circle denotes the standard PSF of the mono and stereo analysis ($R^{mono}_{68,std} = 0.15\,^\circ$ and $R^{stereo}_{68,std} = 0.12\,^\circ$). To fit the spatial distribution in 2-D the observed number of events is compared to the expected number. The expected number of γ-ray events is calculated, similar to the spectral reconstruction described in section 3.6, via a forward folding approach and using a Poisson probability $P(N_{ON}, N_{OFF}|\, n_\gamma, n_{Bck})$

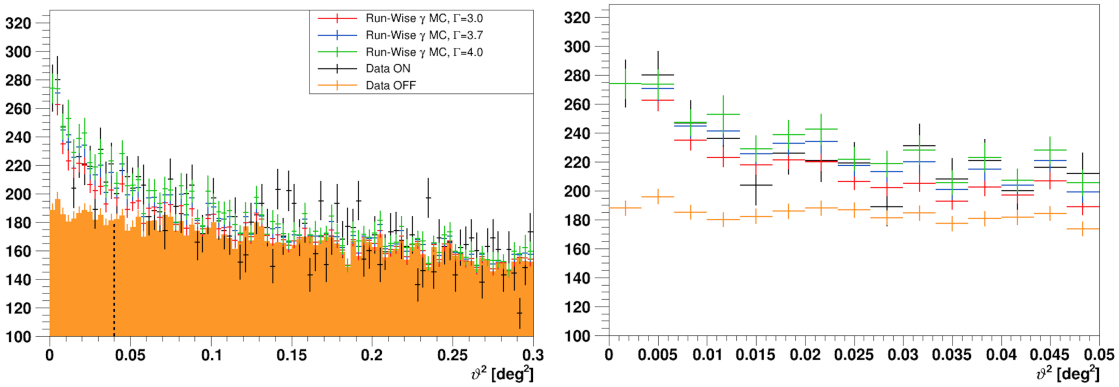

Figure 4.15: *Left*: Distribution of the number of ON events (black) and $\alpha \cdot N_{OFF}$ (orange) as a function of ϑ^2 for the analysis of DS-II with Model Std Mono in comparison to run-wise simulations with a varying power-law index Γ. The dashed black line indicates the cut value of $\vartheta^2_{\mathrm{max}}$. The background was estimated using the *Ring Background* method. *Right*: Zoom into the ϑ^2 range $[0,\, 0.05]\,\mathrm{deg}^2$ of the left figure.

(eqn. 3.21). An assumption about the source morphology shape, e.g. point-like, is necessary. The instrument response function (introduced in 3.6) that includes the effective area and energy resolution for a specific analysis configuration is tabulated and stored as a "look-up" table. IRFs can be produced either using classical Monte Carlo simulations or run-wise simulations. Then a log-likelihood maximization is performed to find the number of background events. The log-likelihood is then maximized against the parameters of the assumed source morphology. The result of the 2-D morphology fit is a best fit position and spatial extension of the fitted source.

In all analyses, the spatial excess event distribution in data is broader than the standard PSF if classical simulations are used. For the angular resolution of H.E.S.S. and assuming an origin of the γ-ray emission inside the CWR as suggested by the variability seen in $Fermi-$LAT data, η Carinae should be compatible with a point-like source which means compatible with the instrument's PSF. Considering the challenging observation conditions, it is probable that the extension beyond the PSF is caused by systematic effects connected to the inhomogeneous NSB and its incorrect treatment in the classical simulations. This statement is also supported by the fact that the extension in the Hillas analysis is larger than in the Model analysis. The ϑ^2 distributions in figures 4.14 and 4.15 suggest that the broadened PSF visible in the data sets of η Carinae can be understood if the spectral energy distribution followed a power-law with a softer index than 3. This will be investigated in the following with 2-D fits using

Mono DS-I	classic MC	RWS, $\Gamma = 3.0$	RWS, $\Gamma = 3.7$	RWS, $\Gamma = 4.0$
Source extension [°]	0.088 ± 0.012	0.065 ± 0.015	0.037 ± 0.022	0.038 ± 0.020
Fit position, RA	161.161 ± 0.026	161.170 ± 0.027	161.152 ± 0.028	161.171 ± 0.029
Dec [°]	-59.675 ± 0.013	-59.674 ± 0.013	-59.673 ± 0.014	-59.673 ± 0.014

Table 4.7: Fit results of the source extension and position in DS-I mono sky maps for classical simulations and run-wise (RWS) simulations with different power-law indices.

Stereo DS-I	classic MC	RWS, $\Gamma = 3.0$
Source extension [°]	0.143 ± 0.021	0.042 ± 0.033
Fit position, RA	161.332 ± 0.044	
Dec [°]	-59.735 ± 0.021	-

Table 4.8: Fit results of the source extension and position in DS-I stereo sky maps for classical simulations and run-wise (RWS) simulations with a power-law index of $\Gamma = 3.0$.

IRFs produced with run-wise simulations with indices $\Gamma = 3.0, 3.7, 4.0$. The choice of indices is motivated by the steep spectra found when reconstructing the spectra with classical IRFs (compare section 4.3.7). Figure 4.16 shows a representative 2-D map of γ-candidate events for run-wise simulations with a simulated power-law index of $\Gamma = 4.0$. Tables 4.7, 4.8 and 4.9 summarize the results of the fit of the spatial extension of η Carinae in all analysis and data set configurations.

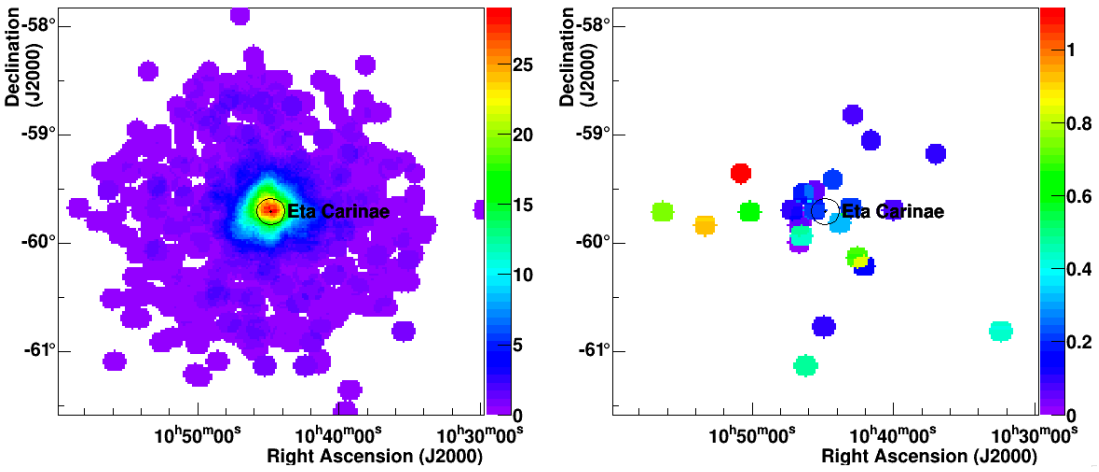

Figure 4.16: Smoothed run-wise mono γ candidate (*left*) and γ-like background map (*right*) for a spectral index of $\Gamma = 4.0$ and DS-II.

Mono DS-II	classic MC	RWS, $\Gamma = 3.0$	RWS, $\Gamma = 3.7$	RWS, $\Gamma = 4.0$
Source extension [°]	0.098 ± 0.010	0.047 ± 0.016	0*	0*
Fit position, RA	161.164 ± 0.022	161.143 ± 0.023	161.146 ± 0.027	161.153 ± 0.031
Dec [°]	-59.667 $\pm$ 0.011	-59.665 $\pm$ 0.011	-59.666 $\pm$ 0.013	-59.667 $\pm$ 0.013

Table 4.9: Fit results of the source extension and position in DS-II mono sky maps for classical simulations and run-wise (RWS) simulations with different power-law indices. Results denoted with '*' are obtained with 1D fits of ϑ^2 distributions because the statistic in the sky map was not sufficient for a 2D sky map fit.

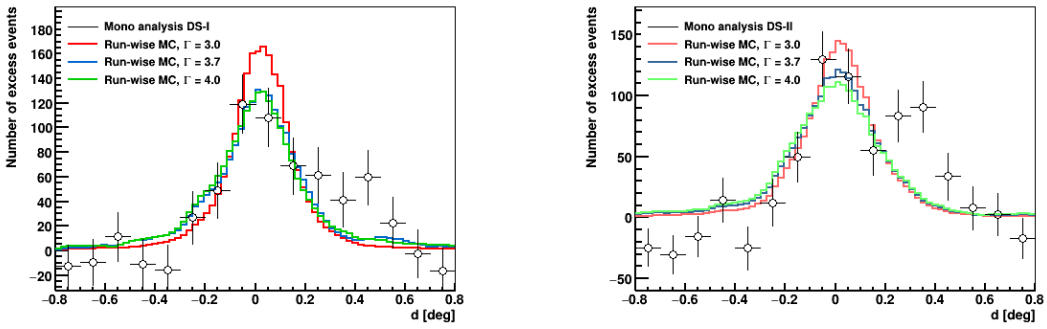

Figure 4.17: Profile plots of a box with length 1.6 ° and width 0.2° through the position of η Carinae (at $x = 0\,°$ here) in data and run-wise simulation sky maps (compare figure 4.16). The position of the box is indicated in figure 4.18. Comparison between mono analysis of DS-I (*left*) and DS-II (*right*) with run-wise simulations with different power-law indices.

Run-wise simulations following a power-law with index $\Gamma \geq 3.7$ reproduce the broadening of the PSF compared to the standard PSF. This shows that this broadening and also the extension visible in the sky maps, e.g. in figure 4.13, can be interpreted as a consequence of the combination of the turned-off pixels ($\sim 8\%$), the NSB level ($\sim 30\%$) and the soft index of the spectral energy distribution of η Carinae. The best fit source positions have a distance to η Carinae of $\sim 0.05\,°$. Figure 4.17 shows the profiles of an excerpt of the sky maps of DS-I and DS-II (depicted in figure 4.18) in comparison to the profiles of run-wise simulations with different power-law indices. These profiles and the maps in section 4.3.3 show an additional excess of emission that will be investigated in the next section.

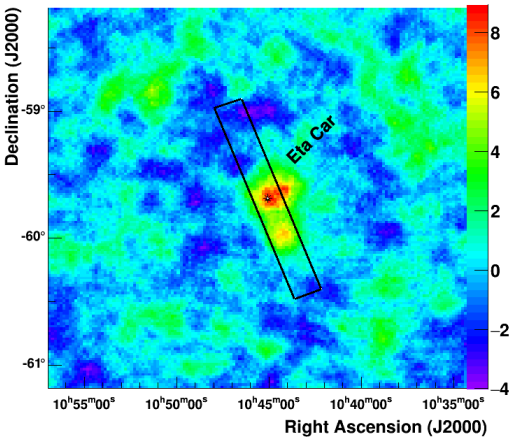

Figure 4.18: Significance map of the mono analysis of DS-II with the box that is projected in in figures 4.17.

4.3.5 HOTS J1044-5957: A hint for a new source

While the excess in the data is described well by the run-wise simulations with indices $\Gamma = 3.7, 4.0$, a weaker emission component is visible at a distance of $\sim 0.29\,^\circ$ to the source (at $0\,^\circ$) in the sky maps. The attempt to fit two sources to the sky map did not lead to converging fit results. A profile plot (same excerpt as shown in fig. 4.18) together with the measured NSB is shown in fig. 4.19. In this profile, a fit with two Gaussian functions is preferred over a single Gaussian at 95 % confidence level. As indicated in figure 4.19, the NSB level is also above 700 MHz at the position of the hot spot. The NSB level per pixel in the plot is corrected for by substracting the number of turned-off pixels. A possible contamination of η Carinae by excess of the hotspot is examinated by fitting two Gaussian functions to the profile in fig. 4.19 and calculating their overlap. With respect to the full integral of the Gaussian function describing the excess of η Carinae, this amounts to 16 %. A dedicated analysis centred at the hot spot at RA $10^\mathrm{h}\,44^\mathrm{m}\,22^\mathrm{s}$ and Dec $-59^\circ\,57'\,52''$ (J2000), in the following called HOTS J1044-5957, was performed and yielded an excess with significance of $4.6\,\sigma$ in the stereo analysis of DS-I and $8.2\,\sigma$ in the mono analysis of DS-I + DS-II (the analysis configurations are the same as for η Carinae, despite the ϑ^2 cut that was set to the standard value of $0.02\,^\circ$ for the mono analysis).

Figure 4.20 shows the NSB map marked with the positions of stellar clusters (open triangles), stars with apparent magnitude above 6 (open circles) and sources of the

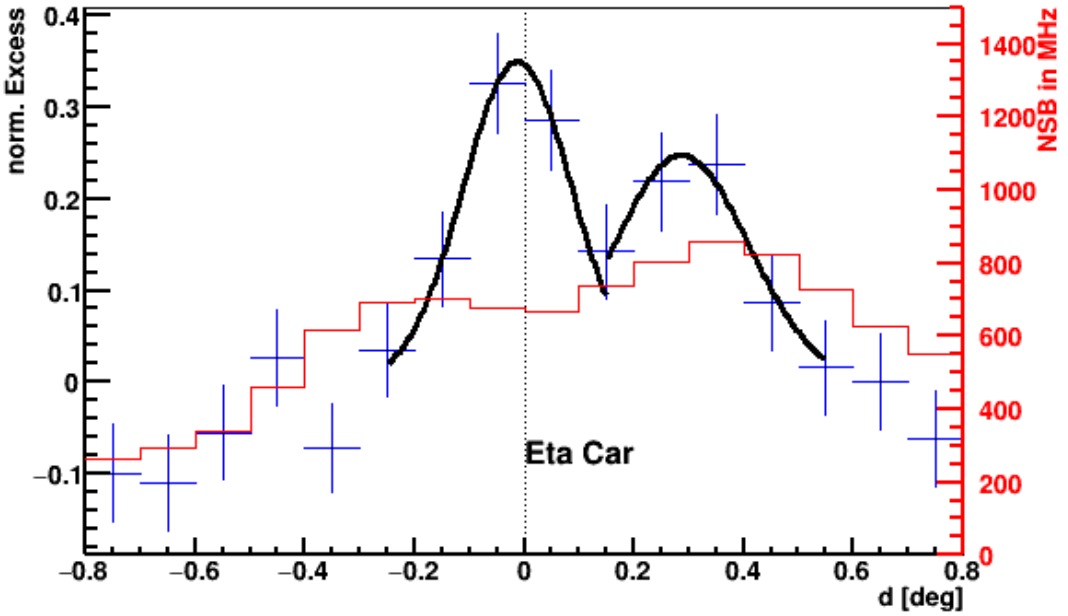

Figure 4.19: Profile plot of the box depicted in fig. 4.18 with two Gaussian functions fitted to η Carinae and the hotspot south of it. The NSB level per pixel in the plot is corrected for by substracting the number of turned-off pixels.

Fermi−LAT 3FGL catalog (open stars). η Carinae is at the centre of the map, indicated with a star. The region brightest in NSB in the southwest of the Carina nebula, where HOTS J1044-5957 is situated, hosts open stellar cluster Collinder 228. Two bright and massive members are the Wolf-Rayet star HD 93131 (WR 24) and the double binary system HD 93206. HD 93131 is one of the most luminous stars known with a bolometric luminosity of $\log(L) = 6.35\,\mathrm{L}_\odot$ and has a mass of $54\,\mathrm{M}_\odot$ that is reduced by $40 \times 10^{-6}\,\mathrm{M}_\odot$ per year. It's stellar wind exhibits a terminal wind velocity of $v_\infty = 2160\,\mathrm{km\,s^{-1}}$ [143, 144]. HD 93206, also known as QZ Car, is composed of at least four young ($4 \pm 1\,\mathrm{Myr}$) massive stars with masses ranging from ~ 20 to $\sim 43\,\mathrm{M}_\odot$ and about as bright as HD 93131 with $\log(L) = 6.48\,\mathrm{L}_\odot$ [145, 146]. An O-type and a B-type star form a binary with an orbital period of $\sim 20\,\mathrm{d}$ and eccentricity $e = 0.34$ (system A) [147, 148]. The second binary is an eclipsing binary of two O-type stars and has a short period of 6 d (system B) [148]. The orbital period of the quaternary star system is $p_4 = 49.5 \pm 1.0\,\mathrm{yr}$ [145]. The four stars drive stellar winds (mass-loss rates $\dot{M}$ and terminal wind velocities v_∞ in table 4.10). Beside the wind-wind collisions of the binary systems, a mutual wind-wind collision, where the winds of the binary systems collide,

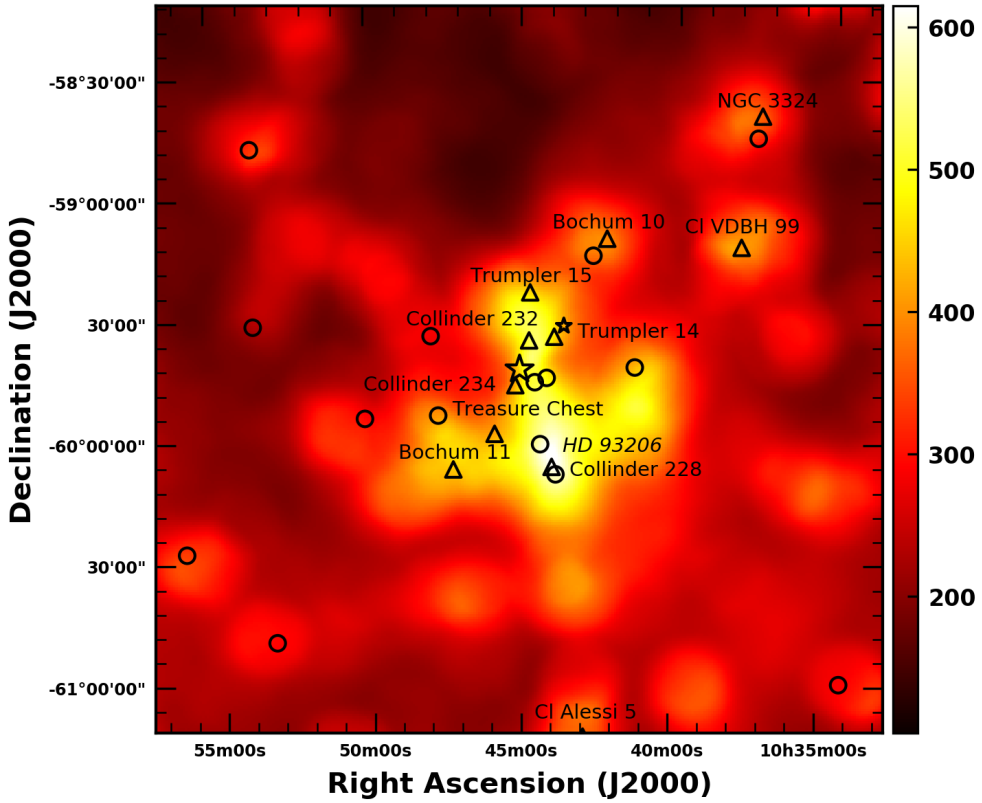

Figure 4.20: Map of the measured NSB in MHz (colour scale) with all stars with an apparent magnitude $m_v \geq 6$ marked with open circles, all stellar clusters marked with open triangles and sources detected by *Fermi*−LAT marked with stars (only η Carinae and 3FGL J1043.6-5930). The map is smoothed with the pixel radius of CT5 0.07 °. The maximum NSB in this plot is reduced by the shut-down of pixels where the NSB is highest.

is possible. In binary systems of massive stars, additional thermal X-ray emission can be generated as a result of wind-wind collision shocks [149]. QZ Car has been observed in X-rays with the *Chandra X-ray Observatory* as part of the *Chandra Carina Complex Project, CCCP* [150, 151]. The X-ray emission can be described by a three temperature thermal plasma model with the hottest component at 2 keV and as a combination of contributions from the single stars and the mutual wind-wind collision. The wind-wind collisions in systems A and B are probably not contributing to the observed X-ray flux as a wind-wind momentum balance does not occur [152]. No non-thermal emission towards QZ Car has been observed.

The hot spot HOTS J1044-5957 is situated at the position of maximum NSB. This is

Component	A1	A2	B1	B2
$\dot{M}$ [$M_\odot\,yr^{-1}$]	2.2×10^{-6}	2.4×10^{-9}	5.2×10^{-7}	6.4×10^{-8}
v_∞ [$km\,s^{-1}$]	2140	1040	2220	2850
m [$M_\odot$]	43 ± 3	$19 +3 -7$	30 ± 3	20 ± 3

Table 4.10: Mass-loss rates and terminal wind velocities for the components of the double binary system QZ Car [152], masses [145].

also where pixels were shut-down which is why the maximum NSB value of ~ 600 MHz in figures 4.22 should rather be interpreted as a lower limit. In the light of this complex background conditions, the analysis of HOTS J1044-5957 gives a hint for a new source, but cannot claim a detection. To dispel concerns about the impact of the NSB on the excess of HOTS J1044-5957, a robust detection in the stereo analysis would be needed, as it is the case for η Carinae.

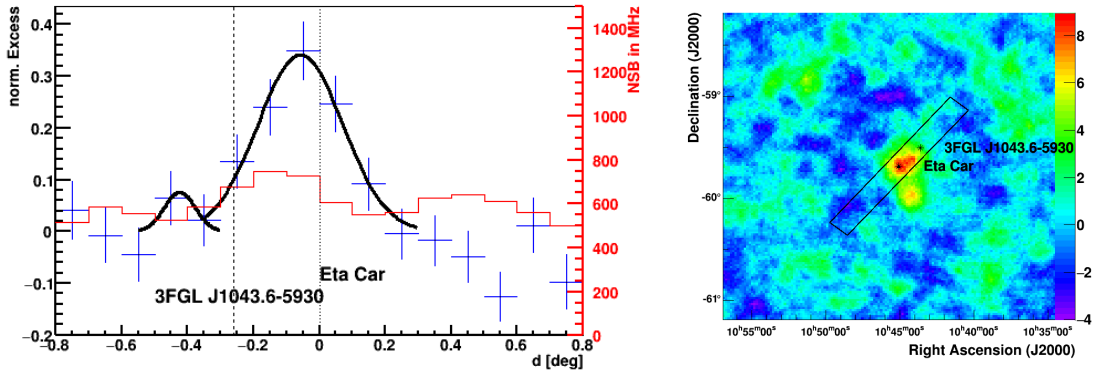

Figure 4.21: Profile through η Carinae and 3FGL J1043.6-5930 fitted with two Gaussian functions to estimate a potential leakage of 3FGL J1043.6-5930 into η Carinae (*left*). Orientation of the projected excerpt (*right*).

Nearby η Carinae ($\sim 0.27\,°$) exists a weak, unassociated 3FGL source, 3FGL J1043.6-5930. It was detected by $Fermi-$LAT with $6\,\sigma$, a power-law index of 2.07 ± 0.11 and a flux of $\phi = 1.93 \cdot 10^{-9} \pm 4.52 \cdot 10^{-10}\,ph\,cm^{-2}\,s^{-1}$ [153]. To examine a possible contamination a profile plot through both sources was produced and the possible contamination was estimated by fitting Gaussian functions to η Carinae and 3FGL J1043.6-5930 and calculating the fraction of leakage (figure 4.21, *left*). This fraction amounts to 3 %, which leads to the conclusion that a possible contamination from this source is negligible.

4.3.6 NSB investigations

To study a possible correlation of the excess towards η Carinae as well as HOTS J1044-5957 in the sky maps with the NSB, the measured NSB is plotted with overlaid significance contours in figure 4.22. The NSB map shows strong features around the position of η Carinae and south of it where also the maximum values are measured. The structure of the high NSB region is highly inhomogeneous, extended over $\geq 0.3\,^\circ$ and increased by factors of $\sim(5-10)$ compared to the average Galactic value of $\sim$100 MHz. Most importantly, η Carinae's position and the most significant region lie in a region between two extended very high NSB regions and the significance does not trace the NSB level, which would be expected if it was only NSB-correlated excess. Below η Carinae the hot spot is visible with an excess of events of $\sim 8.2\,\sigma$.

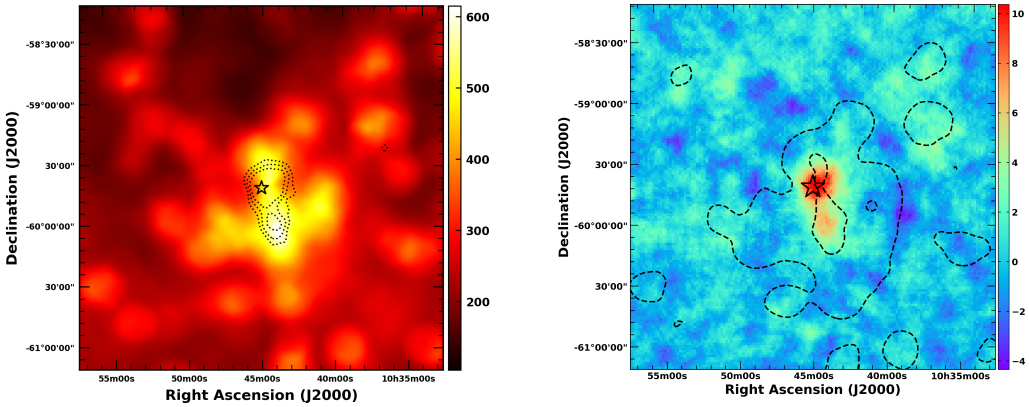

Figure 4.22: Map of the measured NSB in MHz (colour scale) with significance contours (*left*). The contours depict 3.5, 4.75 and 6 σ excess (mono analysis of DS-I and DS-II). The map is smoothed with the pixel radius of CT5 0.07 °. The optical position of η Carinae is marked with a star. The maximum NSB in this plot is reduced by the shut-down of pixels where the NSB is highest. On the right hand side, the significance map of the mono analysis of DS-I and DS-II with contours of 300 and 500 MHz NSB (*right*).

Figure 4.22, *right* shows the significance map of the mono analysis of DS-I and DS-II overlaid with 300 and 500 MHz NSB contours. η Carinae lies inside the 300 MHz contour and close to the 500 MHz contour. On the right hand side, stars and stellar clusters are marked and the PSF from run-wise simulations is shown.

To test the impact of large patterns of non-operating pixels the correlation between

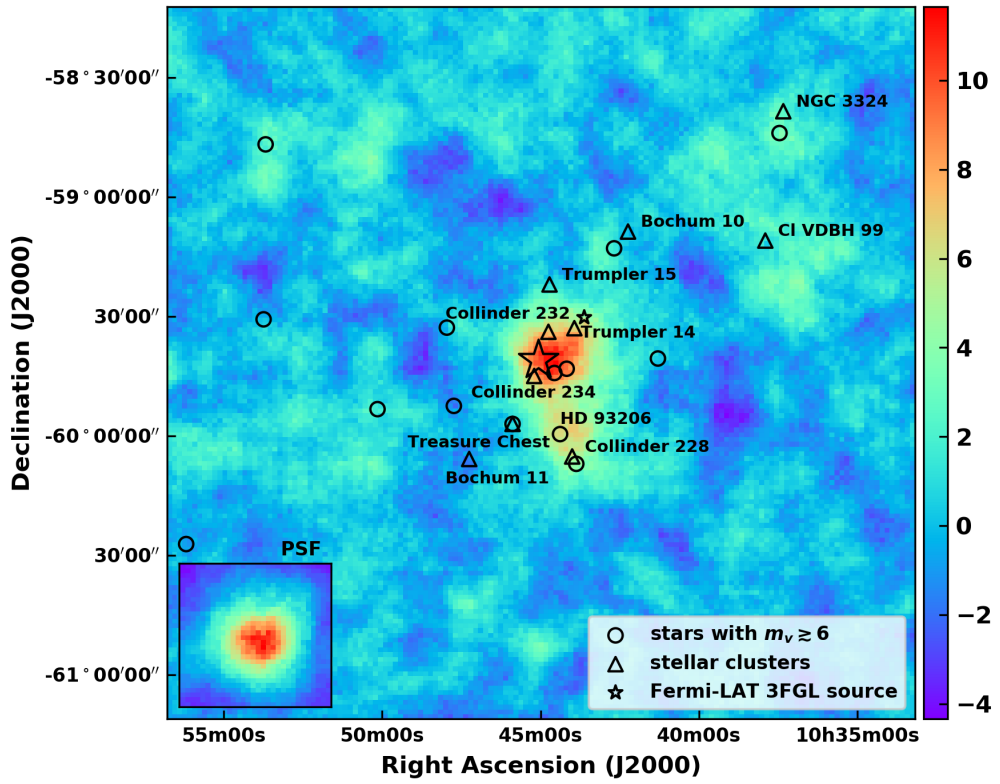

Figure 4.23: Significance map of the mono analysis of DS-I and DS-II with markers for stars (open circles), stellar clusters (open triangles and labels) and the source 3FGL J1043.6-5930. The inlay on the lower left hand side depicts the PSF simulated with run-wise simulations.

excess events and NSB in Hz per pixel was investigated. Figure 4.24, *right*, shows an unsmoothed map of the measured NSB level. White spots are due to pixels that are turned-off to protect them from high currents. The region on the top left hand side of the map was projected in excess events and NSB in MHz (figure 4.24, *left*). The number of excess events per GHz NSB is calculated by fitting the ratio of excess events and NSB per pixel with a constant and amounts to 11.98 ± 7.10 (non-operating pixels are substracted). This number is an estimate of the expected NSB contribution per GHz NSB and pixel in this region with a large pattern of non-operating pixels. Comparing this to the average number of excess events per pixel and GHz NSB in a box centred around the source position amounts to 33.70 ± 8.98, so a rough estimate of the contamination of the excess at the position of η Carinae with NSB would be one third. However, this estimate is per GHz NSB level and the NSB at the exact position of η Carinae is unknown because it is too high for the PMTs. The mean NSB level in the

box is ~ 520 MHz, which is surprisingly low, but also not too meaningful because the NSB level is inhomogeneous and the strongest NSB values are not taken into account. Another difficulty of the comparison of NSB level and excess event correlations between η Carinae's position and another position lies in the different acceptances to γ-like and background events. Hence, an estimation of the exact amount of NSB correlated events in excess events of η Carinae is not straightforward.

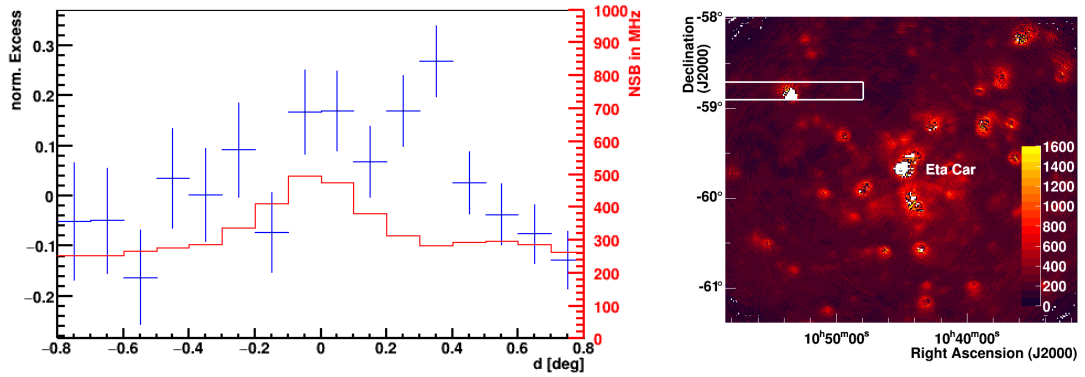

Figure 4.24: Profile through a pattern of turned-off pixels (*left*). Measured NSB map without smoothing (*right*). White spots are due to turned-off pixels. The colour scale is NSB in MHz per pixel.

4.3.7 The γ-ray spectrum of η Carinae and its light curve

The intrinsic γ-ray spectrum of η Carinae was reconstructed following the approach described in section 3.6. Classical simulations were used for the determination of the IRFs because run-wise IRFs were not available yet. The energy threshold is set corresponding to at least 15 % of the effective area. Figure 4.25 shows the spectra for DS-I and DS-II mono analyses and statistical uncertainties on the flux. The spectra agree within statistical errors and connect to the highest-energy $Fermi-$LAT spectral points. The mono analyses are also compatible with the H.E.S.S. upper limits, although the upper limits cover a different phase than the current analyses [94]. The stereo analysis spectrum seems to contradict the upper limits, but this can be attributed to the missing treatment of systematic uncertainties: taking into account a systematic uncertainty on the flux level of 20 %, as in previous H.E.S.S. analyses (compare [140]), the stereo spectrum is compatible with both the monoscopic spectra and the upper limits from 2012. Systematic errors on the reconstructed spectra will be estimated when the run-wise IRFs

are ready, by comparing the run-wise results with the results of the cross-check analysis.

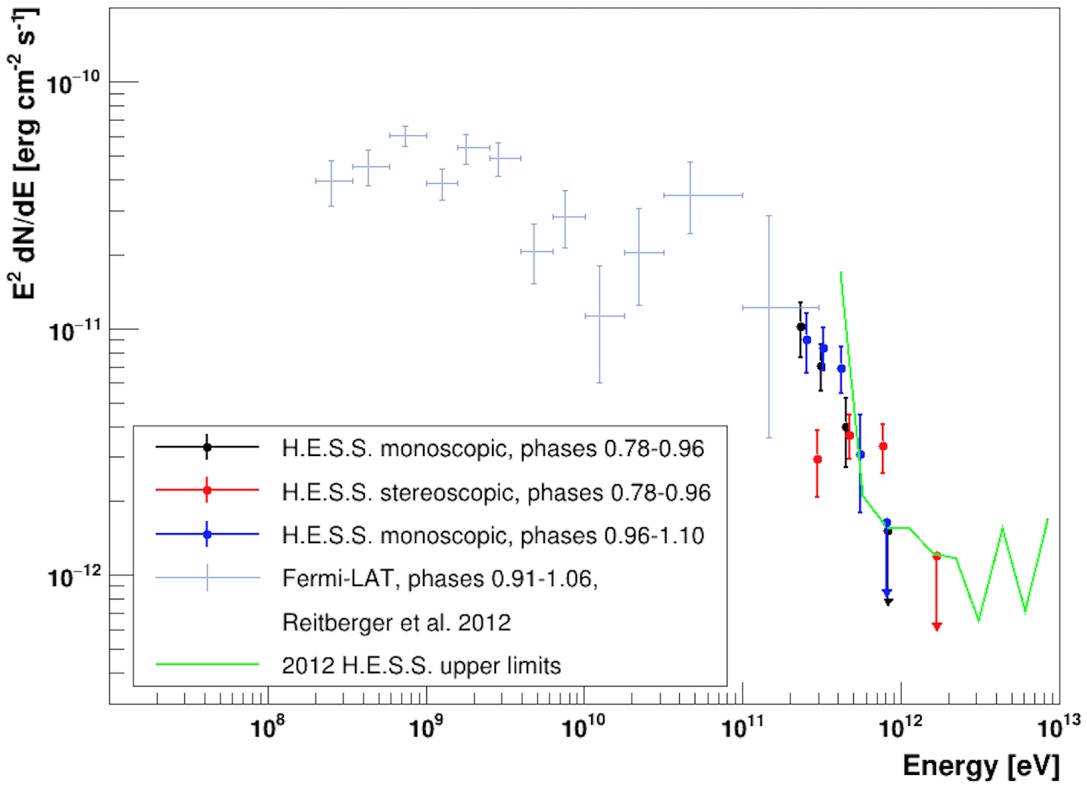

Figure 4.25: Spectrum of the mono analyses of DS-I (phases 0.78-0.96) and DS-II (0.96-1.10), the stereo analysis of DS-I, the upper limits publishes by H.E.S.S. in 2012 [94] and the high-energy component observed by *Fermi*−LAT [90].

The best-fit spectral index for the mono analysis of DS-I is $\Gamma_{\mathrm{DS-I}} = 3.9 \pm 0.4_{\mathrm{stat}}$ above an energy threshold of 190 GeV. The flux norm at the decorrelation energy, where the uncertainties are smallest, of $E_{\mathrm{De,DS-I}} = 295\,\mathrm{GeV}$ is $F_{\mathrm{DS-I}} = (5.1 \pm 0.5_{\mathrm{stat}}) \times 10^{-11}\,\mathrm{ph\,cm^{-2}\,s^{-1}\ TeV^{-1}}$. The γ-ray spectrum of DS-II is best described by a power-law with index of $\Gamma_{\mathrm{DS-II}} = 3.5 \pm 0.2_{\mathrm{stat}}$ and norm $F_{\mathrm{DS-II}} = (3.2 \pm 0.3_{\mathrm{stat}}) \times 10^{-11}$ $\mathrm{ph\,cm^{-2}\ s^{-1}\,TeV^{-1}}$ at a decorrelation energy of $E_{\mathrm{De,DS-II}} = 360\,\mathrm{GeV}$. Table 4.11 lists the best-fit results.

To test for flux variability and analyse the temporal evolution of a source the light curve is computed. The temporal binning is chosen, e.g. nights, and the integrated flux per time bin is calculated. For the calculation of the light curve a spectral shape has

Data Set	Phase	σ	E_{Th} [TeV]	Power Law Index $\Gamma \pm \sigma_{Stat}$	E_{De} [TeV]	$\Phi(> E_{Th})$ $[10^{-11}\,cm^{-2}\,s^{-1}]$
I, monoscopic	0.78 - 0.96	8.9	0.193	3.9 ± 0.4	0.295	1.76 ± 0.19
I, stereoscopic	0.78 - 0.96	7.2	0.221	2.8 ± 0.2	0.484	0.80 ± 0.09
II, monoscopic	0.96 - 1.10	10.3	0.221	3.5 ± 0.2	0.360	1.56 ± 0.13
I + II, monoscopic	0.78 - 1.10	13.6	0.190	3.6 ± 0.2	0.333	1.99 ± 0.15

Table 4.11: Spectral statistics of the analyses: significance of the excess σ (following eqn. 3.14 and 3.15), threshold energy E_{Th}, decorrelation energy E_{De} and flux above the energy threshold $\Phi(> E_{Th})$.

to be assumed, in the case of η Carinae a simple power-law is chosen. Similar to the procedure described in section 3.6, a likelihood maximisation is performed in every bin with the flux normalisation ϕ_0 left free (other parameters like the spectral index are fixed at their mean value).

Fig. 4.27 shows the H.E.S.S. γ-ray light curve of the mono analysis of DS-I and DS-II. All spectral points with a statistical significance of more than $2\,\sigma$ are displayed as points. Upper limits at 95% confidence level are shown for non-significant flux measurements. The nightly and monthly H.E.S.S. light curve is within statistical and systematic uncertainties consistent with no variability. This is in agreement with the $Fermi-$LAT high-energy light curve that is, however, rather limited in the statistics and can only probe the γ-ray emission on much longer timescales. Due to the 5.54 yr orbital period of η Carinae, the source was not visible during periastron passage, which is why the time of the X-ray minimum is not covered by H.E.S.S. observations (c.f. fig. 4.27). Figure 4.26 shows how the spectra obtained in this work and the cross-check analyses compare. They are compatible within systematic errors, if again assuming an error of 20 % on the flux level. In the following the H.E.S.S. result and its implications for particle acceleration and γ-ray emission processes will be discussed in the multiwavelength context.

4.3.8 Discussion and interpretation

A VHE γ-ray source, coincident with η Carinae, was detected in observations with H.E.S.S.. The emission is consistent with being point-like taking into account the broadened PSF in this high NSB region as discussed in section 4.3.4. The H.E.S.S. source is spatially coincident with the $Fermi-$LAT η Carinae source, and the H.E.S.S. γ-ray spectrum smoothly connects at $\sim$180 GeV to the high-energy component of the $Fermi-$LAT spectrum (see Fig. 4.25). Based on these findings, an association of the

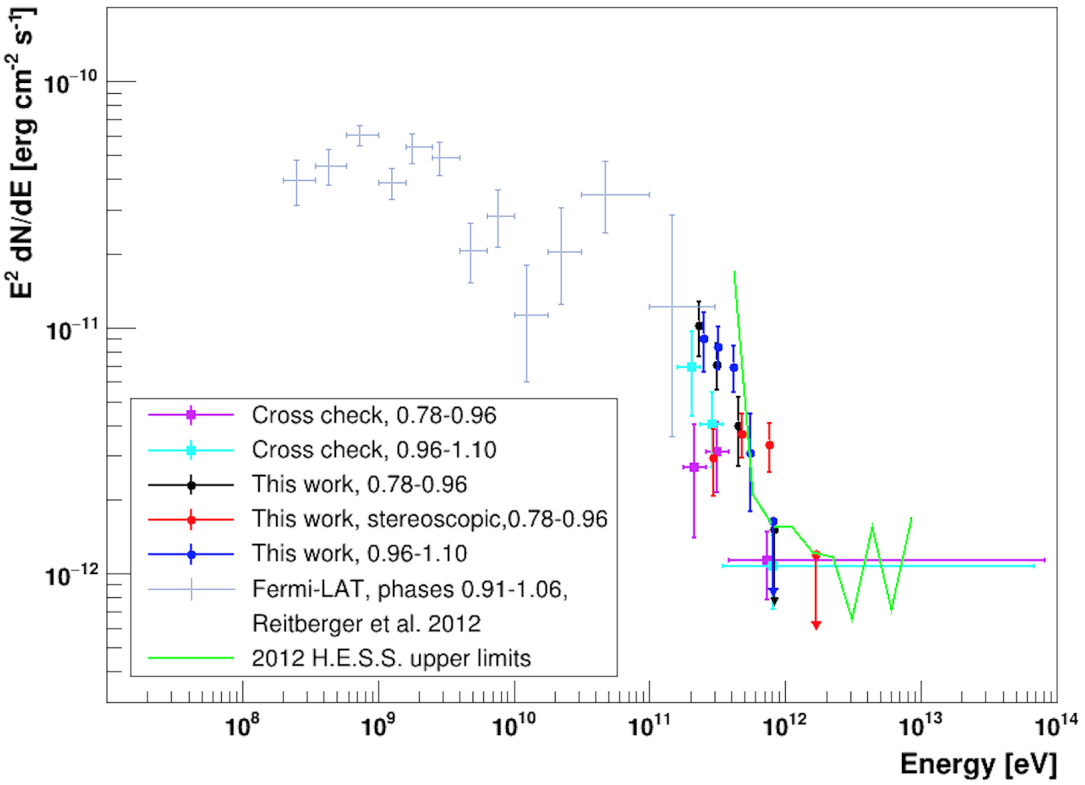

Figure 4.26: Comparison of the spectral points of this work and the cross-check analysis. All spectral points are deduced from monoscopic analyses, unless otherwise stated. The orbital phases are stated in the legend, DS-I corresponds to 0.78-0.96 and DS-II to 0.96-1.10. Additionally are shown: the stereo analysis of DS-I, the upper limits publishes by H.E.S.S. in 2012 [94] and the high-energy component observed by *Fermi*−LAT [90].

γ-ray emission seen by H.E.S.S. to the η Carinae colliding-wind-binary system seems plausible.

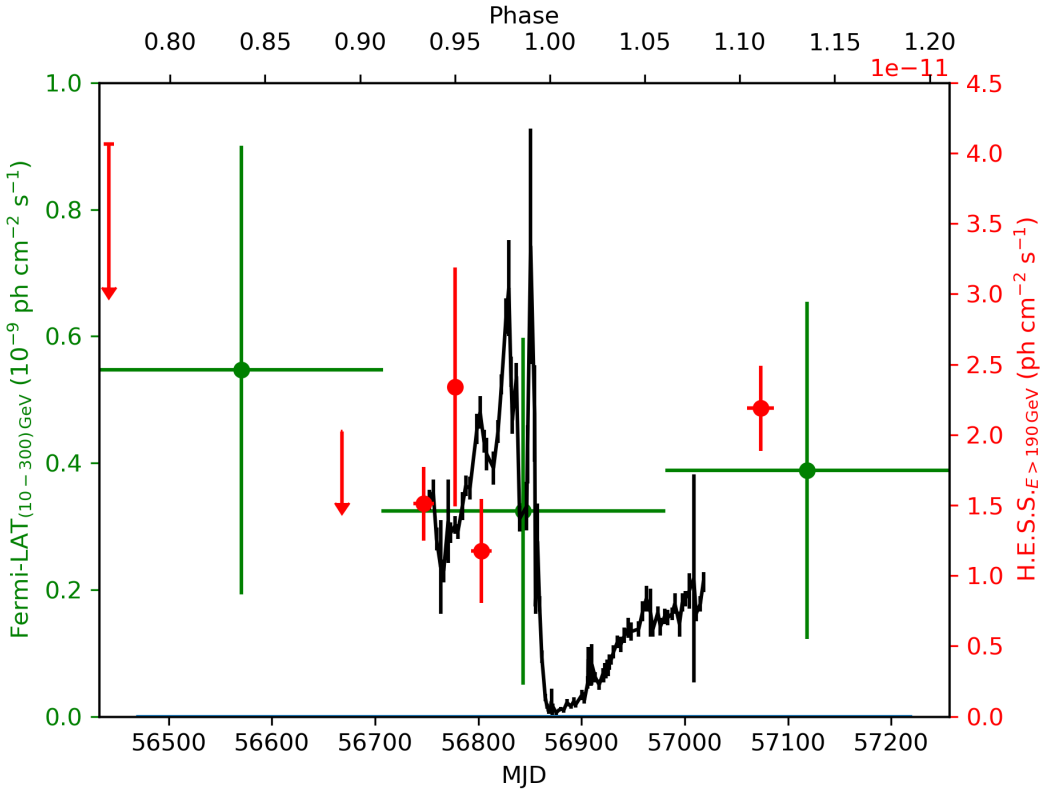

Figure 4.27: Phase-binned flux above 200 GeV as measured by H.E.S.S. in the mono analysis of DS-I and DS-II, red, *Fermi*−LAT flux points [93] and X-ray data by Swift [76].

The best-fit power-law model of the spectral energy distribution has a significantly steeper power-law index than in the *Fermi*−LAT domain. This is consistent with the upper limits reported by the H.E.S.S. collaboration in 2012 [94], based on data acquired using the H.E.S.S.-I system with a significantly higher energy threshold. The fact that the *Fermi*−LAT and H.E.S.S. spectra smoothly connect supports the idea that the same underlying parent particle population produces the γ-ray emission. The H.E.S.S. spectrum contains information about the maximum energy that the radiating particles in η Carinae can achieve, independent of the origin of the emission. The last significant bin in the γ-ray spectrum with $>2\sigma$ starts at 700 GeV in DS-II.

Since the measured emission is compatible with a constant flux, the following discussion is based on the reconstructed spectrum of DS-I and DS-II mono. The integral γ-ray energy flux above the 190 GeV energy threshold in DS-I and DS-II is $5.09 \times 10^{-11}\,\mathrm{erg\,cm^{-2}\,s^{-1}}$ or a luminosity of $L_\gamma = 3.22 \times 10^{34}\,\mathrm{erg\,s^{-1}}$ at a distance of

2.3 kpc to η Carinae. This corresponds to 1% (6%) of the total kinetic wind energy of the companion (primary) star available in the CWR [106]. The solid angle occupied by the CWR is only 1 (6) steradian on the primary (companion) side.

Particles can likely be accelerated to non-thermal energies in two regions in η Carinae, in the shocks on the primary and companion side of the system [102, 106]. Assuming that diffusive shock acceleration is at work in the Bohm limit ($\eta = 1$), the time to accelerate a charged particle to an energy E_{TeV} in a magnetic field B_G and in a shock with speed $v_{\mathrm{sh},10^3\,\mathrm{km\,s^{-1}}}$ can be written as [106]:

$$\tau_{\mathrm{acc}} = 5 \times 10^4\, s\, v^{-2}_{\mathrm{sh},10^3\,\mathrm{km\,s^{-1}}}\, \frac{E_{\mathrm{TeV}}}{B_G}\,. \tag{4.1}$$

In the most optimistic case one can assume that particle acceleration proceeds in the shock region on the companion side, and that the wind speed equals the shock speed: $v_{\mathrm{w}} = v_{\mathrm{sh}} = 3000\,\mathrm{km\,s^{-1}}$.

If the accelerated particles are electrons, inverse Compton scattering would take place in the Klein-Nishina regime from ∼30 GeV onward [100]. Both stars in η Carinae provide optical lower-energy photons for this process. The maximum electron energy in the Klein-Nishina regime would be ∼700 GeV. At energies of hundreds of GeV, electrons will predominantly suffer synchrotron losses with a characteristic cooling time of:

$$\tau_{\mathrm{cool}} = 4 \times 10^2\, s\, E^{-1}_{\mathrm{TeV}}\, B_G^{-2}\,. \tag{4.2}$$

For electrons to reach an energy of 700 GeV in the synchrotron-loss limited acceleration case (where $\tau_{\mathrm{acc}} = \tau_{\mathrm{cool}}$), the maximum allowed magnetic field is estimated to be ∼0.2 G. This magnetic field strength would imply an acceleration time of $\tau_{\mathrm{acc}} = 5.4$ hours, much shorter than the typical flow time of particles and gas out of the system at any phase [cf. 106]. Particle acceleration in this case is exacerbated by the cooling time scale of ~ 4 h, see fig. 4.28.

In a hadronic scenario, protons and heavier nuclei would have to be accelerated to at least 7 TeV [100]. Assuming the same magnetic field strength and Bohm diffusion as in the leptonic case, the acceleration time for protons is 2.25 days. The cooling time depends on the density of hydrogen nuclei n: $\tau_{\mathrm{cool,p}} \approx 3.0 \times 10^7\, n^{-1}\,\mathrm{yr}$ [100]. The density strongly depends on the orbital phase and differs in the shocks on companion

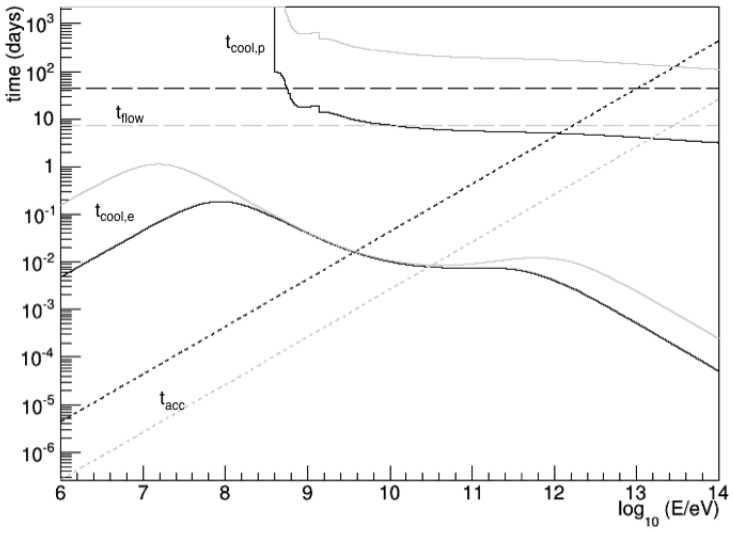

Figure 4.28: Timescales important for particle acceleration in η Carinae as a function of energy assuming Bohm limit: in black the primary, in grey the companion star. A surface magnetic field of $B_s = 100\,\mathrm{G}$ with a toroidal form is used following Eichler and Usov, 1993 [8]. Credit: R. Konno, S. Ohm and J. Hinton

and primary side. Ohm et al. adopt values of $n_{Prim} \approx 10^8\,\mathrm{cm}^{-3}$ and $n_{Com} \approx 10^7\,\mathrm{cm}^{-3}$ at phase $p \approx 0.05$ [106]. Farnier et al. assume only one shock region with a density of hydrogen nuclei $n \approx 3 \times 10^9\,\mathrm{cm}^{-3}$ [33]. Applying these densities leads to cooling times between $\sim 4\,\mathrm{d}$ ($n = 3 \times 10^9\,\mathrm{cm}^{-3}$), $\sim 110\,\mathrm{d}$ ($n = 10^8\,\mathrm{cm}^{-3}$, primary side) and $3\,\mathrm{yr}$ ($n = 10^7\,\mathrm{cm}^{-3}$, companion side). If not assuming a magnetic field strength an estimation of B_p can again be drawn from $\tau_{\mathrm{acc}} = \tau_{\mathrm{cool}}$. For the above mentioned densities of Ohm et al. the magnetic field density can be approximated to $B_{Prim} = 0.1\,\mathrm{G}$ and $B_{Com} = 3 \times 10^{-4}\,\mathrm{G}$.

While the 100 MeV - 10 GeV emission detected by $Fermi-$LAT is interpreted in a leptonic [33, 92, 93] and a hadronic scenario [106], there seems to be a broad consensus that the $\geq$10 GeV emission can best be explained as stemming from interacting protons [33, 102, 106, 92, 93]. The new H.E.S.S. measurement and extension of the spectrum to hundreds of GeV energies is consistent with this hadronic interpretation.

The emission observed in a distance of $\sim 0.26\,^\circ$ from η Carinae (HOTS J1044-5957) is of unknown origin. It is located in direct neighbourhood to the open stellar cluster Collinder 228 (generally considered to be part of Tr 16, only appearing separated be-

cause of an obscuring dust lane [e.g. 41]). Two interesting objects in Collinder 228 are HD 93131 and HD 93206, both driving fast winds. Particles could be accelerated in the wind of a single massive star and/or the collective effect of the stellar winds could lead to particle acceleration via second order Fermi acceleration [e.g. 154]. The correlation of HOTS J1044-5957 with the strongest NSB in the region and the non-detection in the stereo analysis suggests a contribution of the NSB to the emission. However, an in-depth investigation lies beyond the scope of this thesis.

In Figure 4.25 the high-energy end of the gamma-ray spectrum shows a strong turnover around $\sim$100 GeV. The feature could be indicative of i) the maximum energy radiating particles are accelerated to, or ii) significant gamma-gamma absorption of VHE photons in the strong stellar radiation fields, or iii) a mix of both. One could potentially differentiate between the two scenarios, by accurately measuring the shape of the cutoff feature. Given the available H.E.S.S. data and associated spectral uncertainties, it is not possible to distinguish between the options here.

H.E.S.S. observed η Carinae shortly before the thermal X-ray maximum at phase $p \sim 0.9$ and after the subsequent X-ray minimum and recovery of the CWR at phase $p \sim 1.1$. The flux H.E.S.S. observed shows no indication of variability on monthly or intra-night timescales. The lack of strong variability in the H.E.S.S. lightcurve is broadly consistent with the behaviour in hard X-rays [85] and GeV gamma rays [e.g. 93].

η Carinae was not visible for H.E.S.S. during night time at the time of the periastron passage, which is why this data set can not be used to constrain particle acceleration and gamma-ray emission during the time of the X-ray minimum and presumed collapse of the CWR. This also means that the question of the origin of the observed emission from inside or outside the CWR can not be answered with the measurement presented here.

Chapter 5

Conclusion and Outlook

For the first time, VHE γ-ray emission from a colliding wind binary has been observed. This H.E.S.S. measurement was made possible by the in-depth investigation of the impact of the NSB presented in this thesis.

The first step towards the detection of η Carinae was the application of a Hillas-parametrisation based reconstruction to the data set in chapter 4.2.3. For the application, a new shower image cleaning level has been introduced and different cuts have been studied, in order to reach excess statistics comparable with the standard candle of γ-ray astronomy the Crab nebula. An excess of γ-ray emission in the combined data set of DS-I and DS-II towards η Carinae is reported with $8.2\,\sigma$. The emission is not consistent with the PSF of H.E.S.S. which points to contributions by systematic effects, probably related to the NSB level. The impact of turned-off pixels in the camera and the correct NSB (in contrast to a fixed level of NSB) has been studied in run-wise simulations using more detailed realistic observation conditions. The impact of turned-off pixels on excess events is approximated to be $\sim 8\,\%$. The impact of simulating the correct NSB level on excess events is $\sim$ 30 %, the overall impact of realistic NSB and pixel conditions on excess events is $\sim$37%. It has to be noted though, that the simulations do not account for hadronic background. There is an expected contribution from hadronic background that passes the second trigger level with help of NSB photons. The broadening of the PSF observed in data is not reproduced in the run-wise simulations for the Hillas reconstruction based analysis.

The size s, width w and length l of the shower ellipse reconstructed with the Hillas technique are used as seeds for the Model Analysis fit and the results presented in

section 4.3 and following. The introduced increased shower image cleaning leads to improved results in shower reconstruction in the Model Analysis in $\sim 90\,\%$ of reconstructed shower images. Low-level distributions were investigated in section 4.3.2 to monitor the influence of the NSB and ensure the quality of the analysis. The data set is analysed in monoscopic and stereoscopic fashion. Excess γ-ray emission towards η Carinae is found in all analyses with $\geq 7\,\sigma$ in section 4.3.4. With run-wise simulations the impact of the assumed spectral index of the VHE γ-ray emission is studied and it is found that a very soft index of $\sim 3.7 - 4.0$ is consistent with the γ-ray spectral index as reconstructed using classical IRFs. With the assumption of a spectral energy distribution that follows a power law with index $\Gamma \geq 3.7$, η Carinae is consistent with being point-like within the H.E.S.S. PSF.

Sky excess maps show indication for a new source $\sim 0.29\,^\circ$ southwest of η Carinae. Dedicated analyses of this hot spot (HOTS J1044-5957), using monoscopic and stereoscopic reconstruction methods, yield $\sim 8.2\,\sigma$ and $\sim 4.6\,\sigma$, respectively. Its impact on η Carinae's excess emission is estimated to be $\sim 16\,\%$. The position of HOTS J1044-5957 coincides with the region of highest NSB in the FoV and a contribution of the NSB to the excess cannot be excluded. A potential contribution of close-by $Fermi-$LAT source 3FGL J1043.6-5930 to the excess at η Carinae's position is negligible ($\sim 3\,\%$).

Extensive tests demonstrate that the impact of the NSB on η Carinae is well understood. The spatial extension of the NSB and its potential correlation with the γ-ray excess is evaluated in section 4.3.6. The structure of the high NSB region is highly inhomogeneous and extends over $\geq 0.3\,^\circ$. The maximum NSB coincides with HOTS J1044-5957. η Carinae is located right next to an elongated structure of NSB tracing levels above 500 MHz and still within a region with more than 300 MHz NSB. The γ-ray excess significance contours do not trace the NSB emission, as it would be expected for a NSB-dominated excess. The impact of patterns of turned-off pixels on the excess is studied in profile plots of excess maps. Hereby, the maximum contribution of NSB per excess event and given level of NSB is estimated.

In section 4.3.7 the spectral energy distribution of the γ-ray emission observed with H.E.S.S. is presented. Spectra before and after the periastron passage agree within statistic uncertainties. The spectra follow a power-law with a soft index and are steeply falling towards 1 TeV. At the energy threshold of ~ 200 GeV the H.E.S.S. and $Fermi-$LAT spectra connect smoothly, suggesting a common parent particle popula-

tion. Hadronic and leptonic particles are considered. With the maximum γ-ray energy contained in the spectrum of η Carinae acceleration and cooling times of protons and electrons are calculated, as well as an estimate of the magnetic field. In agreement with the explanation of the HE γ-ray component observed by $Fermi-$LAT the hadronic description of η Carinae's VHE γ-ray emission is more plausible. Electrons suffer severe cooling losses, making it hard to reach energies as high as necessary to explain the observed γ-ray energies.

The H.E.S.S. light curve of η Carinae spans from phase 0.78 to 1.10. No variability in the flux level is observed. Unfortunately, η Carinae was not observable shortly after or during the x-ray minimum at periastron. Thus, the question of the (spatial) origin of the γ-ray emission has to be left for future observations and analyses.

H.E.S.S. has been continuing observations on η Carinae since 2015. These observations cover the apastron, where $Fermi-$LAT detected minimum HE γ-ray emission. Analysing these observations as well as data covering other orbital phases will hopefully improve our understanding, e.g. of the (spatial) origin of the emission: variability along the orbit indicates an origin within the CWR. If $Fermi-$LAT and H.E.S.S. observe emission from the same parent particles and the same process of π^0 decay it is expected that the HE component in $Fermi-$LAT and the emission observed with H.E.S.S. behave in a similar way. This can be checked with the data already taken by H.E.S.S.. The next periastron passage of η Carinae will take place at the end of 2019/ beginning 2020. H.E.S.S. can continue to play a crucial role in the investigation of η Carinae's non-thermal emission because it will be the only IACT able to observe the next periastron passage if its operation will be prolonged beyond 2019 and before the onset of the *Cherenkov Telescope Array* [155, 95]. For future observations testing the x-ray minimum at periastron is of great interest. The assumed collapse of the CWR would lead to a (delayed - in comparison to x-rays) minimum in γ-ray emission, if it only originates from the CWR.

Besides η Carinae, other promising CWB exist which are in reach of H.E.S.S. An obvious candidate is γ^2 Velorum (WR 11), the closest CWB at a distance of $\sim$ 340 pc [156]. The bright binary is composed of a Wolf-Rayet star and an O-type companion star and can be observed by naked eye in the Southern hemisphere. In 2016, a weak ($6.1\,\sigma$) signal of γ-ray emission was reported to be found in 7 years of $Fermi-$LAT data [39]. Although magneto-hydrodynamic modeling does not support an additional

component in the HE - VHE regime [157], the energy spectrum in [39] does not show a cut off and there is no further observational data on γ^2 Velorum in this energy regime. Future H.E.S.S. or CTA observations will be able to answer if the exceptional CWB η Carinae will remain truly exceptional.

List of Figures

List of Tables

Danksagung

Ich möchte mich bedanken bei

- Kathrin und Christian für die Möglichkeit zur Promotion und die vielen Reisen zu Konferenzen und Sommerschulen
- Christian für die Unterstützung und das entgegengebrachte Vertrauen
- Stefan O. for making science great again
- der H.E.S.S. Arbeitsgruppe DESY/ Uni Potsdam, auch der früheren: besonders Anneli, Stefan K. und Matthias und der aktuellen sowieso, für die angenehme Arbeitsatmosphäre und den Austausch, bei dem ich am meisten gelernt habe. Bei Heike, Jhinlik, Iryna und Maria. Bei Markus für die Hilfe mit der Model Analyse.

Dem Mo. Lisa. Meinen wunderbaren MitbewohnerInnen: Zuppi, Hannes, Vanessa, Elena, Lise, Fuchsi und dem Vogeljungen. Dem Eismann.

Bibliography

[1] G. W. F. Hegel. *Phänomenologie des Geistes*, volume 1. Suhrkamp, 1986.

[2] G. W. F. Hegel. *The Phenomenology of Mind*. Harper Torchbooks, 1967.

[3] J. Vink. Shocks and particle acceleration in supernova remnants: observational features. *Advances in Space Research*, 33(4):356 – 365, 2004. ISSN 0273-1177.

[4] D. C. Ellison, D. J. Patnaude, P. Slane, P. Blasi, and S. Gabici. Particle Acceleration in Supernova Remnants and the Production of Thermal and Nonthermal Radiation. *ApJ*, 661(2):879, 2007.

[5] G. Dubus. Gamma-ray binaries and related systems. *Astronomy and Astrophysics Review*, 21:64, August 2013.

[6] G. Dubus. Gamma-ray emission from binaries in context. *Comptes Rendus Physique*, 16(661), 2015.

[7] V. Bosch-Ramon. Theoretical overview on high-energy emission in microquasars. *Astrophysics and Space Science*, 309:321–331, June 2007.

[8] D. Eichler and V. Usov. Particle acceleration and nonthermal radio emission in binaries of early-type stars. *ApJ*, 402:271–279, 1993.

[9] A. Abramowski and H.E.S.S. Collaboration. Discovery of extended VHE γ-ray emission from the vicinity of the young massive stellar cluster Westerlund 1. *Astronomy and Astrophysics*, 537:A114, January 2012.

[10] *Nobel Lectures, Physics 1942-1962*. Elsevier Publishing Company, 1964.

[11] E. Halley. *Catalogus stellarum australium*. Typis, T. J., Londini, 1679. URL `//catalog.hathitrust.org/Record/001983785`.

[12] E. Dekker. Early explorations of the southern celestial sky. *Annals of Science*, 44: 439–470, 1987.

[13] D. J. Frew. The Historical Record of η Carinae I. The Visual Light Curve, 1595-2000. *Journal of Astronomical Data*, 10, December 2004.

[14] J. Needham. Astronomy in ancient and medieval china. *Philosophical Transactions of the Royal Society of London. Series A, Mathematical and Physical Sciences*, 276 (1257):67, 1974.

[15] Sir. J. F. W. Herschel. *Results of astronomical observations made during the years 1834, 5, 6, 7, 8, at the Cape of Good Hope*. Smith, Elder and Co., 1847.

[16] W. E. Stanbridge. On the astronomy and mythology of the Aborigines of Victoria. *Transactions Philosophical Institute Victoria*, 2:137–140, 1858.

[17] D. W. Hamacher and D. J. Frew. An Aboriginal Australian Record of the Great Eruption of Eta Carinae. *Journal of Astronomical History and Heritage*, 13:220–234, November 2010.

[18] T. Hockey, editor. *The Biographical Encyclopedia of Astronomers*. Springer-Verlag New York, 1st edition, 2007.

[19] N. Smith, R. D. Gehrz, P. M. Hinz, W. F. Hoffmann, J. L. Hora, E. E. Mamajek, and M. R. Meyer. Mass and kinetic energy of the Homunculus Nebula around η Carinae. *The Astronomical Journal*, 125:1458–1466, March 2003.

[20] S. D. Van Dyk and T. Matheson. The supernova impostors. In K. Davidson and R. M. Humphreys, editors, *Eta Carinae and the Supernova Impostors*, volume 384 of *Astrophysics and Space Science Library*, pages 249–274. Springer-Verlag New York, 2012.

[21] K. Ishibashi, T. R. Gull, K. Davidson, et al. Discovery of a Little Homunculus within the Homunculus Nebula of η Carinae. *The Astronomical Journal*, 125(6): 3222, 2003.

[22] N. Smith. A blast wave from the 1843 eruption of η Carinae. *Nature*, 455(201), 2008.

[23] A. Damineli. The 5.52 Year Cycle of Eta Carinae. *ApJ*, 460:49, March 1996.

[24] K. Davidson and R. M. Humphreys. ETA CARINAE AND ITS ENVIRONMENT. *Annual Review of Astronomy and Astrophysics*, 35(1):1–32, 1997.

[25] A. M. van Genderen, M. J. H. de Groot, and P. S. Thé. The optical and near infrared variability of Eta Carinae: A binary luminous blue variable? *Astronomy and Astrophysics*, 283:89–110, March 1994.

[26] A. Damineli, P. S. Conti, and D. F. Lopes. Eta Carinae: a long period binary? *New Astronomy*, 2(2):107 – 117, 1997. ISSN 1384-1076.

[27] J. M. Pittard and M. F. Corcoran. In hot pursuit of the hidden companion of η Carinae: An X-ray determination of the wind parameters. *Astronomy and Astrophysics*, 383:636–647, February 2002.

[28] D. J. Hillier, K. Davidson, K. Ishibashi, and T. Gull. On the Nature of the Central Source in η Carinae. *ApJ*, 553:837–860, June 2001.

[29] M. De Becker and F. Raucq. Catalogue of particle-accelerating colliding-wind binaries. *Astronomy and Astrophysics*, 558:A28, October 2013.

[30] A. E. Wright and M. J. Barlow. The radio and infrared spectrum of early-type stars undergoing mass loss. *MNRAS*, 170:41–51, January 1975.

[31] M. De Becker. Non-thermal emission processes in massive binaries. *The Astronomy and Astrophysics Review*, 14:171–216, November 2007.

[32] A. F. J. Moffat. Massive Binaries. In F. Bresolin, P. A. Crowther, and J. Puls, editors, *Massive Stars as Cosmic Engines*, volume 250 of *IAU Symposium*, pages 119–132, June 2008.

[33] C. Farnier, R. Walter, and J. C. Leyder. η Carinae: a very large hadron collider. *Astronomy and Astrophysics*, 526(A57), 2011.

[34] M. De Becker, P. Benaglia, G. E. Romero, and C. S. Peri. An investigation into the fraction of particle accelerators among colliding-wind binaries. Towards an extension of the catalogue. *Astronomy and Astrophysics*, 600:A47, April 2017.

[35] A. Reimer, M. Pohl, and O. Reimer. Non-thermal high-energy emission from colliding winds of massive stars. *ApJ*, 644(1118), 2006.

[36] A. Sekiguchi, M. Tsujimoto, S. Kitamoto, M. Ishida, K. Hamaguchi, H. Mori, and Y. Tsuboi. Super-hard X-Ray Emission from Eta Carinae observed with Suzaku. *PASJ*, 61(629), 2009.

[37] Y. Sugawara, Y. Maeda, Y. Tsuboi, K. Hamaguchi, M. Corcoran, A. Pollock, A. Moffat, P. Williams, S. Dougherty, and J. Pittard. The variable X-ray spectrum of the Wolf-Rayet binary WR140 with Suzaku. *Bulletin de la Societe Royale des Sciences de Liege*, 80:724–728, January 2011.

[38] Abdo, A. A. et al., Fermi-LAT collaboration. Fermi Large Area Telescope Observation of a Gamma-ray Source at the Position of Eta Carinae. *ApJ*, 723(649), 2010.

[39] M. S. Pshirkov. The Fermi-LAT view of the colliding wind binaries. *MNRAS*, 457:L99–L102, March 2016.

[40] S. V. Marchenko, A. F. J. Moffat, D. Ballereau, J. Chauville, J. Zorec, G. M. Hill, K. Annuk, L. J. Corral, H. Demers, P. R. J. Eenens, K. P. Panov, W. Seggewiss, J. R. Thomson, and A. Villar-Sbaffi. The Unusual 2001 Periastron Passage in the "Clockwork" Colliding-Wind Binary WR 140. *ApJ*, 596:1295–1304, October 2003.

[41] N. Smith and K. J. Brooks. *The Carina Nebula: A Laboratory for Feedback and Triggered Star Formation*, page 138. December 2008.

[42] N. Smith. A Census of the Carina Nebula. I: Cumulative Energy Input from Massive Stars. *MNRAS*, 367(763), 2006.

[43] T. Preibisch, S. Hodgkin, M Irwin, J. R. Lewis, R. R. King, M. J. McCaughrean, H. Zinnecker, L. K. Townsley, and P. S. Broos. Near-infrared Properties of the X-ray-emitting Young Stellar Objects in the Carina Nebula. *ApJS*, 194(1):10, 2011.

[44] A. W. Fullerton, D. L. Massa, and R. K. Prinja. The Discordance of Mass-Loss Estimates for Galactic O-Type Stars. *ApJ*, 637:1025–1039, February 2006.

[45] N. Smith and K. J. Brooks. A Census of the Carina Nebula. II: Energy Budget and Global Properties of the Nebulosity. *MNRAS*, 379(1279), 2007.

[46] D. A. Grabelsky, R. S. Cohen, L. Bronfman, and P. Thaddeus. Molecular clouds in the Carina arm - The largest objects, associated regions of star formation, and the Carina arm in the Galaxy. *ApJ*, 331:181–196, August 1988.

[47] N. Smith, K. G. Stassun, and J. Bally. Opening the Treasure Chest: A Newborn Star Cluster Emerges from Its Dust Pillar in Carina. *The Astronomical Journal*, 129:888–899, February 2005.

[48] M.S. Longair. *High Energy Astrophysics*. Cambridge University Press, 2011. ISBN 9781139494540.

[49] R. A. Duncan and S. M. White. Radio evidence of recent mass ejection from η Carinae. *MNRAS*, 338:425–427, January 2003.

[50] S. M. Dougherty, A. J. Beasley, M. J. Claussen, B. A. Zauderer, and N. J. Bolingbroke. High-Resolution Radio Observations of the Colliding-Wind Binary WR 140. *ApJ*, 623:447–459, April 2005.

[51] S. M. White, R. A. Duncan, J. M. Chapman, and B. Koribalski. The Radio Cycle of Eta Carinae. In R. Humphreys and K. Stanek, editors, *The Fate of the Most Massive Stars*, volume 332 of *Astronomical Society of the Pacific Conference Series*, page 129, September 2005.

[52] J. M. Chapman, C. Leitherer, B. Koribalski, R. Bouter, and M. Storey. Radio Continuum Measurements of Southern Early-Type Stars. III. Nonthermal Emission from Wolf-Rayet Stars. *ApJ*, 518:890–900, June 1999.

[53] G. Weigelt, K.-H. Hofmann, D. Schertl, et al. VLTI-AMBER velocity-resolved aperture-synthesis imaging of η Carinae with a spectral resolution of 12 000. Studies of the primary star wind and innermost wind-wind collision zone. *Astronomy and Astrophysics*, 594:A106, October 2016.

[54] P. W. Morris, T. R. Gull, D. J. Hillier, M. J. Barlow, P. Royer, K. Nielsen, J. Black, and B. Swinyard. η Carinae's Dusty Homunculus Nebula from Near-infrared to Submillimeter Wavelengths: Mass, Composition, and Evidence for Fading Opacity. *ApJ*, 842:79, June 2017.

[55] F. Hamann and HST–Eta Carinae Treasury Team. HST Spectroscopy of Eta Car's Inner Ejecta. In R. Humphreys and K. Stanek, editors, *The Fate of the Most Massive Stars*, volume 332 of *Astronomical Society of the Pacific Conference Series*, page 287, September 2005.

[56] E. Fernández-Lajús, C. Fariña, J.P. Calderón, et al. The η Carinae optical 2009.0 event, a new "eclipse-like" phenomenon. *New Astronomy*, 15(1):108 – 112, 2010. ISSN 1384-1076.

[57] E. Fernández-Lajús, C. Fariña, A. F. Torres, et al. Long-term optical monitoring of η Carinae. Multiband light curves for a complete orbital period. *Astronomy and Astrophysics*, 493:1093–1097, January 2009.

[58] M. Teodoro, A. Damineli, B. Heathcote, et al. He II λ4686 Emission from the Massive Binary System in η Car: Constraints to the Orbital Elements and the Nature of the Periodic Minima. *ApJ*, 819:131, March 2016.

[59] J. C. Martin, Kris Davidson, and M. D. Koppelman. The Chrysalis Opens? Photometry from the η Carinae Hubble Space Telescope Treasury Project, 2002-2006. *The Astronomical Journal*, 132(6):2717, 2006.

[60] K. Davidson, D. Ebbets, S. Johansson, J. A. Morse, F. W. Hamann, B. Balick, R. M. Humphreys, G. Weigelt, and A. Frank. HST/GHRS Observations of the Compact Slow Ejecta of Eta Carinae. *The Astronomical Journal*, 113:335–345, January 1997.

[61] G. Weigelt and J. Ebersberger. Eta Carinae resolved by speckle interferometry. *Astronomy and Astrophysics*, 163:L5, July 1986.

[62] K. Davidson, D. Ebbets, G. Weigelt, R. M. Humphreys, A. R. Hajian, N. R. Walborn, and M. Rosa. HST/FOS spectroscopy of η Carinae: the star itself, and ejecta within 0.3 arcsec. *The Astronomical Journal*, 109:1784–1796, April 1995.

[63] A. Mehner, K. Davidson, G. J. Ferland, and R. M. Humphreys. High-excitation Emission Lines near Eta Carinae, and Its Likely Companion Star. *ApJ*, 710: 729–742, February 2010.

[64] J. A. Morse, K. Davidson, J. Bally, D. Ebbets, B. Balick, and A. Frank. Hubble Space Telescope Wide Field Planetary Camera 2 Observations of η Carinae. *The Astronomical Journal*, 116(5):2443, 1998.

[65] J. H. Groh, D. J. Hillier, T. I. Madura, and G. Weigelt. On the influence of the companion star in Eta Carinae: 2D radiative transfer modelling of the ultraviolet and optical spectra. *MNRAS*, 423:1623–1640, June 2012.

[66] N. D. Richardson, H. Pablo, C. Sterken, et al. BRITE-Constellation reveals evidence for pulsations in the enigmatic binary η Carinae. *MNRAS*, page sty157, 2018.

[67] O. F. Prilutskii and V. V. Usov. X rays from Wolf-Rayet binaries. *Soviet Astronomy*, 20:2, February 1976.

[68] A. M. Cherepashchuk. Detectability of Wolf-Rayet binaries from X rays. *Soviet Astronomy Letters*, 2:138, August 1976.

[69] A. N. Bunner. Soft X-ray results from the Wisconsin experiment on OSO-8. *ApJ*, 220:261–271, February 1978.

[70] W. Forman, C. Jones, L. Cominsky, P. Julien, S. Murray, G. Peters, H. Tananbaum, and R. Giacconi. The fourth Uhuru catalog of X-ray sources. *ApJ*, 38: 357–412, December 1978.

[71] M. F. Corcoran, G. L. Rawley, J. H. Swank, and R. Petre. First detection of x-ray variability of Eta Carinae. *ApJ*, 445:L121–L124, June 1995.

[72] K. Ishibashi, M. F. Corcoran, K. Davidson, J. H. Swank, R. Petre, S. A. Drake, A. Damineli, and S. White. Recurrent X-Ray Emission Variations of η Carinae and the Binary Hypothesis. *ApJ*, 524:983–987, October 1999.

[73] T. Chlebowski, F. D. Seward, J. Swank, and A. Szymkowiak. X-rays from Eta Carinae. *ApJ*, 281:665–672, June 1984.

[74] M. F. Corcoran. X-Ray Monitoring of η Carinae: Variations on a Theme. *The Astronomical Journal*, 129(4):2018, 2005.

[75] M. F. Corcoran, K. Hamaguchi, J. K. Liburd, et al. The X-ray Lightcurve of the Supermassive star eta Carinae, 1996–2014. *ArXiv e-prints*, July 2015.

[76] M. F. Corcoran, J. Liburd, D. Morris, et al. The 2014 X-Ray Minimum of η Carinae as Seen by Swift. *ApJ*, 838:45, March 2017.

[77] R. F. Viotti, L. A. Antonelli, M. F. Corcoran, A. Damineli, P. Grandi, J. M. Muller, S. Rebecchi, C. Rossi, and M. Villada. BeppoSAX broad X-ray range observations of Eta Carinae during high and low spectroscopic states. *Astronomy and Astrophysics*, 385:874–883, April 2002.

[78] R. F. Viotti, L. A. Antonelli, S. Rebecchi, and C. Rossi. High Energy Phenomena in Eta Carinae. *Journal of Astrophysics and Astronomy*, 23(1):19–22, March 2002. ISSN 0973-7758.

[79] R. F. Viotti, L. A. Antonelli, C. Rossi, and S. Rebecchi. The high energy X-ray tail of η Car revealed by BeppoSAX. *Astronomy and Astrophysics*, 420:527–532, June 2004.

[80] J.-C. Leyder, R. Walter, and G. Rauw. Hard X-ray emission from η Carinae. *Astronomy and Astrophysics*, 477:L29–L32, January 2008. doi: 10.1051/0004-6361: 20078981.

[81] F. Jansen, D. Lumb, B. Altieri, et al. XMM-Newton observatory. I. The spacecraft and operations. *Astronomy and Astrophysics*, 365:L1–L6, January 2001.

[82] F. A. Harrison, W. W. Craig, F. E. Christensen, et al. The Nuclear Spectroscopic Telescope Array (NuSTAR) High-energy X-Ray Mission. *ApJ*, 770:103, June 2013.

[83] K. Hamaguchi and et al. Eta Carinae's Thermal X-ray Tail Measured with XMM-Newton and NuSTAR. *ApJ*, 817(23), 2016.

[84] K. Hamaguchi, M. F. Corcoran, and η Car Team. Extremely Hard X-ray Emission from η Car Observed with XMM-Newton and NuSTAR around Periastron in 2014.6. In W.-R. Hamann, A. Sander, and H. Todt, editors, *Wolf-Rayet Stars: Proceedings of an International Workshop held in Potsdam, Germany, 1-5 June 2015, Universitätsverlag Potsdam*, pages 159–162, 2015.

[85] K. Hamaguchi, M. F. Corcoran, J. M. Pittard, et al. Non-thermal X-rays from colliding wind shock acceleration in the massive binary Eta Carinae. *Nature Astronomy*, 2018.

[86] M. Tavani et al. (AGILE collaboration). Detection of Gamma-ray Emission from the Eta-Carinae region. *ApJ Letters*, 698(L142), 2009.

[87] M. Tavani et al. (AGILE collaboration). The AGILE Mission. *Astronomy and Astrophysics*, 502:995–1013, August 2009.

[88] Abdo, A. A. et al., Fermi-LAT collaboration. Fermi Large Area Telescope Bright Gamma-ray Source List. *ApJS*, 183(46), 2009.

[89] Abdo, A. A. et al., Fermi-LAT collaboration. The large area telescope on the fermi gamma-ray space telescope mission. *ApJ*, 697(2):1071, 2009.

[90] K. Reitberger, O. Reimer, A. Reimer, M. Werner, K. Egberts, and H. Takahashi. Gamma-ray follow-up studies on η Carinae. *Astronomy and Astrophysics*, 544: A98, August 2012.

[91] S. Ohm, J. A. Hinton, and W. Domainko. Particle Acceleration in the Expanding Blast Wave of η Carina's Great Eruption of 1843. *The Astronomical Journal Letters*, 718:L161–L165, August 2010.

[92] K. Reitberger, A. Reimer, O. Reimer, and H. Takahashi. The first full orbit of Eta Carinae seen by Fermi. *Astronomy and Astrophysics*, 577(100), May 2015.

[93] M. Balbo and R. Walter. Fermi acceleration along the orbit of η Carinae. *Astronomy and Astrophysics*, 603:A111, July 2017.

[94] H.E.S.S. Collaboration. H.E.S.S. observations of the Carina nebula and its enigmatic colliding wind binary Eta Carinae. *MNRAS*, 424:128–135, July 2012.

[95] S. Funk, J. A. Hinton, and CTA Consortium. Comparison of Fermi-LAT and CTA in the region between 10-100 GeV. *Astroparticle Physics*, 43:348–355, March 2013.

[96] E. Fermi. On the Origin of the Cosmic Radiation. *Physical Review*, 75:1169–1174, April 1949.

[97] A. R. Bell. The acceleration of cosmic rays in shock fronts – I. *MNRAS*, 182(2): 147–156, 1978.

[98] L. O. Drury. An introduction to the theory of diffusive shock acceleration of energetic particles in tenuous plasmas. *Reports on Progress in Physics*, 46:973–1027, August 1983.

[99] A. R. Bell. Cosmic ray acceleration. *Astroparticle Physics*, 43:56–70, March 2013.

[100] J. Hinton and W Hofmann. *Teraelectronvolt Astronomy*, volume 47. Annual Reviews, 06 2010.

[101] R. Walder, D. Folini, and G. Meynet. Magnetic Fields in Massive Stars, Their Winds, and Their Nebulae. *Space Science Reviews*, 166:145–185, May 2012.

[102] W. Bednarek and J. Pabich. High-energy radiation from the massive binary system Eta Carinae. *Astronomy and Astrophysics*, 530:A49, June 2011.

[103] V. L. Ginzburg and S. I. Syrovatskii. Cosmic magnetobremsstrahlung (synchrotron radiation). *Annual Review of Astronomy and Astrophysics*, 3(1):297–350, 1965.

[104] V. L. Ginzburg and S. I. Syrovatskii. Origin of cosmic rays. *Soviet Physics Uspekhi*, 9(2):223, 1966.

[105] P. Benaglia and G. E. Romero. Gamma-ray emission from Wolf-Rayet binaries. *Astronomy and Astrophysics*, 399:1121–1134, March 2003.

[106] S. Ohm, V. Zabalza, J. A. Hinton, and E. R. Parkin. On the origin of γ-ray emission in η Carina. *MNRAS*, 449:L132–L136, April 2015.

[107] M. de Naurois and L. Rolland. A high performance likelihood reconstruction of γ-rays for imaging atmospheric Cherenkov telescopes. *Astroparticle Physics*, 32: 231–252, December 2009.

[108] P. A. Cherenkov. Visible emission of clean liquids by action of γ radiation. *Doklady Akademii Nauk SSSR*, 2:451+, 1934.

[109] J. Holder. Atmospheric Cherenkov Gamma-ray Telescopes. *ArXiv e-prints*, October 2015.

[110] R. Engel, D. Heck, and T. Pierog. Extensive air showers and hadronic interactions at high energy. *Annual Review of Nuclear and Particle Science*, 61(1):467–489, 2011.

[111] V. F. Hess. Über Beobachtungen der durchdringenden Strahlung bei sieben Freiballonfahrten. *Physikalische Zeitschrift*, 13:1084–1091, 1912.

[112] K. Bernlöhr, O. Carrol, R. Cornils, et al. The optical system of the H.E.S.S. imaging atmospheric Cherenkov telescopes. Part I: layout and components of the system. *Astroparticle Physics*, 20:111–128, November 2003.

[113] R. Cornils, S. Gillessen, I. Jung, et al. The optical system of the H.E.S.S. imaging atmospheric Cherenkov telescopes. Part II: mirror alignment and point spread function. *Astroparticle Physics*, 20:129–143, November 2003.

[114] Bolmont, J. et al. The camera of the fifth H.E.S.S. telescope. Part I: System description. *Nuclear Instruments and Methods in Physics Research A*, 761:46–57, October 2014.

[115] J. M. Davies and E. S. Cotton. Design of the quartermaster solar furnace. *Solar Energy*, 1:16–22, April 1957.

[116] H.E.S.S. Collaboration. Calibration of cameras of the H.E.S.S. detector. *Astroparticle Physics*, 22:109–125, 2004.

[117] R. Winston. High Collection Nonimaging Optics. In *Proc. SPIE 1038, 6th Mtg in Israel on Optical Engineering*, 1989.

[118] H.E.S.S. Collaboration. Localizing the VHE γ-ray source at the Galactic Centre. *MNRAS*, 402(3):1877–1882, 2010.

[119] H.E.S.S. Collaboration. Gamma-ray blazar spectra with H.E.S.S. II mono analysis: The case of PKS 2155-304 and PG 1553+113. *Astronomy and Astrophysics*, 600:A89, April 2017.

[120] M. Holler. *Photon Reconstruction for the H.E.S.S. 28 m Telescope and Analysis of Crab Nebula and Galactic Centre Observations*. PhD thesis, Universität Potsdam, June 2014.

[121] A. Balzer, M. Füßling, M. Gajdus, D. Göring, A. Lopatin, M. de Naurois, S. Schlenker, U. Schwanke, and C. Stegmann. The H.E.S.S. central data acquisition system. *Astroparticle Physics*, 54:67–80, February 2014.

[122] M. de Naurois. Very High Energy astronomy from H.E.S.S. to CTA. Opening of a new astronomical window on the non-thermal Universe, Université Pierre et Marie Curie - Paris VI. Habilitation Dissertation, 2012.

[123] Chalme-Calvet, R. and de Naurois, M. and Tavernet, J.-P. (H.E.S.S. Collaboration). Muon efficiency of the H.E.S.S. telescope. *ArXiv e-prints*, March 2014.

[124] A. M. Hillas. International cosmic ray conference. In F. C. Jones, editor, *19th International Cosmic Ray Conference, La Jolla (USA)*, volume 3, pages 445–448, 1985.

[125] T. C. Weekes, M. F. Cawley, D. J. Fegan, K. G. Gibbs, A. M. Hillas, P. W. Kowk, R. C. Lamb, D. A. Lewis, D. Macomb, N. A. Porter, P. T. Reynolds, and G. Vacanti. Observation of TeV gamma rays from the Crab nebula using the atmospheric Cerenkov imaging technique. *ApJ*, 342:379–395, July 1989.

[126] S. Le Bohec, B. Degrange, M. Punch, et al. A new analysis method for very high definition imaging atmospheric Cherenkov telescopes as applied to the CAT telescope. *Nuclear Instruments and Methods in Physics Research A*, 416:425–437, October 1998.

[127] R. D. Parsons and J. A. Hinton. A Monte Carlo template based analysis for air-Cherenkov arrays. *Astroparticle Physics*, 56:26–34, April 2014.

[128] R. D. Parsons, T. Murach, and M. Gajdus. H.E.S.S. II Data Analysis with ImPACT. In A. S. Borisov, V. G. Denisova, Z. M. Guseva, E. A. Kanevskaya, M. G. Kogan, A. E. Morozov, V. S. Puchkov, S. E. Pyatovsky, G. P. Shoziyoev, M. D. Smirnova, A. V. Vargasov, V. I. Galkin, S. I. Nazarov, and R. A. Mukhamedshin,

editors, *34th International Cosmic Ray Conference (ICRC2015)*, volume 34 of *International Cosmic Ray Conference*, page 826, July 2015.

[129] D. Heck, J. Knapp, J. N. Capdevielle, G. Schatz, and T. Thouw. *CORSIKA: a Monte Carlo code to simulate extensive air showers. Forschungszentrum Karlsruhe GmbH, Karlsruhe (Germany)., Feb 1998, V + 90 p., TIB Hannover, D-30167 Hannover (Germany).* February 1998.

[130] K. Bernlöhr. Simulation of imaging atmospheric Cherenkov telescopes with CORSIKA and sim_ telarray. *Astroparticle Physics*, 30:149–158, October 2008.

[131] S. Gillessen. *Sub-Bogenminuten-genaue Positionen von TeV Quellen mit H.E.S.S.* PhD thesis, Ruprecht-Karls-Universität Heidelberg, Germany, `https://www.bsz-bw.de/cgi-bin/xvms.cgi?SWB11244050`, 2004.

[132] S. Ohm, C. van Eldik, and K. Egberts. γ/hadron separation in very-high-energy γ-ray astronomy using a multivariate analysis method. *Astroparticle Physics*, 31 (5):383 – 391, 2009. ISSN 0927-6505.

[133] M. P. Kertzman and G. H. Sembroski. Computer simulation methods for investigating the detection characteristics of TeV air Cherenkov telescopes. *Nuclear Instruments and Methods in Physics Research A*, 343:629–643, April 1994.

[134] November 2015. URL `https://hess-confluence.desy.de/confluence/pages/viewpage.action?pageId=10234235#Model++:NSBGoodnessvs.UniformNSBGoodness(SearchforStdCuts)-OtherEffects`.

[135] H.E.S.S. Collaboration. Diffuse Galactic gamma-ray emission with H.E.S.S. *Physical Review D*, 90(12):122007, December 2014.

[136] D. Berge, S. Funk, and J. Hinton. Background modelling in very-high-energy γ-ray astronomy. *Astronomy and Astrophysics*, 466:1219–1229, May 2007.

[137] T.-P. Li and Y.-Q. Ma. Analysis methods for results in gamma-ray astronomy. *ApJ*, 272:317–324, September 1983.

[138] F. Piron, A. Djannati-Atai, M. Punch, et al. Temporal and spectral gamma-ray properties of Mkn 421 above 250 GeV from CAT observations between 1996 and 2000. *Astronomy and Astrophysics*, 374:895–906, August 2001.

[139] MAGIC Collaboration. MAGIC upper limits to the VHE gamma-ray flux of 3C 454.3 in high emission state. *Astronomy and Astrophysics*, 498:83–87, April 2009.

[140] H.E.S.S. Collaboration. Observations of the Crab nebula with HESS. *Astronomy and Astrophysics*, 457:899–915, October 2006.

[141] T. Murach, M. Gajdus, and R. D. Parsons. A Neural Network-Based Monoscopic Reconstruction Algorithm for H.E.S.S.II. In *Proceedings of the 34th International Cosmic Ray Conference (ICRC2015), The Hague, The Netherlands*, 2015.

[142] M. Holler, J. Chevalier, J.-P. Lenain, M. de Naurois, and D. Sanchez. Run-Wise Simulations for Imaging Atmospheric Cherenkov Telescope Arrays. In *Proceedings of the 35rd International Cosmic Ray Conference (ICRC2017), Busan (Korea)*, November 2017.

[143] W.-R. Hamann, G. Gräfener, and A. Liermann. The Galactic WN stars. Spectral analyses with line-blanketed model atmospheres versus stellar evolution models with and without rotation. *Astronomy and Astrophysics*, 457:1015–1031, October 2006.

[144] P. A. Crowther, L. J. Smith, and A. J. Willis. Fundamental parameters of Wolf-Rayet stars. V. The nature of the WN/C star WR 8. *Astronomy and Astrophysics*, 304:269, December 1995.

[145] W. S. G. Walker, M. Blackford, R. Butland, and E. Budding. Absolute parameters of young stars: QZ Carinae. *MNRAS*, 470(2):2007–2017, 2017.

[146] Y. Nazé, P. S. Broos, L. Oskinova, et al. Global X-ray Properties of the O and B Stars in Carina. *ApJS*, 194(1):7, 2011.

[147] N. D. Morrison and P. S. Conti. Spectroscopic studies of O-type binaries. VI - The quadruple system QZ Carinae /HD 93206/. *ApJ*, 239:212–219, July 1980.

[148] P. Mayer, R. Lorenz, H. Drechsel, and A. Abseim. The early-type multiple system QZ Carinae. *Astronomy and Astrophysics*, 366:558–564, February 2001.

[149] E. R. Parkin and J. M. Pittard. A 3D dynamical model of the colliding winds in binary systems. *MNRAS*, 388(3):1047–1061, 2008.

[150] L. K. Townsley, P. S. Broos, M. F. Corcoran, et al. An Introduction to the Chandra Carina Complex Project. *ApJS*, 194(1):1, 2011.

[151] P. S. Broos, L. K. Townsley, E. D. Feigelson, K. V. Getman, G. P. Garmire, T. Preibisch, N. Smith, B. L. Babler, S. Hodgkin, R. Indebetouw, M Irwin, R. R.

King, J. Lewis, S. R. Majewski, M. J. McCaughrean, M. R. Meade, and H. Zinnecker. A Catalog of Chandra X-ray sources in the Carina Nebula. *ApJS*, 194(1): 2, 2011.

[152] E. R. Parkin, P. S. Broos, L. K. Townsley, et al. X-ray Emission from the Double-binary OB-star System QZ Car (HD 93206). *ApJS*, 194:8, May 2011.

[153] Acero, F. et al., Fermi-LAT collaboration. Fermi Large Area Telescope Third Source Catalog. *ApJS*, 218(2):23, 2015.

[154] A. M. Bykov. Particle Acceleration and Nonthermal Phenomena in Superbubbles. *Space Science Reviews*, 99(1-4):317–326, October 2001.

[155] CTA Consortium. Design concepts for the Cherenkov Telescope Array CTA: an advanced facility for ground-based high-energy gamma-ray astronomy. *Experimental Astronomy*, 32:193–316, December 2011.

[156] J. R. North, P. G. Tuthill, W. J. Tango, and J. Davis. γ^2 Velorum: orbital solution and fundamental parameter determination with SUSI. *MNRAS*, 377: 415–424, May 2007.

[157] K. Reitberger, R. Kissmann, A. Reimer, and O. Reimer. 3D Magnetohydrodynamic Models of Nonthermal Photon Emission in the Binary System γ^2 Velorum. *ApJ*, 847:40, September 2017.